LRP 592/97 November 1997

EXTERNAL KINKS IN PLASMAS WITH HELICAL BOUNDARY DEFORMATION AND NET TOROIDAL CURRENT

A. Ardelea

Abstract

The investigation of the global ideal magnetohydrodynamic (MHD) stability of plasmas with helical boundary shape and nonvanishing toroidal plasma current constitutes the principal aim of this work. Global external modes with small values of m, n (typically $n = 1, 2, 3$ and $m = n + 1$) are studied, where m and n are the poloidal and toroidal mode numbers, respectively.

The first and main part of the work concentrates on fixed boundary equilibria generated by systematically varying parameters such as the type and the magnitude of the boundary deformation, the number of equilibrium field periods N_{per}, the aspect ratio, the toroidal current density profile, β and the pressure profile. Due to the periodicity of the equilibrium, couplings between Fourier perturbation components with different toroidal mode numbers n occur and lead to the apparition of families of modes. The study of a particular (m, n) mode has to take into account all (m_l, n_l) perturbation components with n_l belonging to the same family as n. The stability analysis is carried out in the parameter region where the inverse rotational transform (the safety factor in the traditional *tokamak notation*) $q \leq 2.0$ and $\beta \leq 2\%$. A particular property of the configurations investigated is that equilibrium Fourier components $(m_e, N_{per} n_e)$ which are involved in the couplings between the (m, n) mode studied and the (m_k, n_k) perturbation components with $m_k > n_k > n$ (that exhibit resonances in the $q > 1$ region are very small. As a consequence, the contributions of the $(m, n) \times (m_k, n_k)$ couplings to the potential energy are very weak.

It is shown that a helical boundary deformation can stabilize the $n = 1, 2, 3$ external modes; if δ is a measure of the plasma boundary deformation, then windows of stability $[\delta_{min}, \delta_{max}]$ may exist for a large variety of equilibrium parameters. The results are analysed in terms of stability areas in the (q_{axis}, q_{edge}) plane. In order to enable a systematic exploration of the space of parameters, an investigation procedure based on jobs chaining and automatic selection of input data for the equilibrium and stability codes has been conceived and implemented.

In the second part of the work, a system of coils that produce a helical, a toroidal and a vertical magnetic field is proposed to obtain configurations with the desired helical boundary shape. A field line tracing code is adapted to fine tune the current and geometrical parameters of the coils to generate closed, helical magnetic surfaces that approximately reproduce those of the fixed boundary calculations in vacuum. The magnetic field from the external currents is given as input to a free boundary equilibrium code which calculates equilibria with a prescribed toroidal current density and finite β. Finally, the stability analysis is performed and the main conclusion of the fixed boundary calculations, namely the existence of a stability window, is confirmed.

Resumé

Le but principal de ce travail a été l'investigation de la stabilité MHD globale des plasmas avec déformation hélicoïdale du bord et courant toroïdal non nul. Les modes globaux externes (m,n) avec nombre d'onde poloïdal m et toroïdal n réduits, plus précisément $n = 1,2,3$ et $m = n+1$, ont été étudiés.

Dans la première partie du travail, des équilibres avec bord du plasma fixe ont été générés en variant de manière systématique des paramètres comme le type et l'amplitude de la déformation du bord, le nombre de périodes d'équilibre du champ magnétique N_{per}, le rapport d'aspect, le profil de densité de courant toroïdal, le facteur β et le profil de pression. En raison du caractère périodique de l'équilibre, des couplages ont lieu entre des composantes de Fourier de la perturbation ayant des nombres d'onde toroïdaux différents, ce qui entraine l'apparition des familles de modes. L'étude d'un mode particulier (m,n) requiert la présence de toutes les composantes (m_l, n_l) avec n_l appartenant à la même famille que n. L' analyse de la stabilité a été effectuée dans la zone des paramètres pour lesquels l'inverse de la transformée rotationelle (le facteur de sécurité dans le language tokamak traditionnel) $q \leq 2.0$ et $\beta \leq 2\%$. Une des propriétés caractéristiques des configurations étudiées est la suivante: les composantes de Fourier $(m_e, N_{per} n_e)$ de l'équlibre, impliquées dans les couplages entre le mode (m,n) étudié et les composantes (m_k, n_k) de la perturbation avec $m_k > n_k > n$ (résonnantes pour $q > 1$), sont très faibles. Par conséquent, les contributions des couplages $(m,n) \times (m_k, n_k)$ à l'énergie potentielle sont très faibles.

Il a été montré qu'une déformation hélicoïdale du bord du plasma peut stabiliser les kinks externes avec $n = 1,2,3$. Si δ représente une mesure de la déformation du bord, des fenêtres de stabilité $[\delta_{min}\delta_{max}]$ peuvent apparaître pour une large variété de combinaisons de paramètres d'équilibre. Les résultats ont été analysés en termes de zones de stabilité dans le plan $\{q_{axe}, q_{bord}\}$.
Une méthode a été concue et implementée pour automatiser les calculs intensifs provoqués par l'investigation à large échelle de l'espace des paramètres.

Dans la deuxième partie du travail, un ensemble de bobines produisant un champ hélicoïdal, toroïdal et vertical a été proposé pour obtenir des équilibres plasmas avec le type de déformation du bord souhaité. Un code permettant de suivre les lignes magnétiques a été adapté pour trouver les courants et les paramètres géométriques des bobines nécessaires pour générer des surfaces de flux fermées hélicoïdales dans le vide, reproduisant approximativement celles des calculs avec bord fixe. Le champ du vide ainsi obtenu a été utilisé comme input par un code d'équilibre avec lequel on a calculé des équilibres avec bord du plasma libre, courant plasma non nul et β fini.
En dernier lieu, l'analyse de stabilité globale à été effectuée et le principal résultat obtenu suite aux calculs avec les équilibres à bord fixe, à savoir l'existence des fenêtres de stabilité, a été confirmé.

Contents

Chapter 1

Introduction

1.1 The subject

Tokamaks and stellarators are presently the two leading systems in the magnetic confinement fusion program. Tokamaks, among which the largest existing devices like the Joint European Torus (JET) [1], the Tokamak Fusion Test Reactor (TFTR) [2], the Japan Tokamak (JT-60) [3]) are to be found, are basically pulsed machines and the maximum magnetic flux produced by the Ohmic current transformer is a crucial factor limiting the duration of the pulse. Current drive techniques like Neutral Beam Injection (NBI) or radio frequency (rf) waves are employed to bring tokamaks to a steady-state regime but this procedure requires additional input power and increases significantly the total cost of the machine.
With respect to this problem, stellarators have the inherent advantage of operating in a steady-state regime. The absence of net plasma current eliminates the risk associated with disruptions and reduces the complications arising from combining current drive schemes with the conditions for good confinement at high β. Moreover, the currents flowing in external conductors allow a wider control of the parameters of the magnetic configuration compared with the tokamak case. This flexibility has to be paid through complicated and difficult to manufacture systems of helical coils or sets of three-dimensional coils in the modular systems. Assembling has to be very accurate because slight misalignments may alterate the magnetic surfaces and introduce important island structures. In this category we find large devices like the Wendelstein 7-X (W7-X) [4], the TJ-II heliac [5] and the Large Helical device (LHD) [6] characterized by a high aspect ratio $A \geq 7$ as well as compact machines like the Compact Helical System (CHS) [7] and the Compact Auburn Torsatron (CAT) [8]) with $A \approx 5$.

Beside these classical configurations a series of new concepts have emerged during the last years. The ULAR (ultra low aspect ratio) tokamaks like the Small Tight Aspect

Ratio Tokamak (START) [9], the Current Drive Experiment-Upgrade Tokamak (CDX-U) [10]) seem promising for obtaining high density and high β plasmas with relatively low magnetic field. The ultra low aspect ratio spherical stellarator (SS) [11] which differs from ULAR tokamaks by the inclination of the external parts of the toroidal field coils, offers closed magnetic surfaces in vacuum with large enclosed volume, high external rotational transform and strong vacuum magnetic well. An important characteristic of the SS is that the net plasma current is non vanishing; it is shown in [11] that bootstrap effects can supply the current necessary for high β equilibrium. The tokamak-stellarator hybrid with inclined coils - the stellamak - presented in [12] was proposed with the standard toroidal field (TF) and poloidal field (PF) coils of the tokamak and in addition a system of simple inclined planar coils to produce stellarator effects. The device should be able to operate as a pure tokamak, as a pure stellarator or in a hybrid manner with smooth transitions between these regimes depending on the current flowing in the coils. Finally, EPEIUS [13] - a small aspect ratio tokamak-torsatron hybrid with modular coils was recently designed to operate with non zero toroidal plasma current and a total rotational transform with a profile similar to that of tokamaks. The study of the magnetic surface resilience as function of the plasma current and of the disruptions induced by this current in the presence of an externally imposed rotational transform are among the main goals of the proposed EPEIUS experiment.

The present work considers plasmas with a helically deformed boundary and non zero net toroidal current. This type of configuration is closer to the standard devices than to those mentioned above; its main characteristic is however that the plasma current is immersed in a stellarator-like field. We decided to study the current-driven external kink modes which appear in such a configuration. According to the global MHD theory, these modes can set severe limits on the current flowing in confinement devices. The stability of helical modes has been widely investigated but most of the numerical or analytical results have been obtained for straight plasma columns (with or without an additional external rotational transform) or for tokamak configurations (the currentless stellarators were not the object of systematic studies with respect to this problem)

It is known - see [14], [15] - that the most dangerous helical modes are those with small m and n. This statement expresses a rather general tendency of stability to improve with increasing m; it does not necessarily mean that for any $\bar{m}$, the mode with $m = \bar{m} + 1$ is more stable than the mode with $m = \bar{m}$. In tokamaks, some of the most important current limitations come from the $n = 1$ internal kink, the Kruskal-Shafranov condition, and the $m \geq 2$ low β external kinks. If q represents the safety factor then the $n = 1, n = 1$ internal kink requires $q_{axis} > 1$ for stability; this mode (including the resistive case) and

its nonlinear evolution is believed to be responsible for the sawtooth oscillations observed in tokamak experiments. The Kruskal-Shafranov limit leads to the condition $q_{edge} > 1$ and stability against higher m external kinks requires a current profile which decays to zero sufficiently rapidly near the plasma edge, typically implying $q_{edge}/q_{axis} \simeq$ 2-3 The effect of the current profile on the stability of kink modes in cylindrical tokamaks is analyzed in [16] on the basis of the Succesive Current Layer (SCL) principle (developed in the same reference). The current profile is considered to be the sum of nested cylindrical current layers disposed around the initial axis and the effect of adding an individual layer on the stability properties is studied. The authors present some optimized current profiles c.f. [16], and conclude that $q_{edge} > 2$ is a theoretical limit ensuring the stability against all kink (and tearing) modes.

The effect of an external rotational transform ι_h on the plasma stability with respect to helical modes was first analyzed in the simplest case of a pressureless straight plasma column with uniform current density [17]. It is shown that for $\iota_h = const$ analytical conditions for stability can be obtained; stability windows at fixed n appear when varying $\iota(a)$ (the value of the total rotational transform ι at the plasma boundary $r = a$) in the interval.

$$\frac{n - \iota_h}{m - 1} < \iota(a) < \frac{n}{m - 1} \tag{1.1}$$

If modes with different n are taken into account the gaps of stability dissapear. The more general case of an non uniform current density and non constant external rotational transform, was considered by M.I.Mikhailov and V.D.Shafranov in [18]. Using the SCL Principle, the authors analysed the role of the individual regions of the current channel for ensuring stability. They showed that the central and peripherial current layers play opposite roles in tokamak-like configurations $\iota' < 0$ and stellarator-like configurations $\iota' > 0$ but concluded that that the growth of the absolute value of the difference $|\Delta\iota| = |\iota(a) - \iota(0)|$ improves the stability in both cases. In a later publication [19], the same authors extended their analysis to the cases where a conducting shell is present. A relation was derived which expresses a stability condition for a current channel of radius r with respect to the m/n mode with resonance surface between the plasma boundary and the conducting shell:

$$(m - 1)\iota - n + \iota_h + r\iota_h'/2 + L[(m + 1)\iota - n - \iota_h - r\iota_h'/2] > 0 \tag{1.2}$$

with $L = (r/b)^{2m}$ and b is the shell radius. From Eq.(1.2) it results that for tokamak-like profiles $\iota' < 0$, $\iota_h = 0$ with $\iota_J(0) < 1$ the ideal modes with $m = n + 1$ and resonant surface in the vacuum are always unstable. Here ι_J is the current rotational transform. When

an external rotational transform is added these modes are unstable if $\iota_J(0) < 1 - \iota_h/n$; in principle stabilization can occur even at $\iota_J(0) < 1$. Using Eq.(1.2) and assuming $\iota_h(r) = const$, diagrams of stability with respect to the $(m = n + 1, n)$ modes were calculated in the $(\iota_J(a), \iota_h)$ plane; stability zones appeared for ι_h larger than 0.4-0.6. The authors conclude that the shearless stellarator rotational transform can stabilize all ideal modes; for that purpose the stellarator rotational transform should be of the order of the current rotational transform $\iota_h \sim \iota_J$. It is also stated that rather small stellarator transforms of the order 0.1-0.15 are useful for stabilizing the most dangerous 2/1 mode (from the viewpoint of disruptive instability) at different current profiles and $\iota(0) = 1$.

1.2 The objectives

With respect to the results of these previous investigations we formulate the objectives of the present work as follows:

• The global MHD stability of toroidal configurations having a helical plasma boundary, arbitrary toroidal current density profiles and finite β will be investigated with respect to (m, n) external kink modes with small toroidal mode numbers n =1, 2, 3, and poloidal mode numbers equal to $m = n + 1$.

• The role of the (helical) boundary shape will be studied in particular. For this purpose the numerical equilibria will be calculated with a fixed boundary code like VMEC (cf. Chap.2). The set of equilibrium parameters used in our investigation consists of the type and amount of boundary deformation, the plasma current density profile, the number of field periods, the aspect ratio, the pressure profile and β. The expression "boundary deformation" will be frequently used and means the deviation from the circular tokamak cross section.

The external rotational transform results from the prescription of the boundary shape and the total ι is determined then from equilibrium computations; it is no longer calculated as the sum of two separate contributions $\iota = \iota_J + \iota_h$ with a second term ι_h artificially added to the system. This is an important difference when comparing with [17], [18] and [19].

• As the work consists mainly in a numerical study with a large number of parameters considered, a method of investigation will be developed. Its aim is to define how the space of parameters should be explored in a systematic way and to create appropriate tools for running the equilibrium (VMEC) and stability (TERPSICHORE - c.f. Chap.2) codes in an efficient and handy way (from the view-point of the user). The method is designed to serve our purposes but should be flexible enough to be applied for systematic 3D equilibrium and/or MHD stability investigations of any type of configuration.

• Mercier and to a certain extent ballooning stability will also be considered but not as principal objects of the study.

This thesis is organized as follows: In Chap.2 the numerical tools used in the investigation are presented together with the underlying theoretical aspects of 3D equilibrium and stability. Chap.3 describes in detail the configurations which are studied and explains the choices which were made when selecting the equilibrium and stability parameters. The investigation method is presented in Chap.4; the peculiarities of the configurations studied which determine the details of the investigation procedure are discussed. Finally, the results are presented in Chap.5. Chap.6 represents an extension of the study. Its aim is to discuss the possibility of practically realizing a configuration of coils which produce the desired type of helical boundary deformation. The summary and conclusions are given in Chap.7

Chapter 2

Equilibrium and Stability

2.1 Equilibrium and the VMEC code

The 3D fixed boundary equilibria with nested magnetic surfaces and single magnetic axis are generated with the VMEC code [20] [21]. The basic equations describing static MHD equilibrium in magnetically confined plasmas are given by the Gauss law, Ampere's law and the MHD equilibrium force balance equation

$$\begin{aligned} \vec{\nabla} \cdot \vec{B} &= 0 \\ \vec{J} &= \mu_0 \vec{\nabla} \wedge \vec{B} \\ \vec{F}_{MHD} \equiv \vec{J} \wedge \vec{B} - \vec{\nabla} p &= 0 \end{aligned} \tag{2.1}$$

where $\vec{B}$ is the magnetic field, $\vec{J}$ represents the plasma current, μ_0 is the permeability of free space and p is the isotropic plasma pressure. The quantity F_{MHD} is the residual MHD force which must vanish in the equilibrium. In a geometry with nested flux surfaces, a coordinate system (s, u, v) is introduced with, $0 < s < 1$ the radial coordinate which labels the magnetic flux surfaces, and u and v the periodic poloidal and toroidal angular variables. A general representation of the magnetic field which satisfies $\vec{B} \cdot \vec{\nabla} s = 0$ and $\vec{\nabla} \cdot \vec{B} = 0$ is given by

$$\vec{B} = \vec{\nabla} v \wedge \vec{\nabla} \Psi + \vec{\nabla} \Phi \wedge \vec{\nabla} u^* \tag{2.2}$$

Here $2\pi\Psi(s)$ is the poloidal magnetic flux and $2\pi\Phi(s)$ is the toroidal magnetic flux (Φ is in fact proportional to s). The u^* variable represents a generalized poloidal angle such that in (s, u^*, v) the magnetic field lines are straight. It is related to u through the expression [22]

$$u^* = u + \lambda(s,u,v) \tag{2.3}$$

where λ is a periodic stream function with zero average over a magnetic surface. The contravariant basis vectors are $\vec{e^i} = \vec{\nabla}\alpha_i$ with $\alpha = (s,u,v)$, the covariant basis vectors are $\vec{e_i} = \partial\vec{x}/\partial\alpha_i = \sqrt{g}\vec{\nabla}e^j \wedge \vec{\nabla}e^k$ and $\sqrt{g} = (\vec{\nabla}s \cdot \vec{\nabla}u \wedge \vec{\nabla}v)^{-1}$ is the Jacobian. The contravariant components of the magnetic field become then

$$\begin{aligned} B^s &= 0 \\ B^u &= \frac{\Phi'(s)}{\sqrt{g}}\left(\iota(s) - \frac{\partial\lambda}{\partial v}\right) \\ B^v &= \frac{\Phi'(s)}{\sqrt{g}}\left(1 + \frac{\partial\lambda}{\partial u}\right) \end{aligned} \tag{2.4}$$

In the covariant representation $\vec{B}$ is written as

$$\vec{B} = X_s\vec{\nabla}s + J(s)\vec{\nabla}u - I(s)\vec{\nabla}v + \vec{\nabla}Q(s,u,v) \tag{2.5}$$

where the covariant components are

$$\begin{aligned} B_s &= X_s + \frac{\partial Q}{\partial s} \\ B_u &= J(s) + \frac{\partial Q}{\partial u} \\ B_v &= -I(s) + \frac{\partial Q}{\partial v} \end{aligned} \tag{2.6}$$

with $J(s)$ the toroidal current flux function and I(s) the poloidal current flux function. The periodic function $Q(s,u,v)$ is generally derived from λ, Φ, Ψ, J and I using the transformations between the co- and contravariant components of $\vec{B}$. The $\vec{B}\cdot\vec{\nabla}$ operator aquires the following form

$$\vec{B}\cdot\vec{\nabla} = \left(\Psi'(s) - \frac{\partial\lambda}{\partial v}\right)\frac{\partial}{\partial u} + \left(\Phi'(s) + \frac{\partial\lambda}{\partial u}\right)\frac{\partial}{\partial v} \tag{2.7}$$

In the inverse representation of the MHD equilibrium, the (s,u,v) coordinates are considered to be independent and the cylindrical coordinates (R,ζ,Z) form the dependent coordinates which are expanded in Fourier series

$$
\begin{aligned}
R(s,u,v) &= \sum_{m_e,n_e} R_{m_e n_e}(s) cos(m_e u - n_e v) \\
Z(s,u,v) &= \sum_{m_e,n_e} Z_{m_e n_e}(s) sin(m_e u - n_e v) \\
\zeta &= v
\end{aligned}
\tag{2.8}
$$

The λ function which was retained to allow flexibility in specifing the poloidal angle is expanded as

$$
\lambda(s,u,v) = \sum_{m_e,n_e} \lambda_{m_e n_e}(s) sin(m_e u - n_e v) \tag{2.9}
$$

Its role is to renormalize the poloidal angle in an iterative procedure such as to minimize the spectral width of the Fourier series with respect to the poloidal mode number m_e.

The VMEC code computes the Fourier amplitudes $R_{m_e,n_e}(s)$, $Z_{m_e,n_e}(s)$ and $\lambda_{m_e,n_e}(s)$ using an energy minimization technique based on the functional

$$
W = \int_{\Omega_P} d^3x [B^2/(2\mu_0) + p/(\Gamma - 1)] \tag{2.10}
$$

with Γ being the adiabatic index and Ω_P representing the toroidal domain. The variations of W are performed with respect to virtual displacements of $\vec{B}$ and p which leave invariant the magnetic flux functions Ψ and Φ and the mass function $M(s)$. The cylindrical coordinates (R, ζ, Z) and λ are supposed to depend on the flux coordinates and also on an artificial time parameter t

$$
\begin{aligned}
\frac{dW}{dt} &= -\int d^3\alpha \, F_R \frac{\partial R}{\partial t} - \int d^3\alpha \, F_Z \frac{\partial Z}{\partial t} - \int d^3\alpha \, F_\lambda \frac{\partial \lambda}{\partial t} \\
&\quad - \int\int_{s=1} du dv \left[R \left(p + \frac{B^2}{2\mu_0} \right) \left(\frac{\partial R}{\partial u} \frac{\partial Z}{\partial t} - \frac{\partial Z}{\partial u} \frac{\partial R}{\partial t} \right) \right]
\end{aligned}
\tag{2.11}
$$

with F_R, F_Z and F_λ given in [22] and $\alpha \in (s,u,v)$ [23]. The last term represents the energy change due to the moving plasma-vacuum interface. In a fixed boundary calculation as in VMEC, it dissapears because by definition $\partial R/\partial t = \partial Z/\partial t = 0$ at $s = 1$. The surface contribution appears only in free boundary calculations where it has to be computed consistently with the fields produced by the currents flowing in the external coils. It is shown in [21], [23] that the coefficients F_R, F_Z and F_λ correspond to the different

components of the force balance equation (2.1). Thus, for a fixed boundary plasma, W is stationary when the MHD equilibrium equations $F_{MHD} \cong 0$ are satisfied. The minimisation of W is performed via a steepest descent procedure coupled with the application of a preconditioning algorithm [21].

2.2 MHD Stability and the TERPSICHORE code

2.2.1 The Boozer coordinate system

Originally, the introduction of the Boozer coordinate system [24] was derived from neoclassical transport considerations. A. Boozer formulated the equations for particle drift orbits in a new magnetic coordinate system which separated the fast particle motion along the magnetic field lines from the slow drift across the lines.
Nuhrenberg and Zille showed later [25] that these coordinates were also suited to the formulation of the ideal MHD stability problem. The advantage of using them in numerical computations will be mentioned in the following section. In the Boozer coordinate system (s, θ, ϕ), $0 \leq s \leq 1$ represents the radial variable, $0 \leq \theta \leq 2\pi$ is the periodic poloidal coordinate and $0 \leq \phi \leq 2\pi/N_{per}$ is the periodic toroidal coordinate with N_{per} being the number of equilibrium field periods. The contravariant expression of the magnetic field is written as

$$\vec{B} = \vec{\nabla}\phi \wedge \vec{\nabla}\Psi + \vec{\nabla}\Phi \wedge \vec{\nabla}\theta \tag{2.12}$$

with $\Psi(s)$ being the poloidal magnetic flux function and $\Phi(s)$ being the toroidal magnetic flux function. This form satisfies the condition $\vec{B} \cdot \vec{\nabla}s = 0$ supposing configurations with single magnetic axes, nested flux surfaces and no islands or X-points. The contravariant components $B^i = \vec{B} \cdot \vec{\nabla}\alpha_i$, $i \in (s, \theta, \phi)$ can be easily derived

$$B^\phi = 0 \qquad B^\theta = \frac{\Psi'(s)}{\sqrt{g}} \qquad B^\phi = \frac{\Phi'(s)}{\sqrt{g}}$$

In covariant form the magnetic field is written in the form

$$\vec{B} = B_s\vec{\nabla}s + J(s)\vec{\nabla}\theta - I(s)\vec{\nabla}\phi \tag{2.13}$$

where $J(s)$ represents the toroidal current flux function and I(s) represents the poloidal current flux function.

The VMEC coordinate system was designed to minimize the spectrum of Fourier modes necessary to obtain the equilibrium to a specified accuracy. A stability code may have other criteria for choosing an optimal coordinate system; the numerical computation of MHD stability in 3D systems requires for example a reliable representation of the $\vec{B} \cdot \vec{\nabla}$ operator and of the parallel current (the latter is an important source of instabilities). In the Boozer coordinate system the magnetic field lines are straight and the $\vec{B} \cdot \vec{\nabla}$ operator is written as

$$\vec{B} \cdot \vec{\nabla} = \Psi'(s)\frac{\partial}{\partial \theta} + \Phi'(s)\frac{\partial}{\partial \phi} \tag{2.14}$$

After some algebra the radial component of the force balance equation takes the form

$$\sqrt{g}p'(s) + \Psi'(s)J'(s) - \Phi'(s)I'(s) = \sqrt{g}\vec{B} \cdot \vec{\nabla}(B_s) \tag{2.15}$$

This relation is used to find the radial covariant component of the magnetic field. The $\vec{\nabla} \cdot \vec{j} = 0$ condition leads to

$$\sqrt{g}\vec{B} \cdot \vec{\nabla}\left(\frac{\vec{j} \cdot \vec{B}}{B^2}\right) = \frac{p'(s)}{(\sqrt{g}B^2)}\left[I(s)\frac{\partial \sqrt{g}}{\partial \theta} + J(s)\frac{\partial \sqrt{g}}{\partial \phi}\right] \tag{2.16}$$

which serves for the determination of the parallel current. Thus, both B_s and $\vec{j} \cdot \vec{B}/B^2$ are evaluated by solving magnetic differential equations which are simple in form and based on a simple representation of the $\vec{B} \cdot \vec{\nabla}$ operator. This represents an important reason for formulating the ideal MHD stabiliy problem in the Boozer coordinate system.

2.2.2 Reconstruction of the MHD equilibrium in Boozer coorinates

The geometry resulting from the code VMEC has to be mapped into the Boozer coordinate system used in TERPSICHORE. The angular variables in the Boozer system (θ, ϕ) are related to the angular variables of the equilibrium (u, v) by

$$\begin{aligned} \theta &= u + \alpha(s, u, v) \\ \phi &= v + \gamma(s, u, v) \end{aligned} \tag{2.17}$$

Expressing $\vec{\nabla}\theta$ and $\vec{\nabla}\phi$ in the equilibrium coordinates and equating the corresponding contra- and covariant expressions of $\vec{B}$ in the VMEC coordinates (Eq.(2.2)) and in the

Boozer coordinates (Eq.(2.12)), one obtains a set of equations for the derivatives $\partial\alpha/\partial u$, $\partial\gamma/\partial u$, $\partial\alpha/\partial v$ and $\partial\gamma/\partial v$. Integrating these equations gives

$$\alpha = \frac{\Psi'(s)Q(s,u,v) - I(s)\lambda(s,u,v)}{\Psi'(s)J(s) - \Phi'(s)I(s)} \tag{2.18}$$

$$\gamma = \frac{\Phi'(s)Q(s,u,v) - J(s)\lambda(s,u,v)}{\Psi'(s)J(s) - \Phi'(s)I(s)} \tag{2.19}$$

with Q and λ being the functions appearing in the covariant (Eq.(2.5)) and contravariant (Eq.(2.2) and Eq.(2.3)) expressions of $\vec{B}$ in the VMEC coordinates. The computation of α and γ proceeds as follows: first, the function λ is computed from $\vec{j}\cdot\vec{\nabla}s = 0$ by solving a linear elliptic equation in each flux tube

$$\begin{aligned} &\frac{g_{vv}}{\sqrt{g}}\frac{\partial^2\lambda}{\partial u^2} - \left(\frac{g_{uu}}{\sqrt{g}} + \frac{g_{vv}}{\sqrt{g}}\right)\frac{\partial^2\lambda}{\partial u\,\partial v} + \frac{g_{uu}}{\sqrt{g}}\frac{\partial^2\lambda}{\partial v^2} \\ &+\left[\frac{\partial}{\partial u}\left(\frac{g_{vv}}{\sqrt{g}}\right) - \frac{\partial}{\partial v}\left(\frac{g_{uv}}{\sqrt{g}}\right)\right]\frac{\partial\lambda}{\partial u} + \left[-\frac{\partial}{\partial u}\left(\frac{g_{uv}}{\sqrt{g}}\right) - \frac{\partial}{\partial v}\left(\frac{g_{uu}}{\sqrt{g}}\right)\right]\frac{\partial\lambda}{\partial v} \\ &+\Psi'(s)\frac{\partial}{\partial u}\left(\frac{g_{uv}}{\sqrt{g}}\right) + \Phi'(s)\frac{\partial}{\partial u}\left(\frac{g_{vv}}{\sqrt{g}}\right) - \Psi'(s)\frac{\partial}{\partial v}\left(\frac{g_{uu}}{\sqrt{g}}\right) - \Phi'(s)\frac{\partial}{\partial v}\left(\frac{g_{uv}}{\sqrt{g}}\right) = 0 \end{aligned} \tag{2.20}$$

The necessary equilibrium information is provided by the geometry i.e the inverse variables R, Z and ζ on each flux surface and by the toroidal and poloidal magnetic flux functions $\Phi(s)$ and $\Psi(s)$. Then, the current flux functions $J(s)$ and $I(s)$ are calculated by integrating

$$J(s) = \int_S ds du \sqrt{g}(\vec{j}\cdot\vec{\nabla}v) \tag{2.21}$$

$$I(s) = \int_S ds dv \sqrt{g}(\vec{j}\cdot\vec{\nabla}u) \tag{2.22}$$

with the integrands depending on the equilibrium data and λ. Combining equation (Eq.(2.5)) with the metric relations between the co- and contravariant components of $\vec{B}$ gives

$$\frac{\partial Q}{\partial u} = \frac{g_{uu}}{\sqrt{g}}\left(\Psi'(s) - \frac{\partial\lambda}{\partial v}\right) + \frac{g_{uv}}{\sqrt{g}}\left(\Phi'(s) + \frac{\partial\lambda}{\partial u}\right) - J(s) \tag{2.23}$$

$$\frac{\partial Q}{\partial v} = \frac{g_{vu}}{\sqrt{g}}\left(\Psi'(s) - \frac{\partial\lambda}{\partial v}\right) + \frac{g_{vv}}{\sqrt{g}}\left(\Phi'(s) + \frac{\partial\lambda}{\partial u}\right) + I(s) \tag{2.24}$$

and Q is obtained by integration. Here $g_{ij} = \frac{\partial x^k}{\partial \xi^i}\frac{\partial x^k}{\partial \xi^j}$, $x^k \in \{R, \zeta, Z\}$, $\xi^{i,j} \in \{s, u, v\}$ are the covariant components of the metric tensor g. At this stage all the information necessary to evaluate Eq.(2.17) is available.

2.2.3 Energy Principle and MHD stability

The testing of ideal MHD stability in arbitrary 3D geometry can be done through an elegant and powerful procedure known as the Energy Principle. The derivation of this principle starts with the general linearized equations of motion. A static ideal MHD equilibrium is assumed with

$$\begin{aligned} \vec{j_0} \wedge \vec{B_0} &= \vec{\nabla} p_0 \\ \vec{j_0} &= \vec{\nabla} \wedge \vec{B_0} \\ \vec{\nabla} \cdot \vec{B_0} &= 0 \\ \vec{v_0} &= 0 \end{aligned}$$

and all quantities are linearized about this background state $A(\vec{r}, t) = A_0(\vec{r}) + \tilde{A}_1(\vec{r}, t)$ with $\tilde{A}_1/A_0 << 1$. The initial condition are $\tilde{A}_1(\vec{r}, 0) = 0$ with the exception of $\vec{v_1}(\vec{r}, 0) = \partial\vec{\xi}(\vec{r}, 0)/\partial t$ where $\vec{\xi}$ represents the displacement of the plasma away from its equilibrium position. All perturbed quantities are expressed in terms of $\vec{\xi}$ and assuming a time dependence of the form $\tilde{A}_1(\vec{r}, t) = A_1(\vec{r})exp(-i\omega t)$; the substitution into the MHD equations gives

$$-\omega^2 \rho \vec{\xi} = \mathbf{F}(\vec{\xi})$$

$$\mathbf{F}(\vec{\xi}) = (\vec{\nabla} \wedge \vec{\mathbf{Q}}) \wedge \vec{\mathbf{B}} + (\vec{\nabla} \wedge \vec{\mathbf{B}}) \wedge \vec{\mathbf{Q}} + \vec{\nabla}(\gamma \mathbf{p} \vec{\nabla} \cdot \vec{\xi} + \vec{\xi} \cdot \vec{\nabla} \mathbf{p}) \tag{2.25}$$

where ρ stands for the mass density and $\vec{Q} = \vec{\nabla} \wedge (\vec{\xi} \wedge \vec{B})$ is the perturbed magneticfield. Equation (2.25) can be solved as an eigenvalue problem with the eigenvalue ω^2. The force opeartor $\mathbf{F}$ is self-adjoint [26] which implies that ω^2 is real and stability transitions occur only when ω^2 crosses zero rather than some other point with $Im(\omega) = 0$ and $Re(\omega) \neq 0$. Because of the self-adjointness of $\mathbf{F}$, the stability problem can be recast in the form of a variational principle [27]. The dot product of (2.25) with $\vec{\xi}^*$ is formed and integration over the plasma volume yields

$$\omega^2 = \frac{\delta W(\vec{\xi}^*, \vec{\xi})}{K(\vec{\xi}^*, \vec{\xi})} \tag{2.26}$$

with

$$\delta W(\vec{\xi}^*,\vec{\xi}) = -\frac{1}{2}\int d\vec{r}\,\vec{\xi}^* \cdot \mathbf{F}(\vec{\xi}) \qquad \mathbf{K}(\vec{\xi}^*,\vec{\xi}) = \frac{\mathbf{1}}{\mathbf{2}}\int \mathbf{d^3\vec{r}}\,\rho|\xi|^2$$

The variational principle states that any allowable function $\bar{\xi}$ i.e. bounded in energy and satisfying appropiate boundary conditions i.e. regularity at origin $\bar{\xi}(0) = 0$ and conducting wall on the plasma boundary $\bar{\xi}(1) = 0$, such that ω^2 becomes an extremum is an eigenfunction of the linearized ideal MHD eigenmode equation (2.25). The quantity δW represents the change in potential energy associated with the perturbation and the quantity K is related to the kinetic energy. A minimum of the potential energy is attained at the extremum corresponding to the smallest eigenvalue ω^2. The Energy Principle states that an equilibrium is stable if and only if $\delta W(\vec{\xi}^*,\vec{\xi}) \geq 0$ for all allowable displacements $\vec{\xi}$. If the minimum δW is negative, the Energy Principle guarantees that the actual eigenvalue ω^2 must be smaller than the eigenvalue $\omega^2 = \delta W/K < 0$ calculated with the trial function. The existence of an allowable trial function such that $\delta W < 0$ is sufficient for instability [27], [28].

Such as formulated above, the energy principle is applicable to systems in which the plasma is surrounded directly by a conducting wall. If a vacuum region is present, then the integration domain must be extended to the whole plasma and vacuum volume and the complicated jump conditions arising at the plasma-vacuum interface must be taken into account when generating the trial functions. The reformulation of δW known as the Extended Energy Principle makes the vacuum contribution appear explicitly and includes the pressure balance across the interface condition as a natural boundary condition. This leads to the following expressions for the potential energy [29]

$$\delta W = \delta W_p + \delta W_s + \delta W_v \tag{2.27}$$

$$\delta W_p = \frac{1}{2}\int_{plasma} d^3\vec{r}\,\left[|\vec{Q}|^2 - \vec{\xi}\wedge(\vec{j}\wedge\vec{Q}) + \gamma p|\vec{\nabla}\cdot\vec{\xi}|^2 + (\vec{\xi}\cdot\vec{\nabla}p)(\vec{\nabla}\cdot\vec{\xi})\right] \tag{2.28}$$

$$\delta W_S = \frac{1}{2}\int_{interface} dS\,|\vec{n}\cdot\vec{\xi}|^2\vec{n}\cdot\left[\left[\vec{\nabla}\left(p+\frac{B^2}{2}\right)\right]\right] \tag{2.29}$$

$$\delta W_v = \frac{1}{2}\int_{vacuum} d^3\vec{r}\,|\vec{B}_1|^2 \tag{2.30}$$

where δW_p, δW_S and δW_V represent the plasma, surface and vacuum contributions. The surface term vanishes unless currents flow on the plasma-vacuum interface. Here $[\![A]\!]$

means the jump in A from plasma to vacuum. $\vec{B}_1$ denotes the perturbed magnetic field in vacuum which satisfies [29]

$$\begin{aligned} \vec{n} \cdot \vec{B}_1 \mid_{wall} &= 0 \\ \vec{n} \cdot \vec{B}_1 \mid_{interface} &= \vec{n} \cdot \vec{\nabla} \wedge (\vec{\xi_\perp} \wedge \vec{B}) \mid_{interface} \end{aligned} \tag{2.31}$$

The Extended Energy Principle states that a system is exponentially stable if δW given by (2.27) is positive. An alternate form for δW_p can be derived from (2.28) by separating the perpendicular and parallel components of $\vec{Q}$ and $\vec{j}$. The result is written as [30]

$$\begin{aligned} \delta W_p = \frac{1}{2} \int_{plasma} d^3\vec{r} \Big[&|\vec{Q_\perp}|^2 + B^2 |\vec{\nabla} \cdot \vec{\xi_\perp} + 2\vec{\xi_\perp} \cdot \vec{\kappa}|^2 + \gamma p |\vec{\nabla} \cdot \vec{\xi}|^2 \\ &-2(\vec{\xi_\perp} \cdot \vec{\nabla} p)(\vec{\kappa} \cdot \vec{\xi_\perp^*}) - j_{\parallel} (\vec{\xi_\perp^*} \wedge \vec{b}) \cdot \vec{Q_\perp} \Big] \end{aligned} \tag{2.32}$$

with $\vec{b} = \vec{B}/|\vec{B}|$ and $\vec{\kappa} = \vec{B} \cdot \vec{\nabla} \vec{b}$ being the field line curvature. The first term represents the line bending energy, the second and the third are the energies required to compress the magnetic field and the plasma. These first three terms are positive and hence stabilizing. The last two represent the interchange and kink energies and can be sources of instabilities. The term with $\vec{\nabla} p$ is at the origin of the pressure-driven modes and the term containing $j_{\parallel}$ generates the current-driven modes (kink modes)

The parallel component of the displacement $\xi_{\parallel}$ appears in δW_p only in the fluid compressibility term which is stabilizing. It is possible to minimize the potential energy once for all with respect to $\xi_{\parallel}$ by allowing only displacements satisfying $\vec{\nabla} \cdot \vec{\xi} = 0$. The most pessimistic stability criteria will be obtained for the incompressible limit.

$$\delta W \mid_{\vec{\nabla} \cdot \vec{\xi} = 0} \leq \delta W$$

2.2.4 Variational formulation in TERPSICHORE

The variational formulation of the linear MHD stability of 3D plasmas on which TERPSICHORE is based is described in [31]. The variational equation is written as

$$\delta W_p + \delta W_v - \omega^2 \delta W_k = 0 \tag{2.33}$$

where δW_p, δW_v, δW_k and ω^2 represent the potential energy in the plasma, the magnetic energy in the vacuum region, the kinetic energy and the eigenvalue of the system. The system is unstable to MHD modes when $\omega^2 < 0$

The form of the plasma potential energy adopted in TERPSICHORE is that developed by Nelson and Hedrick [32]

$$\delta W_p = \frac{1}{2}\int d^3x \left[C^2 + \gamma p |\vec{\nabla}\cdot\vec{\xi}|^2 - D\,|\vec{\xi}\cdot\vec{\nabla}s|^2 \right] \tag{2.34}$$

$$\begin{aligned} C &= \vec{\nabla}\wedge(\vec{\xi}\wedge\vec{B}) + \frac{\vec{j}\wedge\vec{\nabla}s}{|\vec{\nabla}s|^2}(\vec{\xi}\cdot\vec{\nabla}s) \\ D &= 2\frac{(\vec{j}\wedge\vec{\nabla}s)\cdot(\vec{B}\cdot\vec{\nabla})\vec{\nabla}s}{|\vec{\nabla}s|^4} \end{aligned} \tag{2.35}$$

with C and D described in detail in [31] and [25]. In the plasma region the displacement vector is expressed in the form

$$\vec{\xi} = \sqrt{g}\xi^s\vec{\nabla}\theta\wedge\vec{\nabla}\phi + \eta\frac{\vec{B}\wedge\vec{\nabla}s}{B^2} + \left[\frac{J(s)}{\Phi'(s)B^2}\eta - \mu\right]\vec{B} \tag{2.36}$$

with (ξ^s, η, μ) the (radial,binormal,parallel) components respectively. By imposing the incompressibility constraint $\vec{\nabla}\cdot\vec{\xi} = 0$ to get rid of the positive definite term $\gamma p(\vec{\nabla}\cdot\vec{\xi})^2$ from δW_p, the parallel component μ is eliminated as a variable from the problem and the two remaining components of the perturbation are expanded in truncated Fourier series,

$$\xi^s(s,\theta,\phi) = \sum_l \xi_l(s)sin(m_l\theta - n_l\phi) \qquad \eta(s,\theta,\phi) = \sum_l \eta_l(s)cos(m_l\theta - n_l\phi) \tag{2.37}$$

where m_l and n_l are the poloidal and toroidal mode numbers, l being the index of an (m,n) pair. The calculation of the correct growth rates is abandoned with this procedure; nevertheless the position of the marginal stability points is not affected by the elimination of the compression term.

The contribution of the vacuum to the potential energy

$$\delta W_v = \frac{1}{2}\int d^3x \left|\vec{\nabla}\wedge\vec{A}\right|^2$$

is treated according to the pseudoplasma technique [31] [33] which considers the vacuum region as a pressureless, shearless and massless pseudoplasma. A new coordinate system

(s_v, θ_v, ϕ_v) is introduced in the vacuum domain such that the geometry varies smoothly across the plasma vacuum interface and the pseudosurfaces are nested. These coordinates do not correspond to the Boozer coordinates in vacuum. The radial coordinate s_v varies between 1 and s_{wall} (wall position) according to the law $s_v(i) = [(s_{wall} - 1)i/N_{vac} + 1]^k$ where N_{vac} is the number of radial mesh points in the vacuum region and k is an integer exponent (generally 2 or 3).
A pseudo-magnetic field $\vec{T}$ ($\vec{A} = \vec{\xi_v} \wedge \vec{T}$) satisfying $\vec{\nabla} \cdot \vec{T} = 0$ and $\vec{T} \cdot \vec{\nabla} s_v = 0$ is prescribed in the vacuum region with

$$\vec{T} = \left(\frac{d\Psi_v}{ds_v} - \frac{\partial \lambda_v}{\partial \phi_v} \right) \vec{\nabla}\phi_v \wedge \vec{\nabla} s_v + \frac{d\Phi_v}{ds_v} \left(1 + \frac{\partial \lambda_v}{\partial \theta_v} \right) \vec{\nabla} s_v \wedge \vec{\nabla}\theta_v \tag{2.38}$$

in analogy with (2.4). The displacement vector ξ_v in vacuum is written in a similar way with the expression of $\vec{\xi}$ in the internal plasma domain (2.36) as

$$\vec{\xi_v} = \sqrt{g_v} \frac{\Phi'(1) X_v}{(d\Phi_v)/(ds_v)} \vec{\nabla}\theta_v \wedge \vec{\nabla}\phi_v + \frac{\vec{T} \wedge \vec{\nabla} s_v}{T^2} Y_v \tag{2.39}$$

In the formulas above Ψ_v and Φ_v are the poloidal and toroidal magnetic fluxes, respectively, in the vacuum region and X_v and Y_v play the role of the normal and binormal components of ξ_v. The boundary condition at the conducting wall is $X_v(s_{wall}, \theta_v, \phi_v) = 0$. At the plasma vacuum-interface the following conditions are imposed

$$\begin{aligned} \iota_v(1) = \frac{d\Psi_v}{d\Phi_v} &= \frac{\Psi'(1)}{\Phi'(1)} = \iota(1) \\ \lambda_v(1, \theta_v, \phi_v) &= 0 \\ X_v(1, \theta_v, \phi_v) &= \xi^s(1, \theta, \phi) \end{aligned} \tag{2.40}$$

Here ι_v is the rotational transform in the vacuum and ι is the rotational transform in the plasma. In TERPSICHORE one imposes $\iota_v(s_v) = \Psi'(1)/\Phi'(1)$ everywhere in order to obtain a shearless vacuum and the function $\lambda_v(s_v, \theta_v, \phi_v)$ is set to zero in the whole vacuum region ($1 \leq s_v \leq s_{wall}$). Only the normal component has to be continuous at the interface; no such constraint is set on η and Y_v respectively.
Once the perturbation components X_v and Y_v have been Fourier decomposed, the stability problem in vacuum is similar in form to that in the plasma. There is no dissociation between the plasma and the vacuum treatement and a single, unified, step is needed to advance the problem toward the solution.

In the original version of TERPSICHORE δW_k was choosen to be the unit matrix (the incompressibility constraint already modifies the eigenvalue) [34]. In the version used in

this study the expression of the kinetic energy is [31]

$$\delta W_k = \frac{1}{2}\int d^3x\, \vec{\xi}\cdot\rho_{\mathbf{M}}\cdot\vec{\xi} \tag{2.41}$$

with the diadic tensor

$$\rho_{\mathbf{M}} = \vec{\nabla}\mathrm{s}\vec{\nabla}\mathrm{s} + \frac{(\mathbf{\Phi}'(\mathrm{s})\vec{\nabla}\theta - \mathbf{\Psi}'(\mathrm{s})\vec{\nabla}\phi)(\mathbf{\Phi}'(\mathrm{s})\vec{\nabla}\theta - \mathbf{\Psi}'(\mathrm{s})\vec{\nabla}\phi)}{[\mathbf{2\Phi}'(\mathrm{s})]^2}$$

A hybrid finite element method is employed for the radial discretization. The variational problem Eq.(2.33) takes the form

$$\mathbf{D}\vec{x} = \lambda\mathbf{K}\vec{x} \tag{2.42}$$

where $\mathbf{D}$ is the potential energy matrix, $\mathbf{K}$ is the kinetic energy matrix, $\vec{x} = (\xi^s, X_v, \eta, Y_v)$ is the eigenfunction and $\lambda = \omega^2$ is the eigenvalue. The Fourier decomposition of the perturbation components (the elements of $\vec{x}$) leads to the appearance in the matrix elements of $\mathbf{D}$ and $\mathbf{K}$ of the double Fourier flux integrals [31] expressing the coupling between the perturbation components. There are nine independent integrals i =0,..8 having the form

$$C^i_{l1\,l2}(s) \approx \frac{2N_{per}}{4\pi^2}\int\int d\phi\, d\theta\, G^i_{m_e,n_e}(s)\, f^i_1(m_e\theta - N_{per}n_e\phi)\, f^i_2(m_{l1}\theta - n_{l1}\phi)\, f^i_3(m_{l2}\theta - n_{l2}\phi) \tag{2.43}$$

Here $G^i_{m_e,n_e}(s)$ are amplitudes associated to the $(m_e, N_{per}n_e)$ mode numbers resulting from the Fourier decomposition of equilibrium quantities in Boozer coordinates. The $_{l1}$ and $_{l2}$ subscripts are linked to perturbations; (m_{l1}, n_{l1}) and (m_{l2}, n_{l2}) are mode numbers that result from the Fourier decomposition of the perturbation in Boozer coordinates. The f^i_1, f^i_2, f^i_3 functions are either the *sin* or *cos* trigonometric functions depending on i.

2.3 The ballooning mode equation and the Mercier criterion

Eq.(2.32) shows that there are two possible sources for MHD instabilities, one proportional to $j_{||}$ and the other to $\vec{\nabla}p$. Among the pressure driven modes the most unstable are those with very short wavelength perpendicular to the magnetic field and long wavelength parallel to the field. These modes are subdivided in two categories: interchange and ballooning. The Mercier criterion represents a necessary condition for stability against the interchange modes i.e. plasma perturbations which are nearly constant along a field line (no line bending) with $k_{||}/k_{\perp} << 1$, $k_{\perp}a >> 1$. Formally it can be derived from an asymptotic analysis of the ballooning mode equation [35]

2.3.1 The ballooning mode equation in Boozer coordinates

The conventional representation of waves with short perpendicular and long parallel wavelength is the eikonal form

$$\vec{\xi_{\perp}} = \vec{\nu} exp(iS)$$

where the ballooning phase factor S is such that

$$\vec{k_{\perp}} = \vec{\nabla}S \qquad \vec{B}\cdot\vec{\nabla}S = 0$$

The quantity S is assumed to vary rapidly on the equilibrium length scale $|a\vec{\nabla}S| >> 1$ whereas the variation of ν is slow $|a\nabla\nu|/|\vec{\nu}| \approx 1$. The starting point for the derivation of the ballooning mode equation for 3D geometries is Eq.(2.32)) with the perpendicular component of the displacement vector decomposed as

$$\xi_{\perp} = \xi_s \frac{\vec{\nabla}S}{|\vec{\nabla}S|^2} + \chi \frac{\vec{B}\wedge\vec{\nabla}S}{B^2} \tag{2.44}$$

After the elimination of the positive definite plasma compression term which means $\vec{B}\cdot\vec{\nabla}(\xi_{||}/B) = -\vec{\nabla}\cdot\vec{\xi_{\perp}}$, the ballooning mode representation [35] is applied to the remaining displacement components

$$\xi_s = (\xi_{s0} + \epsilon\xi_{s1} + \dots)\, exp(\frac{iS}{\epsilon}) \qquad \chi = (\chi_0 + \epsilon\chi_1 + \dots)\, exp(\frac{iS}{\epsilon}) \tag{2.45}$$

where $\epsilon \approx 1/(k_{\perp}a) << 1$. The lowest order $O(1/\epsilon^2)$ contribution to δW_p comes from the

magnetic compression term which is positive and stabilizing unless $\xi_{s0} = 0$. The next non-zero contribution occurs at order $O(0)$. Here again the magnetic compression term is positive definite; it is eliminated by an appropiate choice of ξ_{s1} whith the consequence that the parallel current contribution is set to zero too (at this order). Thus the most unstable modes for $\vec{k_\perp} \to \infty$ do not involve either compression of the magnetic field nor kink terms. The resulting δW_p shows a competition betwen the stabilizing effect of field line bending and the destabilizing effects of unfavourable curvature

$$\delta W_p = \frac{1}{2}\int\int\int d^3x \left\{ \frac{|\vec{\nabla}S^2|}{B^2}\,(\vec{B}\cdot\vec{\nabla}\chi_0)^2 - \frac{\vec{B}\wedge\vec{\nabla}S\cdot\vec{\nabla}p}{B^2}\,\frac{\vec{B}\wedge\vec{\nabla}S\cdot\vec{\kappa}}{B^2}\,\chi_0 \right\} + 0(\epsilon) \quad (2.46)$$

The stability is determined by solving $\delta W_p + \omega^2 \delta W_k = 0$ with δW_k being the kinetic energy in the form adopted in TERPSICHORE (Eq.(2.41)). According to [36] the ballooning phase factor $\vec{\nabla}S$ is expressed as

$$\vec{\nabla}S = \vec{\nabla}\alpha + \theta_k\vec{\nabla}q = \vec{\nabla}\phi - q(s)\vec{\nabla}\theta - q'(s)(\theta-\theta_k)\vec{\nabla}s \quad (2.47)$$

This form given in Boozer coordinates results from the condition $\vec{B}\cdot\vec{\nabla}S = 0$ in a coordinate system with straight field lines. Here $\alpha = \phi - q(s)\theta$ labels a particular field line and θ_k corresponds to the radial wave number. The Euler equation derived from the minimisation of the energy principle becomes

$$\begin{aligned} \frac{\partial}{\partial\theta}\left([C_p + C_s(\theta-\theta_k) + C_q(\theta-\theta_k)^2]\frac{\partial\chi}{\partial\theta}\right) + [d_p + d_s(\theta-\theta_k)]\chi \\ -\omega^2\frac{\sqrt{g}}{[\Psi'(s)]^2}\left\{1 + \left[\frac{q'(s)}{2q(s)}(\theta-\theta_k)\right]^2\right\}\chi \;=\; 0 \end{aligned} \quad (2.48)$$

which is a second order ordinary differential equation with the C_p, C_s, C_q, d_p, d_s coefficients given in [31] (the subscript $_0$ on χ has been dropped). Eq.(2.48) is the ballooning mode equation in Boozer coordinates; the eigenvalue $\omega^2 = \lambda(q,\alpha,\theta_k)$ has to be calculated for each magnetic field line labeled by q and α.

There is an incompatibility between the requirement of periodicity of χ with respect to θ and ϕ the eikonal representation in systems with shear $q'(s) \neq 0$. The condition $\chi(\theta + 2m\pi, \phi + 2n\pi) = \chi(\theta,\phi)$ cannot be satisfied with χ given by Eq.(2.45) combined with Eq.(2.47). A solution to this problem has been offered with the introduction of the

covering space concept. It is shown in [35], [36] that for an eigenvalue problem

$$\mathcal{L}(x,\theta,\phi)\,\zeta(x,\theta,\phi) = \lambda\,\zeta(x,\theta,\phi) \tag{2.49}$$

where the operator $\mathcal{L}$ and the eigenfunction ζ are periodic in θ and ϕ, the transformation

$$\zeta(x,\theta,\phi) = \sum_{m,n} e^{-i(m\theta+n\phi)} \int_{-\infty}^{\infty} d\eta\, d\nu\, e^{i(m\theta+n\phi)}\, \bar{\zeta}(x,\eta,\nu) \tag{2.50}$$

ensures that any solution $\bar{\zeta}(x,\eta,\nu)$ of

$$\mathcal{L}(x,\eta,\nu)\,\bar{\zeta}(x,\eta,\nu) = \lambda\,\bar{\zeta}(x,\eta,\nu) \tag{2.51}$$

in the infinite domain $-\infty < \eta < \infty$, $-\infty < \nu < \infty$ (covering space) generates a periodic solution $\zeta(x,\theta,\phi)$ of Eq.(2.49) with the same eigenvalue λ. The transformation $\zeta \to \bar{\zeta}$ replaces the physical stability problem with its uncomfortable periodicity requirements by an artificial problem in the covering space domain. The operator for the artificial problem is identical with the operator of the physical problem. Because $\bar{\zeta}$ does not have to be periodic, it can be represented in an eikonal form $F(x,\eta,\nu)exp(iS/\epsilon)$ with a slowly varying amplitude $F(x,\eta,\nu)$. The lowest order expansion of F in powers of ϵ gives an ordinary differential equation like Eq.(2.48). The dependence of F with x which is the radial variable appears in the higher order equations [35], [36].

2.3.2 Derivation of the Mercier criterion

In the analysis of the cylindrical screw pinch, Suydam developed a purely analytical criterion [37] depending only on equilibrium profiles which provided a test for stability against localized interchange modes. He showed that for modes localized about a singular surface $\vec{k}\cdot\vec{B} = 0$, the potential energy δW_p of the cylindrical screw pinch is minimized by a function ξ satisfying an Euler-Lagrange equation of the type $\frac{d}{dx}\left(x^2\frac{d\xi}{dx}\right) + D_s\xi = 0$. The solution is expressed as $\xi = c_1 x^{p_1} + c_2 x^{p_2}$, $p_{1,2} = -\frac{1}{2} \pm \frac{1}{2}(1-4D_s)$ where $x = r - r_{res}$ measures the distance from the resonant surface and D_s is given in [38]. For $1-4D_s < 0$ the roots are complex, ξ oscillates infinitely rapidly as $x \to 0$ and a trial function can be constructed which makes δW_p negative i.e. unstable. The condition $1-4D_s > 0$ is known the Suydam criterion and and its violation for any r in $(0,a)$ means instability. The study made by Newcomb [39] showed later that the knowledge of the radial dependence of ξ

determined from the general Euler-Lagrange equation

$$\frac{d}{dr}\left(f\frac{d\xi}{dr}\right) + g\xi = 0 \tag{2.52}$$

can be used to derive a set of necesary and sufficient conditions for the stability of the internal modes. One of his theorems states that if a solution of Eq.(2.52) which vanishes at r_1 also vanishes at some other point in an interval (r_1, r_2) containing no singular points, then a trial function can be constructed such that $\delta W_p < 0$ in (r_1, r_2).

Based on Newcomb's study and generalizing Suydam's analysis, the Mercier criterion [40] was derived as an interchange stability criterion for a more general toroidal geometry. The independent angular variable θ of the ballooning mode formalism replaces the radial variable x of the Suydam analysis and the ballooning mode equation is studied in the limit where θ is very large. A non-oscillatory behaviour of the solution χ which is regular at $\pm\infty$ is required as a necessary condition for stability. Following the developements of Connor *et al.* [35] the expansion

$$\chi = \bar{\theta}^{\alpha}\left[X_0 + \frac{X_1}{\bar{\theta}} + \frac{X_2}{\bar{\theta}} + ...\right] \tag{2.53}$$

is introduced in Eq.(2.48) and the resulting equation is solved order by order. Here $\bar{\theta} = \theta - \theta_k \to \infty$, the functions X_0, X_1, ... satisfy the same periodicity as the equilibrium and α is the indicial coefficient to be determined. At the dominant order $O(\bar{\theta}^{\alpha+2})$, one obtains $X_0 = 1$; the next order $O(\bar{\theta}^{\alpha+1})$ gives an equation for $\partial X_1/\partial\bar{\theta}$. At $O(\bar{\theta}^{\alpha})$, after averaging over a flux surface, the indicial equation for α is obtained

$$\alpha^2 + \alpha + D_M = 0 \tag{2.54}$$

with D_M given in [31]. The roots of this equations are $\alpha = -\frac{1}{2} \pm \frac{1}{2}(1 - 4D_M)$ and the transition from oscillatory to non oscillatory behaviour occurs for $D_M = 1/4$. Therefore the Mercier criterion for interchange stability is expressed by

$$D_M < \frac{1}{4} \tag{2.55}$$

Chapter 3

Configurations studied

The aim of this chapter is to present the configurations which were studied and to explain why they were chosen in particular. The parameters specifying the geometry and the equilibrium profiles are described together with the selection of the stability modes to be investigated.

3.1 Types of helical boundary deformations

In the following chapters the expressions "$L = l+1$ configuration" or "$L = l+1$ boundary deformation" will be frequently encountered. They means that if the R, Z coordinates are Fourier decomposed as in Eq.(2.8) the only non-zero components apart (0,0) and (1,0) are $(l, l \pm 1)$ (the helical magnetic field is essentially described by the $L = l$ helicity component). In our study, the principal helical boundary deformations belonged to the

- L=2 type

$$\begin{cases} R(s=1,u,v) &= R_0 + cosu + \delta_2 \left(cos(u) + cos(u - 2N_{per}v)\right) \\ Z(s=1,u,v) &= sinu + \delta_2 \left(sin(u) - sin(u - 2N_{per}v)\right) \end{cases} \tag{3.1}$$

- L=3 type

$$\begin{cases} R(s=1,u,v) &= R_0 + cosu + \delta_3 \left(cos(2u - N_{per}v) + cos(2u - 3N_{per}v)\right) \\ Z(s=1,u,v) &= sinu + \delta_3 \left(sin(2u - N_{per}v) - sin(2u - 3N_{per}v)\right) \end{cases} \tag{3.2}$$

where R and Z are the cylindrical coordinates of a boundary point as functions of the radial flux coordinate s and the poloidal and toroidal geometrical angles u and v. N_{per} is the number of equilibrium field periods and δ_2 and δ_3 are parameters measuring the plasma boundary deformation. If $\delta_2 = 0$, $\delta_3 = 0$ the boundaries are circular. In our study

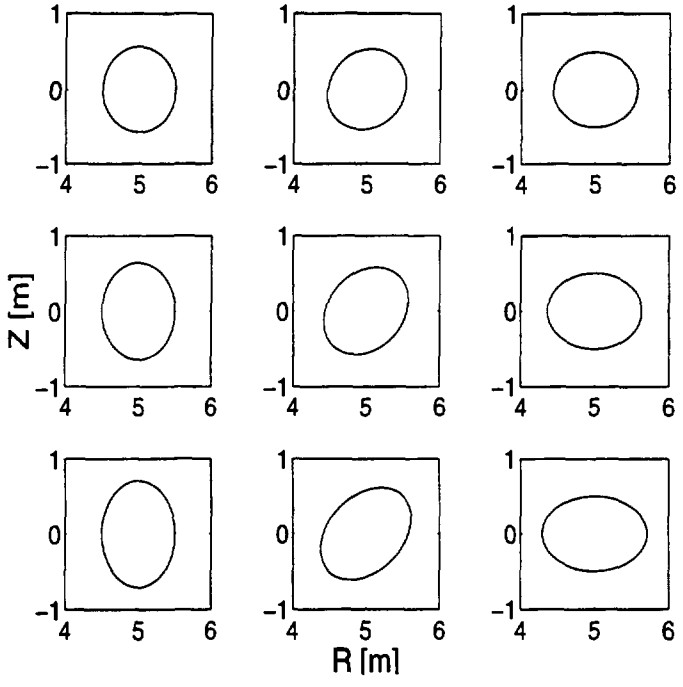

Figure 3.1: **boundary for L=2 configuration** *at three toroidal angles* $0,\ 3\pi/(4N_{per}),\ 7\pi/(4N_{per})$ *horizontally and three values for the deformation parameter* $\delta_2 = 0.07,\ 0.014,\ 0.210$ *- vertically*

typical values range between $0 \leq \delta_2 \leq 0.35$ and $0 \leq \delta_3 \leq 0.14$. Fig.3.1 and Fig.3.2 show some $L = 2$ and a $L = 3$ boundaries resulting from the formulas above.

We also tested some configurations with boundaries corresponding to

- a $L = 1$ type

$$\begin{cases} R(s=1,u,v) &= R_0 + cosu + \delta_1 cos(N_{per}v) \\ Z(s=1,u,v) &= sinu - \delta_1 sin(N_{per}v) \end{cases} \tag{3.3}$$

- a mixture between $L = 2$ and $L = 3$ types

$$\begin{cases} R(s=1,u,v) &= R_0 + cosu + \delta_2\,(cosu + cos(u - 2N_{per}v)) \\ &\quad +\delta_3\,(cos(2u - N_{per}v) + cos(2u - 3N_{per}v)) \\ Z(s=1,u,v) &= sinu + \delta_2\,(sinu - sin(u - 2N_{per}v)) \\ &\quad +\delta_3\,(sin(2u - N_{per}v) - sin(2u - 3N_{per}v)) \end{cases} \tag{3.4}$$

Other types of boundary deformations were not considered. For larger L the boundary shapes become exotic and difficult to realise with a reasonable system of coils; also for $L \geq 4$ even, there exists a threshold value δ_L which is low and decreases with L, such

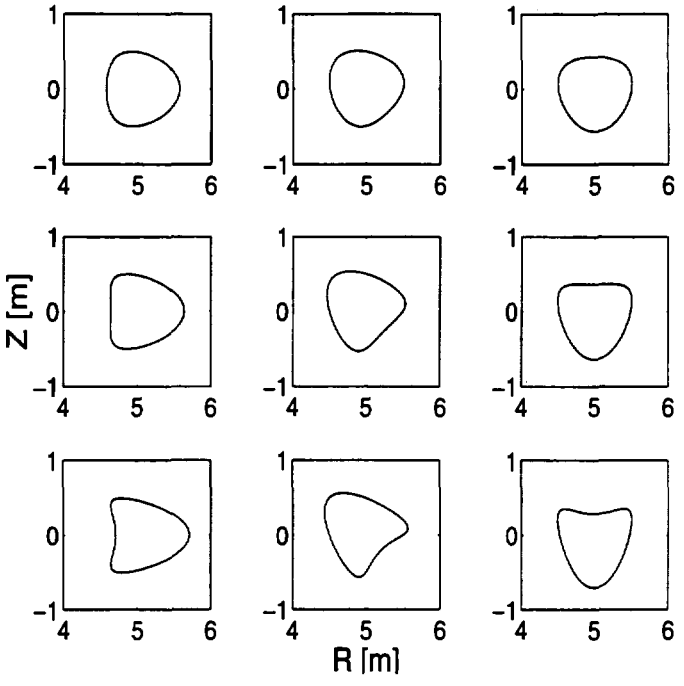

Figure 3.2: **boundary for L=3 configuration** *at three toroidal angles* 0, $3\pi/(4N_{per})$, $7\pi/(4N_{per})$ *horizontally and three values for the deformation parameter* $\delta_3 = 0.035,\ 0.07,\ 0.105$ *- vertically*

that for a deformation parameter $\delta \geq \delta_L$ the boundary surface intersects itself several times. If $\delta = 0$, we define the quantity $\epsilon_c = 1/R_0$ as the inverse aspect ratio of the circular tokamak. During the stability analysis, families of equilibria were generated with the following value for $1/\epsilon_c$: 5, 8, 10, 13 and 17. When δ increases, the average minor radius is changed so the effective inverse aspect ratio ϵ is different from ϵ_c.

3.2 Number of field periods and families of unstable modes

The $C^i_{lk}(s)$ integrals from Eq.(2.43) are non-zero only if the $(m_e, N_{per}n_e)$, (m_{l1}, n_{l1}) and (m_{l2}, n_{l2}) mode numbers are coupled via relations like :$m_e \pm m_{l1} \pm m_{l2} = 0$ and $N_{per}n_e \pm n_{l1} \pm n_{l2} = 0$. The Fourier decomposition is such that $m_j \geq 0$ and $n_j \geq 0$ if $m_j = 0$ with $j = e,\ l1,\ l2$. This reduces the preceding relations to:

$$\begin{aligned} m_e &= m_{l1} \pm m_{l2} \\ n_e N_{per} &= n_{l1} \pm n_{l2} \end{aligned} \tag{3.5}$$

This means that in a geometry with N_{per} field periods, a partial decoupling between modes occurs, based on the values of the toroidal Fourier mode numbers. Modes with toroidal numbers n_{l1} and n_{l2} produce non-vanishing integral terms i.e. they belong to the same family, if (3.5) is respected.
The number of independent mode families N_{fam} is limited and determined by the number of equilibrium field periods. It is easy to verify that

$$N_{fam} = \begin{cases} N_{per}/2 + 1 & N_{per} = 2p \\ (N_{per} - 1)/2 + 1 & N_{per} = 2p + 1 \end{cases} \tag{3.6}$$

If k labels one of these families, the modes belonging to it will have a toroidal mode number given by

$$n_i = n_i(k, N_{per}) = iN_{per} \pm k \quad i = .., -1, 0, 1, .. \quad k \in \{0, N_{fam}\}. \tag{3.7}$$

Some of these values are given in 3.1 for $N_{per} = 2,..8$. The following remarks can be made:
• N_{fam} increases with the number of field periods. If $N_{per} = 1$ there is only one family containing all the modes, if $N_{per} = 2$ or 3, two families are present, for $N_{per} = 4$ or 5 there are three families and so on.
• The toroidal mode numbers are unequally distributed among the families. The special $k = 0$ family is degenerate and contains only modes with $n_l = \pm iN_{per}$ which on average (for $N_{per} \geq 3$) has two times less modes than the other families. If N_{per} is even the family $k = N_{fam} = N_{per}/2$ contains is also degenerate and contains in average two times less values of n than the other $k = 1, .., N_{fam} - 1$ families.
• For any fixed family k, let $\Delta(i, k, N_{per}) = n_{i+1}(k, N_{per}) - n_i(k, N_{per})$ be the difference between two adjacent mode numbers; then on average Δ increases with N_{per}.

From the observations above we deduce that, in stability calculations, a small N_{per} is more complicated to treat than a larger N_{per}. When N_{per} decreases there are fewer families and inside each family more and more n 's with close values. The larger number of mode couplings complicates the physics of the problem and requires more computational resources.

For these reasons we did not investigate configurations with $N_{per} = 2$ or 3 but we chose $N_{per} = 4$ and 5 because these values are common to most torsatrons and stellarators (TJ-II [5], W7X, etc). We skipped $N_{per} = 6$ because of the unbalance in the number of

N_{per}	k_{family}	n															
2	0	-6	-6	-4	-4	-2	-2	0	0	2	2	4	4	6	6	8	8
2	1	-7	-5	-5	-3	-3	-1	-1	1	1	3	3	5	5	7	7	9
3	0	-9	-9	-6	-6	-3	-3	0	0	3	3	6	6	9	9	12	12
3	1	-10	-8	-7	-5	-4	-2	-1	1	2	4	5	7	8	10	11	13
4	0	-12	-12	-8	-8	-4	-4	0	0	4	4	8	8	12	12	16	16
4	1	-13	-11	-9	-7	-5	-3	-1	1	3	5	7	9	11	13	15	17
4	2	-14	-10	-10	-6	-6	-2	-2	2	2	6	6	10	10	14	14	18
5	0	-15	-15	-10	-10	-5	-5	0	0	5	5	10	10	15	15	20	20
5	1	-16	-14	-11	-9	-6	-4	-1	1	4	6	9	11	14	16	19	21
5	2	-17	-13	-12	-8	-7	-3	-2	2	3	7	8	12	13	17	18	22
6	0	-18	-18	-12	-12	-6	-6	0	0	6	6	12	12	18	18	24	24
6	1	-19	-17	-13	-11	-7	-5	-1	1	5	7	11	13	17	19	23	25
6	2	-20	-16	-14	-10	-8	-4	-2	2	4	8	10	14	16	20	22	26
6	3	-21	-15	-15	-9	-9	-3	-3	3	3	9	9	15	15	21	21	27
7	0	-21	-21	-14	-14	-7	-7	0	0	7	7	14	14	21	21	28	28
7	1	-22	-20	-15	-13	-8	-6	-1	1	6	8	13	15	20	22	27	29
7	2	-23	-19	-16	-12	-9	-5	-2	2	5	9	12	16	19	23	26	30
7	3	-24	-18	-17	-11	-10	-4	-3	3	4	10	11	17	18	24	25	31
8	0	-24	-24	-16	-16	-8	-8	0	0	8	8	16	16	24	24	32	32
8	1	-25	-23	-17	-15	-9	-7	-1	1	7	9	15	17	23	25	31	33
8	2	-26	-22	-18	-14	-10	-6	-2	2	6	10	14	18	22	26	30	34
8	3	-27	-21	-19	-13	-11	-5	-3	3	5	11	13	19	21	27	29	35
8	4	-28	-20	-20	-12	-12	-4	-4	4	4	12	12	20	20	28	28	36

Table 3.1: *Coupling of modes into families depending on the number of equilibrium field periods N_{per}. The different families are indexed by k. Only a few number of toroidal mode numbers n are shown.*

modes between the $k = 1, 2$ and $k = 0, 3$ families and prefered the next value $N_{per} = 7$ to it. Larger values were not considered in the study.

3.3 Modes studied

Let us consider a sequence of equilibrium calculations which have identical input parameters with the exception of the amount of boundary deformation δ. Suppose that δ is monotonically increased from zero to a certain final value; the consequence will be that the q profile decreases between the first and the last equilibrium of the sequence and this variation can be quite large. For a given family, several (m_l, n_l) perturbation components with different m_l/n_l resonances can be destabilized when going through the entire equilibrium sequence. Already at moderate values of the deformation parameter, i.e. δ between one third to one half of the ranges given for δ_2 and δ_3 at the beginning of this section, the q profile is sufficiently low such that the most unstable modes are $(n+1, n)$ where n can be 1, 2, 3, ... We decided therefore to limit the investigations only to these modes, in the region where they are excited i.e the $q \leq 2$ region. We recall that in tokamaks, $q_{edge} \simeq 2$ is a stability limit imposed by the external kinks at $\beta << 1$.

Let (m, n) be the particular mode studied and let us consider the ensemble of all the perturbation components (m_l, n_l) which are coupled to (m, n) via the N_e equilibrium terms $(m_e, N_{per} n_e)$. Here N_e represents the number of Fourier coefficients needed in TERPSICHORE for an accurate reconstruction of the equilibrium in Boozer coordinates.
The expression (m, n) mode means that the (m, n) Fourier component of the perturbation (in Boozer coordinates) is dominant with respect to the other components.

The values of n_l are determined by the condition that n_l and n belong to the same family. If the equilibrium Fourier series are not truncated (N_e unlimited), there is no upper limit for m_l or n_l and the above mentioned ensemble should contain an infinite number of modes. However, in a numerical computation N_e is finite which implies that the number of (m_l, n_l) modes is limited too.
In TERPSICHORE we chose to decompose the perturbations in Fourier series in the following way :
1) the toroidal mode numbers are limited to an inteval $n_l^{min} \leq n_l \leq n_l^{max}$ where $n_l^{min} \simeq -20$ and $n_l^{max} \simeq 30$.
2) the poloidal mode numbers are bounded by $0 \leq m_l \leq m_l^{max} \simeq 25$.
The ensemble of (m_l, n_l) perturbation components which is left after the selection following the choice of the N_e equilibrium components, and the truncation of the perturbation Fourier series, will be denoted by $\mathcal{T}^0_{m,n}$.

n	m_l/n_l resonances						
1	2/1	...					
3	4/3	5/3	6/3	...			
5	6/5	7/5	8/5	9/5	10/5	...	
7	8/7	9/7	10/7	11/7	12/7	13/7	...
9	10/9	11/9	12/9	13/9	14/9	15/9	...
11	12/11	13/11	14/11	15/11	16/11	17/11	...
...	...						

Table 3.2: *Values of the toroidal mode number n_l of perturbation components from the same family as the studied $(m,n) = (2,1)$ mode in a configuration with $N_{per} = 4$ and some m_l/n_l resonances of components which could be coupled with the (2,1) mode in the $q < 2$ region.*

n	m_l/n_l resonances						
1	2/1	...					
4	5/4	6/4	7/4	...			
6	7/6	8/6	9/6	10/6	11/6	...	
9	10/9	11/9	12/9	13/9	14/9	15/9	...
11	12/11	13/11	14/11	15/11	16/11	17/11	...
14	15/14	16/14	17/14	18/14	19/14	20/14	...
...	...						

Table 3.3: *The same as in Tab.(3.2) but for $N_{per} = 5$.*

The next step is the elimination from $\mathcal{T}^0_{m,n}$ of those perturbation components which are coupled to (m,n) via negligible $(m_e, N_{per}n_e)$ equilibrium terms. We suppose that, if the amplitude of a particular equilibrium component is smaller than $10^{-7} - 10^{-8}\times$ the amplitude of the dominant equilibrium component, then the related (m_l, n_l) perturbation component will lead to negligible $(m,n) \times (m_l, n_l)$ coupling contributions to the potential energy. This hypothesis will be further discussed in Chapter 4. The (m_l, n_l) ensemble resulting from these operations is denoted by $\mathcal{T}_{m,n}$ and represents the minimal reasonable set of perturbation components needed for the numerical study of the particular (m,n) mode. Thus, retaining a (m_l, n_l) component in $\mathcal{T}_{m,n}$ depends not only on the mode studied and the number of field periods but also on other equilibrium properties. In particular, the type of plasma boundary deformation has a strong impact on the hierarchy of the $(m_e, N_{per}n_e)$ equilibrium terms following the dominant $(0,0)$ and $(1,0)$ components.

The study of (m,n) modes with $m = n+1$ requires the $\mathcal{T}_{n+1,n}$ set. In principle the $\mathcal{T}_{n+1,n}$ sets cannot be used for the study of modes with poloidal and toroidal mode numbers

n	m_l/n_l resonances						
2	3/2	4/2	...				
6	7/6	8/6	9/6	10/6	...		
10	11/10	12/10	13/10	14/10	15/10	16/10	...
14	15/14	16/14	17/14	18/14	19/14	20/14	...
18	19/18	20/18	21/18	22/18	...		
...	...						

Table 3.4: *Values of the toroidal mode number n_l of modes perturbation components from the same family as the studied $(m,n) = (3,2)$ mode in a configuration with $N_{per} = 4$ and some m_l/n_l resonances of components which could be coupled with the (2,1) mode in the $q < 2$ region.*

n	m_l/n_l resonances						
2	3/2	4/2	...				
3	4/3	5/3	6/3	...			
7	8/7	9/7	10/7	11/7	12/7	13/7	...
8	9/8	10/8	11/8	12/8	13/8	14/8	...
12	13/12	14/12	15/12	16/12	17/12	18/12	...
13	14/13	15/13	16/13	17/13	18/13	19/13	...
...	...						

Table 3.5: *The same as in Tab.(3.4) but for $N_{per} = 5$.*

different from m or n. Nevertheless, if for a given equilibrium, the $(n+2,n)$ component becomes dominant the calculated growth rate or radial structure can be considered valid even if $\mathcal{T}_{n+1,n} \neq \mathcal{T}_{n+2,n}$. The justification is based on the fact that the difference between the two sets consists only in a few (m_l, n_l) components such that the couplings with $(n+1,n)$ or $(n+2,n)$ occur via small $(m_e, N_{per}n_e)$ equilibrium terms. This can be true even when the $(m \geq n+3, n)$ components are dominant but this depends strongly on the value of n and on the equilibrium geometry.

A particular category of components belonging to $\mathcal{T}^0_{m,n}$ (or $\mathcal{T}_{m,n}$) deserves special attention. This category is formed by those components with (m_l, n_l) resonant values in the region of interest i.e. $1 < q < 2$. The most important of them are given in tables Tab.(3.2) to Tab.(3.5) for $(m,n) = (2,1)$, $(3,2)$ and for $N_{per} = 4$, 5. Only some of the values satisfying $1 < m_l/n_l \leq 2$ are displayed. If we eliminate from the $\mathcal{T}_{m,n}$ set all (m_l, n_l) components with $m_l > n_l > n$ we obtain a new set which is be denoted by $\mathcal{T}^{nores}_{m,n}$. The reason for doing this and the role of $\mathcal{T}_{m,n}$ and $\mathcal{T}^{nores}_{m,n}$ will be discussed in detail in Chapter 3.

Generally, if the $q_r = m_l/n_l$ resonance is situated in the vicinity of the plasma boundary, the (m_l, n_l) component is strongly destabilized. The importance of the contribution of the $(m,n) \times (m_l, n_l)$ coupling to the potential energy depends then on the amplitude of the $(m_e, N_{per}n_e)$ equilibrium component obtained by inverting Eq.(3.5). We denote by $(m_{e1}, N_{per}n_{e1})$ the pair obtained with the "-" sign, and by $(m_{e2}, N_{per}n_{e2})$ the pair obtained with the "+" sign. Only one of the two pairs can satisfy the periodicity requirement and we drop the indices (1 or 2) and refer to it as $(m_e, N_{per}n_e)$

If the amplitude of the $(m_e, N_{per}n_e)$ component is non negligible then there is a good chance that the behaviour of the (m,n) mode will be influenced by the (m_l, n_l) mode at least in the region where the latter is excited.
Tab.(3.6) to Tab.(3.9) show what these equilibrium coupling components are for the most dangerous m_l/n_l resonances in the cases where $(m,n) = (2,1)$, $(3,2)$ and for configurations with $N_{per} = 4$ and 5. For example it can be seen from Tab.(3.6) that the $(2,1)$ mode in a configuration with $N_{per} = 4$ is coupled to modes with $n_l = 3$ and 5 via $(m_e, N_{per}n_e)$ terms with $n_e = 1$. The couplings with the next values for n_l namely 7 and 9 require the presence of $n_e = 2$. Similarily, Tab.(3.9) shows that the $(3,2)$ mode in a configuration with $N_{per} = 5$ is coupled to modes with $n_l = 4$ and 6 via $n_e = 1$. The coupling with $n_l = 9$ and 11 occurs via $n_e = 2$.

We repeat below, for convenience, the definitions of the various $\mathcal{T}$ sets

- $\mathcal{T}^0_{m,n}$ - set of (m_l, n_l) perturbation components needed to study the (m,n) mode when the equilibrium is calculated with N_e Fourier components. It is obtained by taking all possible combinations from Eq.(3.5) and retaining only that m_l and n_l values which are inside the limits imposed by the truncation of the Fourier series.

- $\mathcal{T}_{m,n}$ - the set resulting from $\mathcal{T}^0_{m,n}$ when the (m_l, n_l) components which couple to (m,n) via negligible $(m_e, N_{per}n_e)$ are eliminated. The (m_l, n_l) components from $\mathcal{T}^0_{m,n}$ with $m_l > n_l > n$ are however retained.(the previous definition of $\mathcal{T}_{m,n}$ does not contain this last aspect).

- $\mathcal{T}^{nores}_{m,n}$ - the set resulting from $\mathcal{T}_{m,n}$ when the (m_l, n_l) components with $m_l > n_l > n$ are eliminated.

(m_l, n_l)	(m_{e1}, n_{e1})	(m_{e2}, n_{e2})	(m_l, n_l)	(m_{e1}, n_{e1})	(m_{e2}, n_{e2})
(2 1)	(0 0)	-	(10 7)	-	(12 2)
...	...	...	(11 7)	-	(13 2)
(4 3)	-	(6 1)	...	...	...
(5 3)	-	(7 1)	(10 9)	(8 2)	-
(6 3)	-	(8 1)	(11 9)	(9 2)	-
...	...	...	(12 9)	(10 2)	-
(6 5)	(4 1)	-	(13 9)	(11 2)	-
(7 5)	(5 1)	-	...	...	...
(8 5)	(6 1)	-	(12 11)	-	(14 3)
(9 5)	(7 1)	-	(13 11)	-	(15 3)
...	...	...	(14 11)	-	(16 3)
(8 7)	-	(10 2)	(15 11)	-	(17 3)
(9 7)	-	(11 2)	...	...	...

Table 3.6: *Some perturbation components with $m_l/n_l \leq 2$ resonant values and corresponding equilibrium coupling terms $(m_e, N_{per}n_e)$ ((m_{e1}, n_{e1}) or (m_{e2}, n_{e2}) depending on the $\pm$ sign in Eq.(3.5)) for $(m, n) = (2, 1)$ and $N_{per} = 4$. The equilibrium toroidal mode numbers correspond to one field period. A "-" means that n, n_l and the corresponding n_{ei} cannot satisfy the periodicity requirements imposed by Eq.(3.5)*

(m_l, n_l)	(m_{e1}, n_{e1})	(m_{e2}, n_{e2})	(m_l, n_l)	(m_{e1}, n_{e1})	(m_{e2}, n_{e2})
(2 1)	(0 0)	-	...	...	...
...	...	...	(10 9)	-	(12 2)
(5 4)	-	(7 1)	(11 9)	-	(13 2)
(6 4)	-	(8 1)	(12 9)	-	(14 2)
(7 4)	-	(9 1)	(13 9)	-	(15 2)
(8 4)	-	(10 1)	...	...	...
...	...	...	(12 11)	(10 2)	-
(7 6)	(5 1)	-	(13 11)	(11 2)	-
(8 6)	(6 1)	-	(14 11)	(12 2)	-
(9 6)	(7 1)	-	(15 11)	(13 2)	-
(10 6)	(8 1)	-	...	...	...

Table 3.7: *the same as in Tab.(3.6) but for $N_{per} = 5$; the equilibrium toroidal mode numbers correspond to one field period.*

(m_l, n_l)	(m_{e1}, n_{e1})	(m_{e2}, n_{e2})	(m_l, n_l)	(m_{e1}, n_{e1})	(m_{e2}, n_{e2})
(3 2)	(0 0)	(6 1)	(10 6)	(7 1)	(13 2)
(4 2)	(1 0)	(7 1)	...	...	...
...	...	...	(11 10)	(8 2)	(14 3)
(7 6)	(4 1)	(10 2)	(12 10)	(9 2)	(15 3)
(8 6)	(5 1)	(11 2)	(13 10)	(10 2)	(16 3)
(9 6)	(6 1)	(12 2)	(14 10)	(11 2)	(17 3)

Table 3.8: *Some perturbation components with $m_l/n_l \leq 2$ resonant values and corresponding equilibrium coupling terms $(m_e, N_{per} n_e)$ ((m_{e1}, n_{e1}) or (m_{e2}, n_{e2}) depending on the $\pm$ sign in Eq.(3.5)) for $(m, n) = (3, 2)$ and $N_{per} = 4$. The equilibrium toroidal mode numbers correspond to one field period. A "-" means that n, n_l and the corresponding n_{ei} cannot satisfy the periodicity requirements imposed by Eq.(3.5)*

(m_l, n_l)	(m_{e1}, n_{e1})	(m_{e2}, n_{e2})	(m_l, n_l)	(m_{e1}, n_{e1})	(m_{e2}, n_{e2})
(3 2)	(0 0)	-	...	...	...
(4 2)	(1 0)	-	(9 8)	-	(12 2)
...	...	...	(10 8)	-	(13 2)
(4 3)	-	(7 1)	(11 8)	-	(14 2)
(5 3)	-	(8 1)	(12 8)	-	(15 2)
(6 3)	-	(9 1)	...	...	...
...	...	...	(13 12)	(10 2)	-
(8 7)	(5 1)	-	(14 12)	(11 2)	-
(9 7)	(6 1)	-	(15 12)	(12 2)	-
(10 7)	(7 1)	-	(16 12)	(13 2)	-
(11 7)	(8 1)	-	...	...	...

Table 3.9: *the same as in Tab.(3.8) but for $N_{per} = 5$; the equilibrium toroidal mode numbers correspond to one field period.*

3.4 Current and pressure profiles

After the amount of plasma boundary deformation, the toroidal current density was the second most important parameter considered in the analysis. We prescribed it with a expression allowing a large flexibility of profiles:

$$J(s) = a_1 (1 - s^{a_2})^{a_3} + a_4 (1 - s^{a_5})^{a_6} \tag{3.8}$$

where a_1,..,a_6 are free parameters. Some profiles were systematically used throughout the whole study. They are given by the following choices of a_i , $i = 2,..6$:

• $a_2 = 1.2$, $a2 = 3$ $a_4 = ..= a_6 = 0$ corresponding to a peaked profile with very small gradient in the exterior region of the plasma, near the boundary.

• $a_2 = 2.5$, $a_3 = 2$ $a_4 = ..= a_6 = 0$ representing an intermediate form between peaked and broad profiles.

• $a_2 = 20$, $a_3 = 8$ $a_4 = ..= a_6 = 0$ yieldind a broad profile with a negligible gradient in the main part of the plasma volume and falling sharply near the edge.

• $a_2 = 10$, $a_3 = 2$, $a_5 = 2.5$, $a_6 = 2$, $sign(a_4) \neq sign(a_1)$ corresponding to a hollow current profile relatively flat in the central region and and maximum near the plasma edge.

• $a_2 = 2$, $a_3 = 2$, $a_5 = 1.2$, $a_6 = 8$, $sign(a_4) \neq sign(a_1)$ corresponding to a hollow current profile with a maximum relatively close to the magnetic axis.

The curent densitiey profiles for the combinations of the a_i's given above are shown in Appendix A

The direction of the current flow was chosen such that increasing it or augmenting δ has the same effect on q, namely it diminishes the inverse rotational transform.

Two pressure profiles were used in the computations

$$p(s) = \frac{p_0}{2}[(1 - s)^2 + (1 - s^2)^2] \tag{3.9}$$

$$p(s) = p_0(1 - s^2) \tag{3.10}$$

where p_0 is the pressure on the magnetic axis. We denote by pr^A the first profile and by pr^B the second profile; the pressure gradient is zero at the axis for pr^B and zero at the plasma edge for pr^A.

The values chosen for β were 1% and 2%.

Chapter 4

Investigation procedure

The results of this work, have been obtained from hundreds of runs of the equilibrium and stability codes. We describe in this chapter how the space of parameters was scanned and the looping procedure chosen to systemize the study. Important properties of the configurations studied which determined the investigation method are discussed too. Finally, numbers concerning the pure numerical aspect and the procedures needed to verify the accuracy of the results are described.

4.1 Variation of equilibrium parameters

The study consisted in a regular and systematic exploration of the space of equilibrium parameters. The list of parameters is repeated here for convenience :

- the type and amount of plasma boundary deformation
- the number of equilibrium field periods
- the type of pressure profile and the value of β,
- the type of current density profile and its magnitude
- the starting value of the inverse aspect ratio ϵ_c

Equilibrium sequences were calculated by varying these quantities in the following way:
1) The general features of the configuration i.e. the type of boundary deformation, the number of equilibrium field periods and the inverse aspect ratio of the circular tokamak ϵ_c are specified.
2) The pressure profile and the value of β are chosen next.
3) For every combination of parameters from 1) and 2), a general current profile is prescribed with the choice of a_2 and a_3; for hollow profiles, a_5 and a_6 are also specified. In

the last case the difference between the maximum current density and its value on axis is determined by $|a_1| - |a_4|$.
4) Once the a_i, i=2,..,6 are fixed the toroidal plasma current is varied by changing a_1.
5) For every choice specified with 1), 2) and 3), the amount of boundary deformation is monotonically increased by

$$\delta_i = \delta_{start} + i\,\Delta\delta(i) \qquad i = 0, 1, .. \tag{4.1}$$

where δ_{start} is the first value of the sequence; it is equal to zero if the sequence starts with the circular tokamak. $\Delta\delta(i)$ is chosen piecewise constant with larger values at the beginning of the sequence and smaller values in the "regions of interest".
The reason for taking $\delta_{start} > 0$ comes from the fact that for small and peaked currents and $1/\epsilon_c \geq 10$ at $\beta \geq 1\%$, the circular tokamak equilibrium may not exist: VMEC does not converge or the equilibria have very large Shafranov shifts ($\geq 20 - 25\%$) such that we prefer to start the sequence from a more reliable equilibrium. When the current and β are fixed, the increase of the boundary deformation diminishes the Shafranov shift.

Preliminary runs of TERPSICHORE are performed in order to identify and select the Fourier modes needed for the equilibrium reconstruction in Boozer coordinates as well as the $\mathcal{T}_{m,n}$ set of modes required for the stability analysis of the $(m,n) = (2,1)$, $(3,2)$ and $(4,3)$ modes.
The looping procedure consists in specifying first the N_{per}, L, $1/\epsilon_c$, β parameters, the pressure and current profiles and iterating thereafter over the value of δ given by Eq.(4.1). For each equilibrium thus produced TERPSICHORE is called to calculate the global stability and the Mercier criterion. We are looking for the maximum instability growth rate and identify the dominant unstable mode(s). Ballooning stability is also tested in a certain number of cases.

4.2 Special features of the configurations studied

The discussion in Section 3.4 concerning the tables Table(3.6) to Table(3.9) is continued here but we proceed in a different way. Instead of starting from the m_l/n_l resonances which may appear in the $q < 2$ region and determine from them the $(m_e, N_{per}n_e)$ components, we identify first the $(m_e, N_{per}n_e)$ components necessary for the correct representation of the equilibrium in Boozer coordinates. This is done by iteratively running TERPSICHORE until the desired results concerning the spectrum of equilibrium components are obtained. After we have decided what (m,n) mode will be studied, we identify the (m_{l1}, n_{l1}) and

(m_{l2}, n_{l2}) perturbation components resulting from inverting Eq.(3.5)

$$\begin{aligned} m_{l1,l2} &= m_e \mp m \qquad m_{l1,l2} \geq 0 \\ n_{l1,l2} &= N_{per} n_e \mp n \end{aligned} \tag{4.2}$$

Tab.(B.1) to Tab.(B.3) show these modes for configurations with different $N_{per} = 4$, 5 and $L = 2$, for the cases $(m, n) = (2, 1)$ and $(3, 2)$. The equilibrium quantity whose Fourier amplitudes are represented corresponds to the Jacobian $\sqrt{g}$ in Boozer coordinates; the values are taken at the plasma boundary $s = 1$. We have chosen this quantity because it appears frequently in the flux tube integrals Eq.(2.43). The values of the equilibrium toroidal mode numbers have been represented per field period (m_e, n_e instead of m_e, $N_{per} n_e$). For lack of space only 120 Fourier components are represented; they are listed in the order of increasing m_e. The following observations can be made :

• **Tab.(B.1) and Fig.4.1**: study of the $(2, 1)$ mode in a $L = 2$ configuration with $N_{per} = 5$, $1/\epsilon_c = 5$. The $\sqrt{g}_{m_e,n_e}$ amplitudes whith $n_e = 1$ are extremely low $\simeq 10^{-12}$ to 10^{-13} $\forall m_e$. The corresponding perturbation components coupled to $(2, 1)$ are those with $n_l = 4$ or 6; for $m_e \geq 5$, $(m_l, 6)$ components with $m_l > 6$ are involved and for $m_e \geq 7$, $(m_l, 4)$ components with $m_l > 4$ are present. The couplings $(2, 1) \times (m_e, 4)$ or $(2, 1) \times (m_e, 6)$ are then extremely weak. The table displays $(m_e, 1)$ amplitudes and related perturbation components only for $m_e < 11$.
The $\sqrt{g}_{m_e,n_e}$ amplitudes which are non negligible have even values of n_e. When $n_e = 2$ only perturbations components with toroidal mode numbers $n_l = 9$ and 11 are involved in couplings. $m_l/11$, $m_l > 11$ resonances appear for $m_e \geq 10$ and $m_l/9$, $m_l > 9$ resonances appear for $m_e \geq 12$. It can be seen from the table that $\sqrt{g}_{10,2} \simeq 10^{-6}$ and $\sqrt{g}_{12,2} \simeq 10^{-7}$; these values remain very low compared with the dominant $\sqrt{g}_{m_e,n_e}$ which are of the order $\simeq 10^0$ - see Fig.4.1. If the q profile is such that the $(10, 9)$, $(11, 9)$, .. or $(13, 12)$, $(14, 12)$, .. modes are excited, it is highly probable that their coupling to $(2, 1)$ continue to be very weak.
The discussion can be continued for resonances with higher toroidal mode number.
- for $n_l = 14$, 16, 24, .. involving odd m_e's the corresponding $\sqrt{g}_{m_e,n_e}$ are $< 10^{-14}$
- for $n_l = 19$, 21, 29, .. involving even m_e's the corresponding $\sqrt{g}_{m_e,n_e}$ such that $m_l/n_l > 1$ are effectively less than $\sqrt{g}_{10,2} \simeq 10^{-6}$.
In each case the $(2, 1) \times (m_l, n_l)$ couplings with $m_l/n_l > 1$ occur via $\sqrt{g}_{m_e,n_e}$ amplitudes which are more and more negligible with increasing n_l.

• **Tab.(B.2) and Fig.4.2**: study of the $(2, 1)$ mode in a mixed $L = 2$ and $L = 3$ configuration with $N_{per} = 4$. The difference with the preceeding $L = 2$ configuration

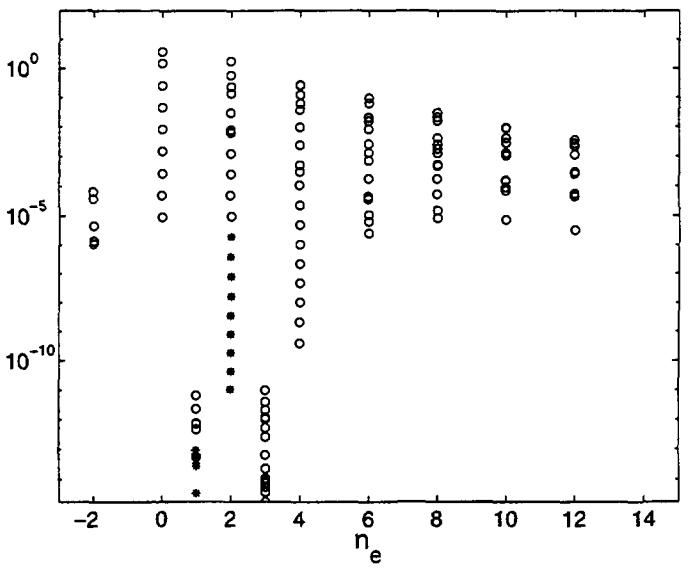

Figure 4.1: $\sqrt{g}_{m_e,n_e}$ *amplitudes for a* $L = 2$ *configuration with* $N_{per} = 5$. *The equilibrium is characterized by* $1/\epsilon_c = 5$, $\beta = 1\%$, *with pressure profile* pr^B *and* $J'(s)/J'_{norm} = 0.9(1 - s^{10})^2 - 0.4(1 - s^{2.5})^2$. *The x-axis corresponds to the* n_e *equilibrium mode number (rather than* $N_{per} n_e$*). The points marked with '*' represent the equilibrium components responsible for couplings between the* $(2,1)$ *mode and the* (m_l, n_l) *perturbation components with* $m_l > n_l > 1$ *(only the* $n_e \leq 2$ *i.e.* $n_l \leq 11$ *are shown). All other equilibrium components are identified with 'o'. See Tab.(B.1) for detailed informations.*

consists in the fact that the $\sqrt{g}_{m_e,n_e}$ amplitudes associated to odd n_e's are no longer negligible - see Fig.4.2. If $n_e = 1$, the perturbation components involved in couplings have $n_l = 3$ and 5; for example the $(6,5)$ component is coupled to $(2,1)$ via the $(m_e, n_e) = (4,1)$ equilibrium term whose amplitude is $\sqrt{g}_{4,1} \simeq 10^{-3}$ and the $(4,3)$ component is coupled to $(2,1)$ via $\sqrt{g}_{6,1} \simeq 10^{-4}$. Perturbation modes with $n_l = 7$,9 and $m_l/n_l > 1$ require $n_e = 2$ and appear for $m_e \geq 10$ and $m_e \geq 8$ respectively. The coupling with the $(10,9)$ component occurs via $\sqrt{g}_{8,2} \simeq 10^{-5}$; the couplings with the other $(m_l, 9)$, $m_l > 9$ or $(m_l, 11)$, $m_l > 11$ components (not visible in the table) involve $\sqrt{g}_{m_e,n_e}$ amplitudes which are less than 10^{-6}.

• **Tab.(B.3) and Fig.4.3**: study of the $(3,2)$ mode in a $L = 2$ configuration with $N_{per} = 5$. Here again the $\sqrt{g}_{m_e,n_e}$ amplitudes with $n_e = 1$ are extremly low $\simeq 10^{-13}$. The table shows only some of them involving couplings of $(3,2)$ with (m_l, n_l) components having $n_l = 3$, 7. If $n_e = 2$ then $n_l = 8$ and 12. The largest $\sqrt{g}_{m_e,n_e}$ amplitude related to couplings between $(3,2)$ and (m_l, n_l) with $m_l > n_l > 2$ is $\sqrt{g}_{10,2} \simeq -3.55 \cdot 10^{-6}$ involving the $(13,12)$ component. All other couplings with $(14,12)$, $(9,8)$, etc occur via $\sqrt{g}_{m_e,n_e} \leq 10^{-7}$.

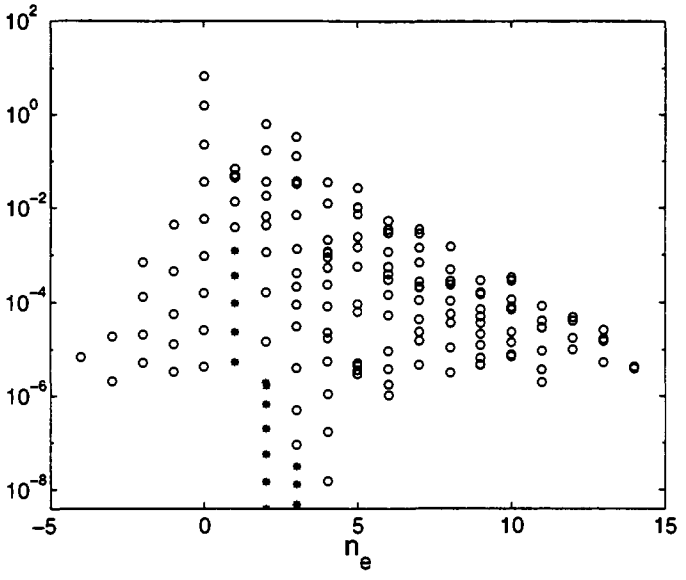

Figure 4.2: $\sqrt{g}_{m_e,n_e}$ *amplitudes for a mixed* $L = 2$ *and* $L = 3$ *configuration with* $N_{per} = 4$ *The is characterized by* $1/\epsilon_c = 5$, $\beta = 1\%$ *with pressure profile* pr^B *and* $J'(s)/J'_{norm} = 0.44(1 - s^{20})^8$. *The x-axis corresponds to the* n_e *equilibrium mode number (rather than* $N_{per}n_e$*). The points marked with '*' represent the equilibrium components responsible for couplings between the* $(2,1)$ *mode and the* (m_l, n_l) *perturbation components with* $m_l > n_l > 1$ *(only the* $n_e \leq 2$ *i.e.* $n_l \leq 9$ *are shown). All other equilibrium components are identified with 'o'.See Tab.(B.2) for detailed informations.*

In order to verify the generality of these remarks several tests have been performed. We kept constant the values of (m, n), L, N_{per} and β and observed the variation of the $\sqrt{g}_{m_e,n_e}$ amplitudes when doing the following:

- we estimated the $\sqrt{g}_{m_e,n_e}$'s on several flux surfaces. As the inner flux surfaces remain very similar to the boundary (in fact they are less deformed) the hierarchy of the $\sqrt{g}_{m_e,n_e}$ amplitudes remains practically the same.
- more visible changes appear when varying the amount of boundary deformation. Nevertheless, at weak or very strong δ's the $\sqrt{g}_{m_e,n_e}$ amplitudes involving couplings with (m_l, n_l), $m_l/n_l > 1$ remain considerably lower than the dominant terms.
- different current density profiles or pressure profiles do not bring noticable modifications in the $\sqrt{g}_{m_e,n_e}$ hierarchy.
- finally, if instead of the Jacobian we considered another equilibrium quantity also appearing in Eq.(2.43) i.e. $|B^2|$, we arrive at the same conclusions.

The validitity of the preceeding observations has been verified for any of the types of helical boundary deformation which were considered.

The discussion above can be summarized as follows:

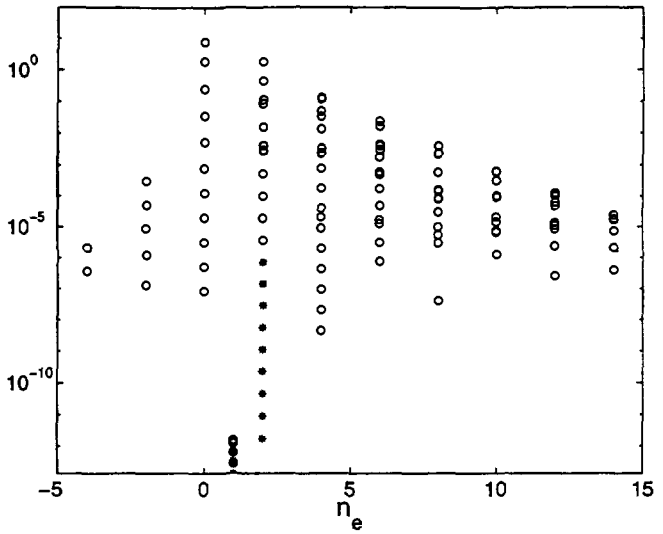

Figure 4.3: $\sqrt{g}_{m_e,n_e}$ *amplitudes for a* $L = 2$ *configuration with* $N_{per} = 5$. *The equilibrium is characterized by* $1/\epsilon_c = 5$, $\beta = 1\%$, *with pressure profile* pr^B *and* $J'(s)/J'_{norm} = 0.35(1 - s^{20})^8$. *The x-axis corresponds to the* n_e *equilibrium mode number (rather than* $N_{per}n_e$*). The points marked with '*' represent the equilibrium components responsible for couplings between the* $(3,2)$ *mode and the* (m_l, n_l) *perturbation components with* $m_l > n_l > 1$ *(only the* $n_e \leq 2$ *i.e.* $n_l \leq 11$ *are shown). All other equilibrium components are identified with 'o'.See Tab.(B.3) for detailed informations.*

• the equilibrium of plasmas with prescribed helical boundary deformation is characterized by a spectrum of $(m_e, N_{per}n_e)$ Fourier components (describing quantities related to the geometry or appearing in Eq.(2.43)) such that dominant components have low m_e and n_e values.

• the coupling between the $(m = n + 1, n)$ modes studied $n = 1, 2, 3$, with other (m_l, n_l) perturbation components having $m_l > n_l > n$ occurs via $(m_e, N_{per}n_e)$ equilibrium components with very low amplitude. Thus it is probable that the excitation of the (m_l, n_l) modes with resonant m_l/n_l values in the $1 < q < 2$ region will not influence the behaviour of the (m, n) mode studied. If the amplitude of the $(m_e, N_{per}n_e)$ equilibrium components serves as a scaling factor for measuring how strong the $(m, n) \times (m_l, n_l)$ couplings may be, then the most dangerous perturbation components have $m_l = n_l + 1$, followed by $m_l = n_l + 2$ etc. The values of n_l depend on N_{per} and L.

• the large value of the $(1, 0)$ equilibrium component has as consequence that strong couplings occur between (m_l, n_l) and $(m_l \pm 1, n_l)$ perturbation components. The largest equilibrium components (those which compared to the largest $(0, 0)$ term are from 10^0 to 10^{-3} times smaller) are responsible for couplings of modes studied only with perturbation components having $m_l/n_l < 1$ $(n_l > n)$ i.e. not having a rational surface for $q > 1$.

4.3 (m_l, n_l) perturbation modes with $m_l > n_l > n$

When we computed an equilibrium sequence corresponding to Eq.(4.1)) we chose the successive values of δ_i sufficiently close in order to obtain q profiles which decrease slowly from one equilibrium to the following. The study of an $(m = n + 1, n)$ mode is done by applying the following procedure :

A. taking advantage of the particularities of the $(m_e, N_{per} n_e)$ spectrum of modes described in the Section 4.2, we run TERPSICHORE for each $\mathcal{E}_i$ with the $\mathcal{T}_{m,n}^{nores}$ set. The successive lowest eigenvalues $\omega_{min}^{2\,nores}(\delta_i)$ are associated to one of the (m, n), $m = n, n+1, n+2$, etc modes (in general $m = n+1$). The reason for doing this comes from the fact that it is far more easy to follow the (m, n) mode when no (m_l, n_l) components with $m_l > n_l > n$ (resonances) are present. A chaining procedure combining equilibrium and stability calculations for the whole range of δ_i 's and aiming at determining the successive $\omega_{min}^{2\,nores}(\delta_i)$ can be easily designed.

In the case when some of the minimum eigenvalues thus obtained are positive then we have to verify that the re-inclusion of the (m_l, n_l) modes with $m_l > n_l > n$ does not bring important destabilizing couplings with (m, n). The following verification procedure is then applied:

B. Only those equilibria for which $\omega_{min}^{2\,nores}(\delta_i) > 0$ are considered and TERPSICHORE is run with the $\mathcal{T}_{m,n}$ set. Depending on the q profile, different (m_l, n_l) modes with $m_l > n_l > n$ can be destabilized. For each δ_i, we search in increasing order the hierarchy of the $\omega_j^2(\delta_i)$ negative eigenvalues $\omega_{min}^2(\delta_i) < \omega_1^2(\delta_i) < \omega_2^2(\delta_i) < .. < 0$ (as shown in Fig.C.1 from Appendix C) and identify the associated (m_j, n_j), $j = min$, 1, 2,.. dominant components. Then, for every ω_j^2, we evaluate the contribution of the $(m, n) \times (m_j, n_j)$ couplings together with the $(m, n) \times (m_l, n_l)$ couplings $(m_l > n_l > n)$ to the potential energy. If these contributions are negligible, then the elimination of the (m_l, n_l) modes with $m_l > n_l > n$ from $\mathcal{T}_{m,n}$ is justified.

The justification can be pursued in the following way. Here again we consider only those equilibria for which $\omega_{min}^{2\,nores}(\delta_i) > 0$.

C. The (m, n) mode is eliminated from the $\mathcal{T}_{m,n}$ set and TERPSICHORE is run to

evaluate the new $\tilde{\omega}^2_{min}(\delta_i) < \tilde{\omega}^2_1(\delta_i) < \tilde{\omega}^2_2(\delta_i) < .. < 0$ hierarchy. If the ratio

$$\frac{\tilde{\omega}^2_j(\delta_i) - \omega^2_j(\delta_i)}{\omega^2_j(\delta_i)} \simeq 0 \qquad \forall j, i \tag{4.3}$$

then the $(m,n) \times (m_l, n_l)$ couplings $(m_l > n_l > n)$ are really negligible and the (m,n) mode can be studied with the $\mathcal{T}^{nores}_{m,n}$ set.

4.4 Technical aspects

Without a chaining mechanism designed to automatize the computations, this work could not have been possible. Several hundreds of equilibrium sequences were calculated and their global MHD stability analysed by initiating a chaining procedure and waiting for the results. Details concerning these procedures are given in Appendix C.

The VMEC code was run with a number of radial mesh points N_s between 68 and 108 and the equilibrium quantities were decomposed in $N^v_e = 61$ Fourier pairs $(0 \leq m^v_e \leq 5, -5 \leq n^v_e \leq 5)$. The superscript ^{v} indicates that the decomposition is made in VMEC angular coordinates. Computing equilibria with a larger N^v_e number has no effect on the spectrum of Fourier equilibrium modes; this has been verified for all the types of boundary deformation considered.
For low currents at high β, we have found equilibria with large Shafranov shifts Δ_{Shf}. Even if the code converged well we did not continue the investigations when we encountered values exceeding $\Delta_{Shf} > 18 - 20\%$.
For the mapping of the equilibrium to Boozer coordinates we used a number N_e of Fourier modes varying from 120 to 200 - see Tab.(B.1) to Tab.(B.3) in the Appendix B. It has been shown in Section 4.2, that for $L = 2$ the equilibrium Fourier modes with odd n_e are extremely low; they play no role in the equilibrium reconstruction. Nevertheless we kept the $n_e = 1$ modes, especially those $(m_e, N_{per} n_e)$ pairs involving couplings with (m_l, n_l), $m_l/n_l > 1$ perturbation modes in order to check that the couplings are indeed unsignificant. The ballooning calculations were performed with values of $N_e \sim 400$ and more.
Several techniques are available to test the accuracy of the reconstructed equilibrium. The Jacobian $\sqrt{g_B}$ derived directly from the geometry can be compared with the quantity arising from the dot product of the co- and contravariant expressions of $\vec{B}$ (2.13).

$$\sqrt{g_B} B^2 = \Psi'(s) J(s) - \Phi'(s) I(s) \tag{4.4}$$

Another way is the comparison of the flux quantities $J'(s)$ and $I'(s)$ constructed from the equilibrium coordinates with the equivalent quantities obtained from the avearged radial

component of the force balance equation (2.15). These techniques were implemented in TERPSICHORE; the N_e set of modes was determined iteratively such that the relatives errors for the above mentioned quantities were inferior to 10^{-3}.

TERPSICHORE was run with $N_s = 68$ to 108 radial mesh points and 84 to 116 Fourier components for the perturbations. The number of vacuum grid points was generally $N_s/4$; For all simulations the position of the axisymmetric wall was kept fixed; the distance to the plasma boundary corresponded to two times the radius of the circular plasma boundary ($\delta = 0$). Convergence tests for N_s were done regularly to check the validity of the results.

Chapter 5

Results

5.1 Stability windows in δ

The circular tokamak $\delta = 0$ has a safety factor profile such that $q_{axis} < q_{edge}$. At $\delta = 0$, the typical values in our study are $1 < q_{axis} < 2.5$ and $1 < q_{edge} < 3.5$. The basic effect of increasing δ with all other equilibrium parametres remaining constant is to lower the inverse rotational transform. As the deformation of the flux surfaces is stronger near the plasma edge than near the magnetic axis, q_{edge} is lowered more rapidly than q_{axis}. This is true for $L = 2$, 3 configurations but not for $L = 1$ where q_{edge} and q_{axis} are decreased nearly at the same rate. For $L = 3$ configurations, q_{axis} barely changes.
At strong deformations, the q profile is inverted and the minimum of q is located either at the plasma edge or close to it.

TERPSICHORE is run with the $\mathcal{T}^{nores}_{m,n}$ set for an equilibrium sequence $\mathcal{E}_i$; if for a given δ_i, the q profile is such that the resonant value $q_{res} = m/n$ is in the vicinity of the plasma edge, the (m, n) mode is strongly destabilized. When δ is increased, the eigenvalue associated with the mode i.e. $\omega^2_{m,n}$ decreases and the mode in question rapidly has the strongest growth rate. At larger values of δ the eigenvalue reaches a minimum after which it starts increasing quickly. The (m, n) mode becomes less unstable and soon stabilizes. Depending on the equilibrium parameters, the stabilization can be more or less rapid; two situations may occur :
1) The stabilization is strong and a stability window $I^{stb}_{m,n} = [\delta_{min}, \delta_{max}]$ appears, in the sense that at δ_{max} the (m, n) mode is stable but the $(m-1, n)$ mode becomes unstable.
2) The stabilization is slow; when q has sufficiently decreased, the $(m-1, n)$ mode is destabilized and becomes the most unstable component of the perturbation such that ω^2_{min} starts decreasing again.
The first case is illustrated in Fig.5.1 to Fig.5.4 for different current density profiles, L types of boundary deformations and number of equilibrium field periods.

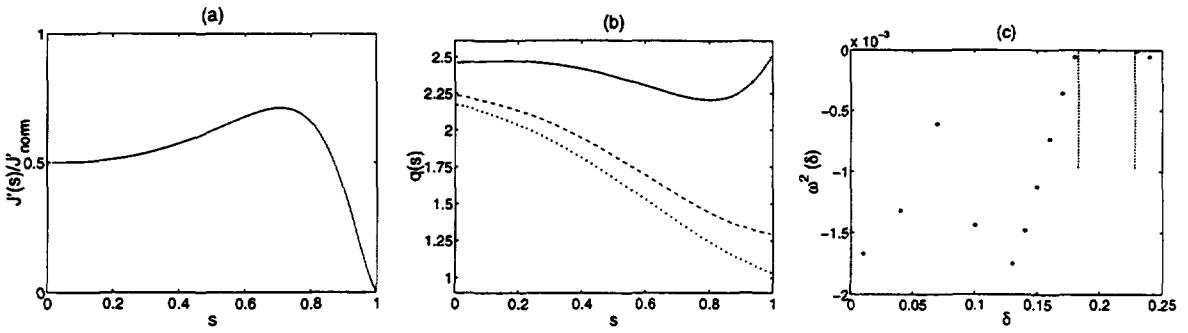

Figure 5.1: *Study of the (2,1) mode with the* $\mathcal{T}^{nores}_{m,n}$ *set:* (a) $J'(s)$ *profile,* (b) $q(s)$ *profile and* (c) *the most unstable eigenvalue* ω^2_{min} *as a function of* δ *for a configuration characterized by* $L = 2$, $N_{per} = 5$, $1/\epsilon_c = 5$, *at* $\beta = 1\%$, *with pressure profile* pr^B *and toroidal current density given by* $J'(s)/J'_{norm} = 0.9(1 - s^{10})^2 - 0.4(1 - s^{2.5})^2$. q *is represented for* $\delta_2 = 0.010$ *(-),* 0.180 *(- -) and* 0.230*(·). For* $\delta_2 = 0.010$ *and* 0.040 *the (3,1) component dominates, at* $\delta_2 = 0.070$ *the (3,1) and (2,1) components have comparable amplitudes, for* $0.100 \leq \delta_2 < 0.180$ *the (2,1) component is the strongest and finally for* $\delta_2 \geq 0.230$ *(last two points) the (1,1) components sets off. The stability window is delimited by the two vertical dotted lines.*

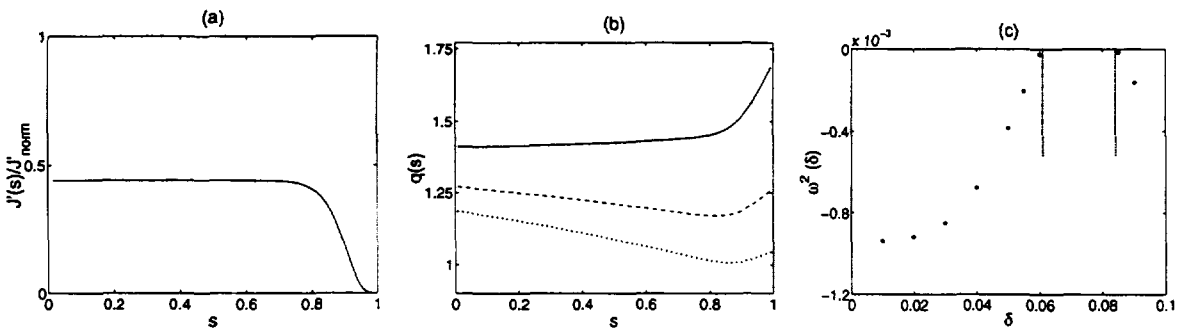

Figure 5.2: *Study of the (2,1) mode with the* $\mathcal{T}^{nores}_{2,1}$ *set:* (a) $J'(s)$ *profile,* (b) $q(s)$ *profile and* (c) $\omega^2_{min}(\delta)$ *for a mixed* $L = 2$ *and* $L = 3$ *configuration* ($\delta_3/\delta_2 = 2.5$), $N_{per} = 4$, $1/\epsilon_c = 10$, *at* $\beta = 1\%$, *with pressure profile* pr^B *and toroidal current density given by* $J'(s)/J'_{norm} = 0.44(1 - s^{20})^8$. q *is represented for* $\delta_2 = 0.010$ *(-),* 0.060 *(- -) and* 0.085*(·). The (2,1) component is dominant for* $\delta_2 \leq 0.07$ *and for* $\delta_2 \geq 0.085$ *the (1,1) component becomes destabilizing. The stability window is delimited by the two vertical dotted lines. See also Fig.5.6*

The second case is presented in Fig.5.5 for a $L = 3$ boundary deformation and $N_{per} = 4$. Fig.5.6 and Fig.5.7 show the evolution of the largest Fourier components of ξ and η between three values of δ corresponding to the beginning of the equilibrium sequence (δ_{start}), the beginning and the end of the stability window.

Fig.5.6 illustrates the same case as in Fig.5.2. At $\delta_3 = 0.010$, $\xi_{(2,1)}$ has the largest ampli-

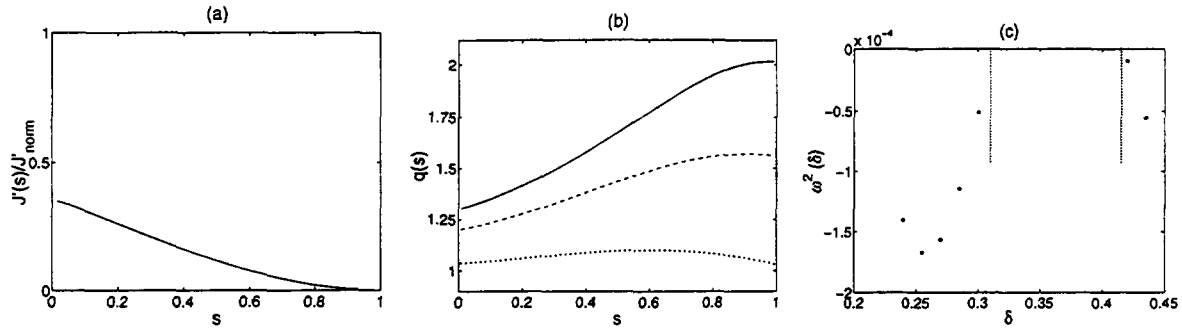

Figure 5.3: *Study of the (2,1) mode with the* $\mathcal{T}_{2,1}^{nores}$ *set:* **(a)** $J'(s)$ *profile,* **(b)** $q(s)$ *profile,* **(c)** $\omega^2_{min}(\delta)$ *for* $L = 2$, $N_{per} = 4$, $1/\epsilon_c = 10$, *at* $\beta = 1\%$ *with* pr^A *pressure profile and* $J'(s)/J'_{norm} = 0.35(1 - s^{1.2})^2$. q *is plotted for* $\delta_2 = 0.240$ *(-),* 0.300 *(- -) and* 0.420*(·). There is no equilibrium for* $\delta_2 = 0$. *For the first five points* ($0.240 \leq \delta_2 \leq 0.300$) *the (2,1) component has the largest amplitude, for the last two* ($\delta_2 \geq 0.420$), *the (1,1) component dominates.*

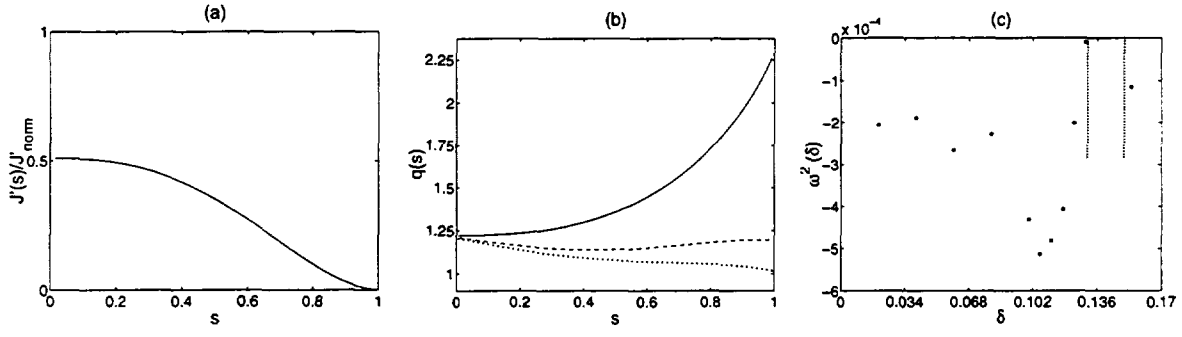

Figure 5.4: *Study of the (3,2) mode with the* $\mathcal{T}_{3,2}^{nores}$ *set:* **(a)** $J'(s)$ *profile,* **(b)** $q(s)$ *profile,* **(c)** $\omega^2_{min}(\delta)$ *for* $L = 3, N_{per} = 4, 1/\epsilon_c = 10$, $\beta = 1\%$, *pressure profile* pr^A *and toroidal current density given by* $J'(s)/J'_{norm} = 0.51(1 - s^{2.5})^2$. q *is represented for* $\delta = 0.020$, $\delta = 0.130$ *and* $\delta = 0.154$. *The (5,2) component dominates for* δ*=0.020 and 0.040, at* δ*= 0.060* (q_{edge}*=1.915) the (4,2) is the strongest, and for* $0.080 \leq \delta \leq 0.130$ *the (3,2) component has the largest amplitude. The stable window is between* $0.130 < \delta_3 < 0.154$ *and for* $\delta_3 \geq 0.154$ *the (2,2) component is destabilizing. See also Fig.5.7*

tude followed by $\xi_{(3,1)}$ and $\xi_{(4,1)}$; $\xi_{(1,1)}$ comes only in the fourth position but is the second most important at $\delta_3 = 0.060$ and becomes the dominant at $\delta_3 = 0.085$. For this last value of δ_3, Fig.5.2 shows a q_{min} slightly less than unity and we see from Fig.5.6 that the $(1,1)$, $(3,3)$ and $(5,5)$ perturbation components are excited. In the case presented in Fig.5.7 the mode studied was $(3,2)$. At $\delta_3 = 0.020$ the q profile is such that $\xi_{(5,2)}$ and $\eta_{(5,2)}$ respectively, have the largest amplitudes. At $\delta_3 = 0.130$ the $(3,2)$ component is dominant and at $\delta_3 = 0.154$ ($q_{edge} \simeq 1$) the $(2,2)$ component becomes the largest, followed by $(6,6)$. Complementary information is given in Fig.5.4.

If TERPSICHORE is run with the $\mathcal{T}_{m,n}$ set, several (m_l, n_l) modes with $m_l > n_l > n$ can be destabilized in the $[\delta_{min}, \delta_{max}]$ interval. We want to verify that the (m,n) modes

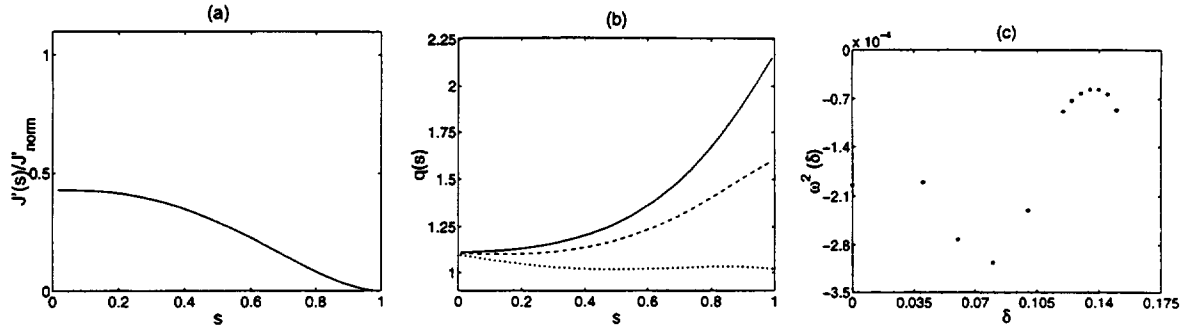

Figure 5.5: *Study of the (2,1) mode with the* $\mathcal{T}_{2,1}^{nores}$ *set:* (**a**) $J'(s)$ *profile,* (**b**) $q(s)$ *profile and* (**c**) $\omega^2_{min}(\delta)$ *for a configuration characterized by* $L = 3$, $N_{per} = 4$, $1/\epsilon_c = 13$, *at* $\beta = 1\%$, *with pressure profile* pr^A *and toroidal current density given by* $J'(s)/J'_{norm} = 0.43(1 - s^{2.5})^2$. q *is represented for* $\delta_2 = 0.$ *(-),* 0.080 *(- -) and* 0.140*(·). At* $\delta_3 = 0.$ *the* $(3,1)$ *component dominates, the* $(2,1)$ *mode is destabilized for* $\delta_3 > 0.06$ *then becomes less unstable after* $\delta_3 > 0.08$. *Beginning with* $\delta_3 \sim 0.13$ *the (1,1) mode is excited. At* $\delta_3 = 0.14$, *the minimum of the inverse rotational transform* q_{min} *becomes smaller than 1. There is no stability window.*

$(m = n, n+1, n+2, ..)$ modes remain stable in the $I^{stb}_{m,n}$ interval when allowing the $(m,n) \times (m_l, n_l)$ couplings $(m_l > n_l > n)$. For this purpose we apply the verification procedure described in Section 4.3. The fact that we may then obtain a series of negative eigenvalues $\omega^2_{min}(\delta_i) < \omega^2_1(\delta_i) < \omega^2_2(\delta_i) < .. < 0$ is not a definite proof that all associated (m_l, n_l) modes are unstable for the $\delta_i \in I^{stb}_{m,n}$ selected. If valid results for a particular (m_l, n_l) mode are desired, then TERPSICHORE should be run with the appropiate $\mathcal{T}_{m_l,n_l}$ set.

The existence of the stability window for δ motivates the stability analysis. The aim of the investigation work is to describe the properties of this stability window and to find how it is affected by the equilibrium parameters.

5.2 Role of the $(m,n) \times (m_l, n_l)$, $m_l > n_l > n$ couplings

In this section we present the results obtained when applying the verification procedure as described in Section 4.3. Two cases are considered; for both of them, the mode studied is $(m,n) = (2,1)$. The equilibria correspond to three different values of the boundary deformation parameter; these values belong to the stability window $\delta \in I^{stb}_{m,n}$.

A) a configuration with $L = 2$, $N_{per} = 5$ at $\beta = 1\%$. The current density profile is $J'(s)/J'_{norm} = -0.9(1 - s^{10})^2 + 0.4(1 - s^{2.5})^2$ and the pressure profile is pr^B Eq.(3.10). It

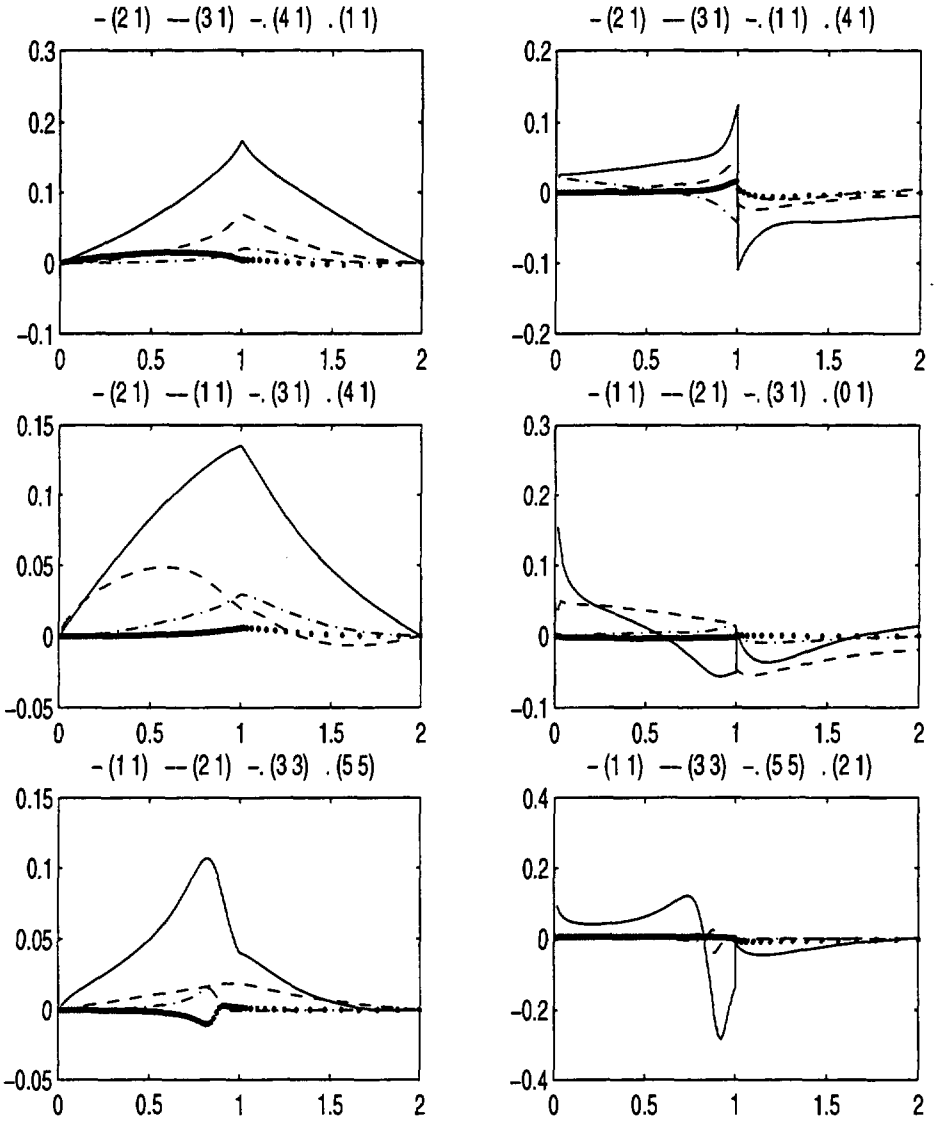

Figure 5.6: *The four most important perturbation components $\xi_{m,n}(s)$ (left column) and $\eta_{m,n}(s)$ (right column) for the same case as in Fig.5.2 i.e. a mixed $L = 2$ and $L = 3$, $N_{per} = 4$, $1/\epsilon_c = 10$, pr^B, $\beta = 1\%$, $J'(s)/J'_{norm} = 0.44(1 - s^{20})^8$ at $\delta_3 = 0.010$ (first row), 0.060 (middle row, just before the stability window) and 0.085 (last row, just after the stability window). For each of these values $\delta_2 = 2.5\,\delta_3$. The interval $0 \leq s \leq 1$ corresponds to the plasma region and $1 \leq s \leq 2$ to the vacuum region. The (m, n) perturbation components are listed from left to right in the order of decreasing maximum amplitude.*

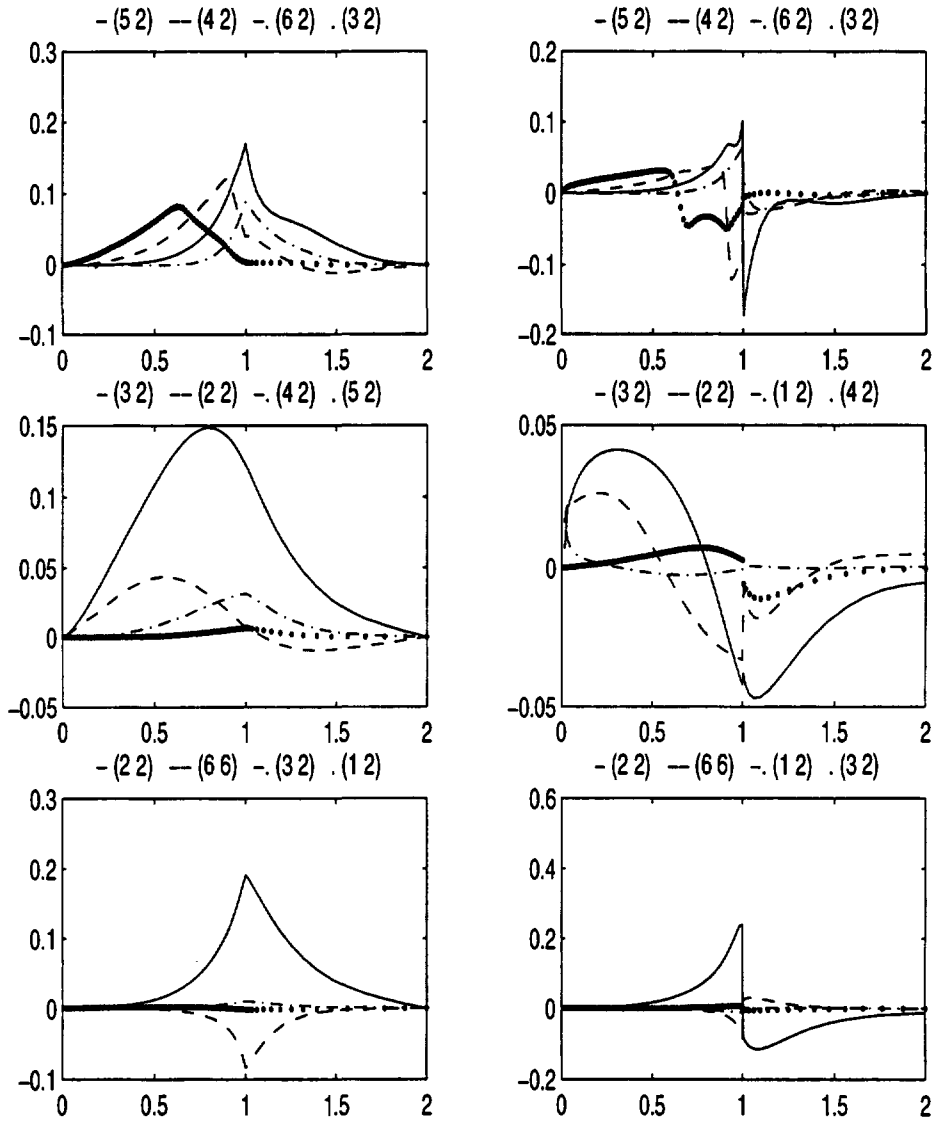

Figure 5.7: *The four most important perturbation components* $\xi_{m,n}(s)$ *(left column) and* $\eta_{m,n}(s)$ *(right column) for the same case as in Fig.5.4 i.e.* $L = 3$, $N_{per} = 4$, $1/\epsilon_c = 10$, pr^B, $\beta = 1\%$, $J'(s)/J'_{norm} = 0.51(1 - s^{2.5})^2$ *at* $\delta_3 = 0.020$ *(first row), 0.130 (middle row, just before the stability window) and 0.154 (last row, just after the stability window). The interval* $0 \leq s \leq 1$ *corresponds to the plasma region and* $1 \leq s \leq 2$ *to the vacuum region. The* (m, n) *perturbation components are listed from left to right in the order of decreasing maximum amplitude.*

is the same equilibrium sequence as that shown in Fig.5.1. The stability window is inside the interval $0.180 < \delta_2 < 0.230$. The data has been represented separately in two tables:
• Tab.(5.1) shows the hierarchy of eigenvalues and the associated unstable modes. The corresponding values of q_{axis}, q_{min} and q_{edge} are indicated. For example at $\delta_2 = 0.190$ there are four unstable modes (the fifth eigenvalue searched in increasing order is positive); the $(11,9)$ mode has the strongest growth rate $\omega^2_{min} = -5.928 \times 10^{-4}$ and the $(8,6)$ mode is the least unstable $\omega^2_{8,6} = -3.026 \times 10^{-5}$. Let $W_p^{(m_{l1},n_{l1})\times(m_{l2},n_{l2})}$ be the contribution to the potential energy of the coupling between perturbation components (m_{l1}, n_{l1}) and (m_{l2}, n_{l2}).The last column represents the quantity

$$W_p^{max\ res} = max\{\ max_k|W_p^{(2,1)\times(m_k,n_k)}|,\ max_{k'}|W_p^{(1,1)\times(m_{k'},n_{k'})}|\ \} \tag{5.1}$$

where (m_k, n_k), $(m_{k'}, n_{k'})$ are perturbation components with resonant values for $q > 1$. $W_p^{max\ res}$ has to be compared with

$$W_p^{max} = max_{l1,l2}|W_p^{(m_{l1},n_{l1})\times(m_{l2},n_{l2})}| \tag{5.2}$$

where (m_{l1}, n_{l1}) and (m_{l2}, n_{l2}) may be any perturbation components (including resonant and non resonant ones for $q > 1$). One can observe that $W_p^{max\ res} << W_p^{max}$.
• Tab.(D.1) in Appendix D gives more details concerning the perturbation components that contribute to the couplings and the corresponding $W_p^{(m_{l1},n_{l1})\times(m_{l2},n_{l2})}$ values. Each set of four lines is associated in corresponding order to one unstable eigenvalue from Tab.(5.1). The first line of any set shows the four main contributions. The following three lines show amplitudes of $(2,1) \times (m_l, n_l)$ couplings such that either (m_l, n_l) is the dominant perturbation component or the $(m_e, N_{per}n_e)$ equilibrium component involved in the coupling is among the three largest in the hierarchy of equilibrium terms (not the whole hierarchy but that part involving couplings with (m_l, n_l) components such that $m_l > n_l > n$). We have also shown the $(1,1) \times (m_l, n_l)$ couplings because (n,n) modes are, in general, responsible for the upper boundary of the stability window; the values of q are such that the mode is susceptible to become excited.
For $\delta_2 = 0.190$ the main contribution i.e. $\sim -3.89 \times 10^{-4}$ comes from the $(11,9) \times (11,9)$ term ; the second is due to the $(11,9) \times (12,9)$ coupling via the $(1,0)$ equilibrium term and is about half less i.e. $\sim -1.94 \times 10^{-4}$. The third main contribution i.e. $\sim -1.06e \times 10^{-4}$ comes from the $(9,-1) \times (11,9)$ coupling involving the $(m_e, n_e) = (2,2)$ $(N_{per} = 5)$ equilibrium term which, as we see from Tab.(B.1), is one of the most important $(\sqrt{g}_{2,2} \simeq -1.7 \times 10^0)$. We also see that the $(2,1) \times (11,9)$, $(2,1) \times (10,9)$, $(1,1) \times (11,9)$, .. couplings are largely inferior to the $(11,9) \times (11,9)$ contribution. The same is true for the couplings with other components $(5,4)$, $(6,4)$, $(10,9)$, etc. Therefore it is justified to

have used the $\mathcal{T}_{2,1}^{nores}$ set.

B) a configuration with a mixed $L = 2$ and $L = 3$ boundary deformation ($\delta_3/\delta_2 = 2.5$), $N_{per} = 4$ at $\beta = 1\%$. The current density profile is broad $J'(s)/J'_{norm} = 0.44(1 - s^{20})^8$ i.e. nearly constant in the main part of the plasma and falling rapidly to zero near the edge. The pressure profile is pr^B (Eq.(3.10)). The equilibrium sequence corresponds to that illustrated in Fig.5.2 with the stability window being inside the interval $0.060 < \delta_2 < 0.085$. The two associated data tables are:

• Tab.(5.2) indicating five unstable eigenvalues for $\delta_2 = 0.065$ and 0.070 and only two for $\delta_2 = 0.080$. Here $q_{min} \neq q_{edge}$. The relation $W_p^{max\,res} << W_p^{max}$ continues to be valid.

• Tab.(D.2) shows the couplings contributions. For $\delta_2 = 0.065$ (i.e. $\delta_3 = 0.162$) the main contribution $\sim -4.94 \times 10^{-4}$ comes from the $(4,3) \times (5,3)$ coupling followed by the $(5,3) \times (5,3)$ term. The ratio of the $(2,1) \times (m_l, 3)$ couplings to the dominant contribution is $\sim 10^{-6}$. This ratio climbs to $\sim 10^{-4}$ if we consider the $(1,1) \times (m_l, 3)$ couplings; in this last case the equilibrium coupling term is $(m_e, n_e) = (5,1)$ ($N_{per} = 4$) with an amplitude $\sqrt{g}_{5,1} \simeq -1.2 \times 10^{-3}$ which is the second largest among the equilibrium components responsible for couplings with (m_l, n_l) components satisfying $m_l > n_l > 1$ (see Tab.(B.2)). Even if the couplings are considerably stronger than in the pure $L = 2$ case, they still remain very low (compared to the dominant terms) to have an influence on the potential energy.

5.3 Stability areas and equilibrium parameters

Having found an interval for δ in which the (m,n), $m = n, n+1, n+2, ..$ modes are stable, we want to know what happens if the plasma current is slightly modified. We vary then the a_1 parameter from Eq.(3.8) and keep $a_2..a_6$ constant. By doing this we increase or decrease $J'(s)$ but do not affect its shape. Other stability windows may thus be obtained; the representation of these stability windows in a (q_{axis}, q_{edge}) plane gives a stability area denoted by SA - see Fig.5.8 to Fig.5.11.

In these plots, each vertical line (for $L = 3$) or oblique line (for $L = 2$) represents an equilibria sequence associated to one value of a_1; large a_1's correspond to equilibrium having smaller q_{axis}. An equilibrium sequence starts from a $(q_{axis}(\delta_{start}), q_{edge}(\delta_{start}))$ point situated at top of the plane, and ends at the bottom, in the $q_{edge} \simeq 1$ region. As mentioned in Sect. 5.1, the q profile is never lowered at the same rate throughout the whole plasma when increasing δ. The slope defined by $\Delta q_{edge}/\Delta q_{axis}$ when $i \rightarrow i+1$ can vary with δ_i and from one equilibrium sequence to another, but is in most of the cases larger than 45°

δ	q_{axis}	q_{min}	q_{edge}	ω^2	$(m_l, n_l)_\xi$		$(m_l, n_l)_\eta$		W_p^{max}	$W_p^{max\ res}$
0.190	2.223	1.233	1.233	-5.928E-04	11	9	11	9	-3.89E-04	-6.37E-15
				-5.513E-04	14	11	14	11	-2.43E-04	2.78E-16
				-1.715E-04	5	4	5	4	-1.07E-04	-1.04E-15
				-3.026E-05	8	6	8	6	-8.43E-05	-6.19E-17
0.200	2.210	1.178	1.178	-3.391E-04	7	6	7	6	-2.76E-04	-7.98E-17
				-2.671E-04	11	9	11	9	-1.30E-04	-1.30E-13
				-5.363E-05	13	11	13	11	-5.73E-05	-2.12E-15
				-4.594E-05	5	4	5	4	-3.52E-05	-4.94E-15
0.220	2.185	1.076	1.076	-2.115E-04	12	11	12	11	-1.70E-04	-9.02E-15
				-6.188E-05	10	9	10	9	-4.42E-05	-3.49E-14

Table 5.1: *The unstable eigenvalues obtained when studying the* $(2,1)$ *mode with the* $\mathcal{T}_{2,1}$ *set. The equilibria are from the same sequence as those in Fig.5.1 i.e.* $L = 2$, $N_{per} = 5$, $1/\epsilon_c = 5$, pr^B *and* $J'(s)/J'_{norm} = 0.9(1-s^{10})^2 - 0.4(1-s^{2.5})^2$. *The three values of* δ *are inside the stability window i.e. the* $(n,1)$ *modes are stable if studied with the* $\mathcal{T}_{m,n}^{nores}$ *set. The perturbation components with the largest* ξ_{max} *and* η_{max} *amplitudes are given in the columns at the right of* ω^2. *The quantities* W_p^{max} *and* $W_p^{max\ res}$ *were defined by Eq.(5.1) and the lines following.*

δ	q_{axis}	q_{min}	q_{edge}	ω^2	$(m_l, n_l)_{\xi_{max}}$		$(m_l, n_l)_{\eta_{max}}$		W_p^{max}	$W_p^{max\ res}$
0.065	1.254	1.137	1.218	-4.398E-04	4	3	4	3	-4.94E-04	-1.54E-08
				-2.119E-04	6	5	6	5	-4.23E-04	-2.68E-08
				-1.818E-04	8	7	8	7	-3.36E-04	-5.39E-14
				-6.918E-05	11	9	11	9	-2.63E-04	-4.66E-12
				-8.521E-06	8	7	8	7	-1.51E-05	6.36E-15
0.070	1.237	1.104	1.172	-4.318E-04	6	5	6	5	-4.28E-04	-5.80E-08
				-2.029E-04	4	3	4	3	-4.69E-04	-3.63E-10
				-1.973E-04	10	9	10	9	-3.03E-04	-2.59E-12
				-1.750E-04	8	7	8	7	-3.38E-04	-1.59E-11
				-2.821E-05	10	9	10	9	-4.63E-05	-4.25E-13
0.080	1.203	1.039	1.087	-1.880E-04	10	9	10	9	-3.57E-04	-9.95E-12
				-2.264E-05	8	7	8	7	-3.35E-04	-5.37E-13

Table 5.2: *The unstable eigenvalues obtained when studying the* $(2,1)$ *mode with the* $\mathcal{T}_{2,1}$ *set. The equilibria are from the same sequence as those in Fig.5.2 i.e. a mixed* $L = 2$ *and* $L = 3$ *boundary deformation,* $N_{per} = 4$, $1/\epsilon_c = 10$, pr^B *and* $J'(s)/J'_{norm} = 0.44(1-s^{20})^8$. *The three values of* δ *are inside the stability window i.e. the* $(n,1)$ *modes are stable if studied with the* $\mathcal{T}_{m,n}^{nores}$ *set. The columns at the right of* ω^2 *show the perturbation components with the largest* ξ_{max} *and* η_{max} *amplitudes;* W_p^{max} *and* $W_p^{max\ res}$ *were defined by Eq.(5.1) and the lines that follow.*

indicating that q_{edge} diminishes generally more rapidly than q_{axis}.

The stability areas can be described in terms of size, shape and position in the $\{q_{axis}, q_{edge}\}$ plane. The comparison of these attributes between several SA's, was chosen to serve as a basis for discussing the effects of the different equilibrium parameters on the stabilization process. All numerical values that follow are related to the $(2,1)$ mode. The results concerning other (m,n) will be mentioned later.

• SA position and limits

The largest part of the SA is situated in most cases under the diagonal $q_{edge} = q_{axis}$ and in the region limited by $q_{edge} \leq 1.5$. The windows of stability correspond generally to inverted q profiles. In a number of cases q_{edge} is lowered so much that $q_{min} = q_{edge}$ and the inverse rotational transform becomes a monotonically decreasing function of s. This is generally true for hollow and to some extension for broad current density profiles - see Fig.5.1.

The upper margin of the SA represents the entry points in the stability windows i.e. the δ_{min} correspondig to the selected a_1's. Its left (small q_{axis}) and lower (small q_{edge}) margins correspond to the destabilization of an (n,n) mode. In general these limits are associated with $q_{min} \simeq 1.0$. The nature of the SA boundary at large q_{axis} cannot be clearly defined and will be discussed below.

• dependence on the current profiles

Small currents require more deformation for stabilization (bigger δ_{min}) than larger currents. This is because a smaller current implies higher values of q at δ_{start} ; when q is lowered the values of δ for which the mode studied is destabilized (before being stabilized) are higher than in the large current case.

Peaked current density profiles ($a_2 < 1.5$) yield compact stability areas, situated mostly in the $1.0 < q_{axis} < 1.5$ region - see Fig.5.8(a), Fig.5.9(a) and Fig.5.11. Broad current densities ($a_2 > 5$) give areas elongated in the q_{axis} direction - see Fig.5.8(b) and Fig.5.9(b). Hollow currents ($sign(a_1) \neq sign(a_4)$) produce stable areas shifted towards large q_{axis} Fig.5.8(c) and Fig.5.9(c). For strong and peaked currents densities, stabilization occurs also when $q_{axis} < q_{edge}$ and/or non monotonic q profiles - see Fig.5.3 and Fig.5.8(a), Fig.5.9(a), Fig.5.11.

• number of field periods and and aspect ratio

Calculations realized with several current density profiles and at different aspect ratios have shown that $N_{per} = 4$ and $N_{per} = 5$ give stability areas which are comparable in size. We can give only a qualitative appreciation by saying that the differences are at the level

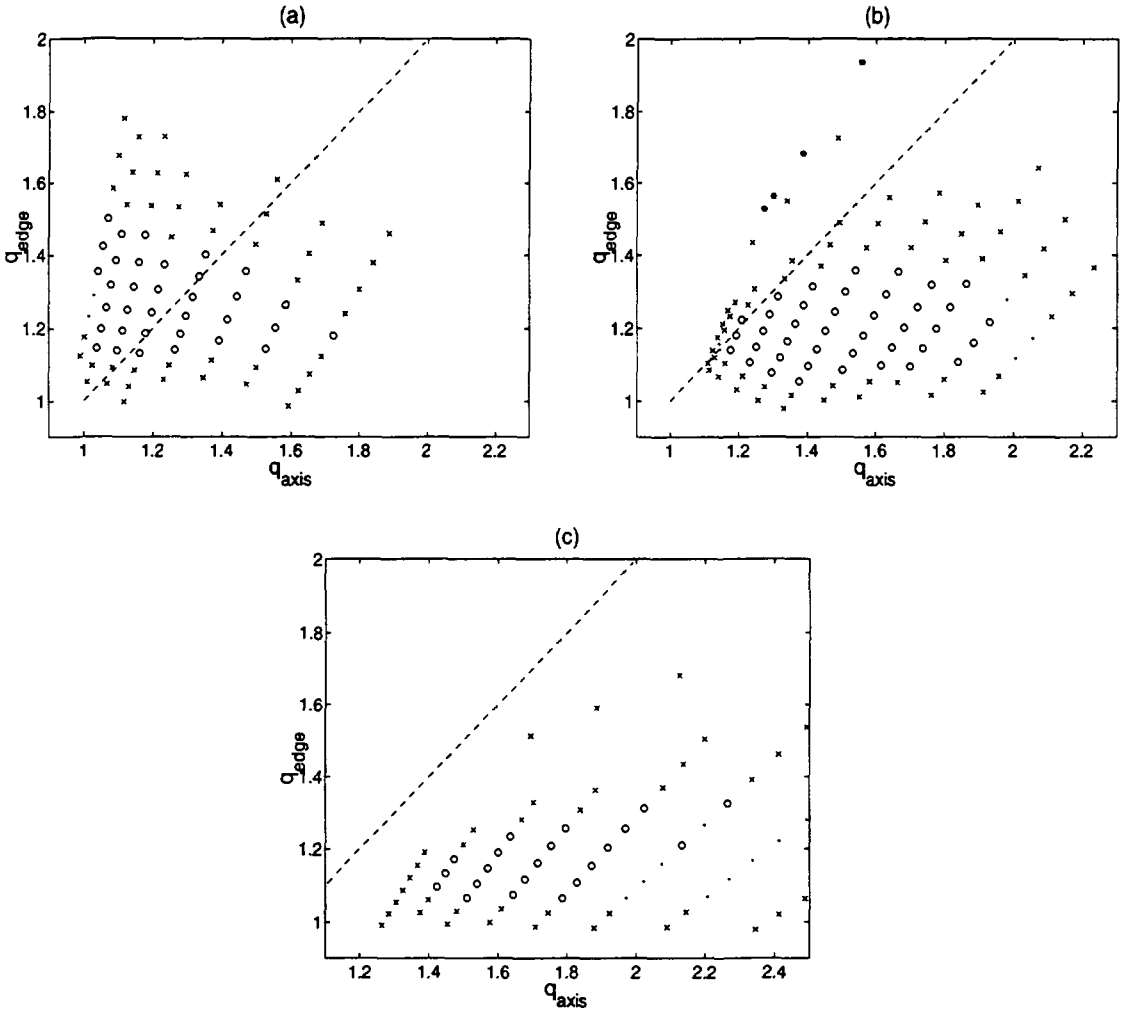

Figure 5.8: *Stability area of the* $(2,1)$ *mode* ($\mathcal{T}_{2,1}^{nores}$ *set) for equilibria with* $L = 2$, $N_{per} = 5$, $1/\epsilon_c = 10$, *at* $\beta = 1\%$ *and pressure profile* pr^B. *The difference between the three plots is due to the current density profile.* **(a)** *peaked profile* $J'(s)/J'_{norm} = a_1(1 - s^{1.2})^2$, **(b)** *broad profile* $J'(s)/J'_{norm} = a_1(1 - s^{20})^8$, **(c)** *hollow profile* $J'(s)/J'_{norm} = a_1(1 - s^{10})^2 - 0.4(1 - s^{2.5})^2$. *Each oblique line corresponds to a fixed* a_1 *value and represent* (q_{axis}, q_{edge}) *pairs at different* δ*'s. Unstable points are represented with the labels "*$\times$*", stable points with "*$\circ$*" and points close to marginal stability with "*$\cdot$*". The circular tokamak* $\delta_2 = 0$ *is represented by "*$*$*". Peaked currents can give stable equilibria with* $q_{axis} < q_{edge}$. *The stable areas associated with hollow currents start at higher* q_{axis}.

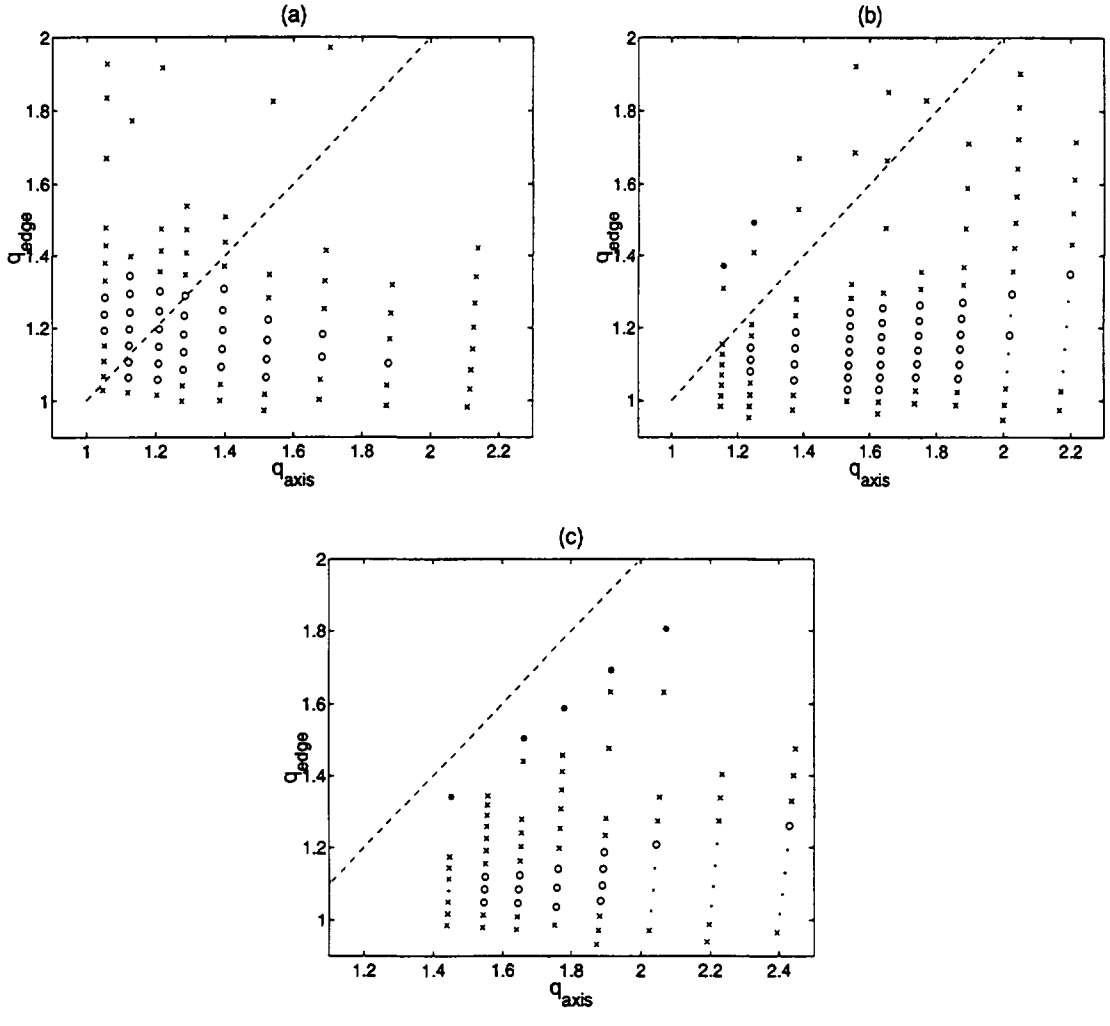

Figure 5.9: *Stability area of the* $(2,1)$ *mode (*$\mathcal{T}_{2,1}^{nores}$ *set) for equilibria with* $L = 3$, $N_{per} = 4$, $1/\epsilon_c = 10$, *at* $\beta = 1\%$ *and pressure profile* pr^B. **(a)** *peaked profile* $J'(s)/J'_{norm} = a_1(1-s^{2.5})^2$, **(b)** *broad profile* $J'(s)/J'_{norm} = a_1(1-s^{20})^8$, **(c)** *hollow profile* $J'(s)/J'_{norm} = a_1(1-s^{10})^2 - 0.4(1-s^{2.5})^2$. *Each vertical line corresponds to a fixed* a_1 *value and represent* (q_{axis}, q_{edge}) *pairs at different* δ*'s. Unstable points are represented with the labels "*$\times$*", stable points with "*o*" and points close to marginal stability with "*.*". The circular tokamak* $\delta_2 = 0$ *is represented by "*$*$*".*

of details. This is no longer true when $N_{per} = 7$; the associated SA seems to be reduced in size by a factor of two or more - see Fig.5.10 (a). Unfortunately we do not have enough data to sustain a detailed comparison and no study was done for higher N_{per} to verify if the stabilization becomes indeed less effective.

Regarding the inverse aspect ratio the following cases have to be distinguished :

a) $L = 3$ boundary deformation - the average plasma radius does not change with δ and the inverse aspect ratio remains constant when increasing the plasma boundary deformation. The largest SA were produced with $1/\epsilon \simeq 8$ to 10. For $1/\epsilon_c = 13$ the SA seem to decrease but the differences with the former two values were small - see Fig.5.10 (b). For $1/\epsilon_c = 5$, the reconstruction of the equilibrium in Boozer coordinates is systematically subject to errors (c.f. Section 4.4 and Eq.(4.4)) and we decided to eliminate the results from the discussion.

b) $L = 2$ boundary deformation - the calculation of the average plasma radius from Eq.(3.1) gives an inverse aspect ratio which varies with δ according to the law

$$\frac{1}{\epsilon} = \frac{1}{\sqrt{1+\delta}} \frac{1}{\epsilon_c} \tag{5.3}$$

If for example, the equilibrium sequence is started with $1/\epsilon_c = 10$ at $\beta = 1\%$, then in the stability windows, $1/\epsilon$ may reach values between 9 and 8.5 (δ_2 betwen 0.2 and 0.4). The latter value corresponds to the cases with small and peaked current densities. As $1/\epsilon$ changes slowly but continually, we chose $1/\epsilon_c$ as a comparison criterion. We arrived at the same conclusions as those from point a). Concerning $1/\epsilon_c = 5$, the stability areas were less extended compared with $1/\epsilon_c = 8$ or 10. For $1/\epsilon_c = 17$ the Shafranov shifts became very high $\Delta_{Shf} \sim 20\%$ and the stability calculations may be compromised by questionable equilibria; therefore we do not comment them.

c) mixed $L = 2$ and $L = 3$ boundary deformation - the variation of $1/\epsilon$ is due only to δ_2 and the comments from point b) remain valid.

• type of boundary deformation

$L = 2$ configurations require for stabilization values of δ which are much larger than those for $L = 3$ configurations i.e $\delta_{min}^{L=2} \sim 0.20 - 0.30$ compared to $\delta_{min}^{L=3} \sim 0.08 - 0.12$ - see Fig.5.1, Fig.5.3 and Fig.5.4. Fig.5.8 illustrates stability areas obtained with three different current profiles for a $L = 2$ configuration at $\beta = 1\%$ and $1/\epsilon_c = 10$; the same is shown in Fig.5.9 for a $L = 3$ configuration.

If we ignore for the moment the right side of the (q_{axis}, q_{edge}) plane and compare only the $q_{axis} < 2$ regions, we observe that the $L = 2$ configurations give stability areas which are slightly larger than those produced by $L = 3$ configurations. For $L = 2$, stable equilibria can exist with a higher q_{edge} (1.4 for example) than in the $L = 3$ case. We admit that a comparison between the two sets of figures (Fig.5.8 and Fig.5.9) is not quite justified here

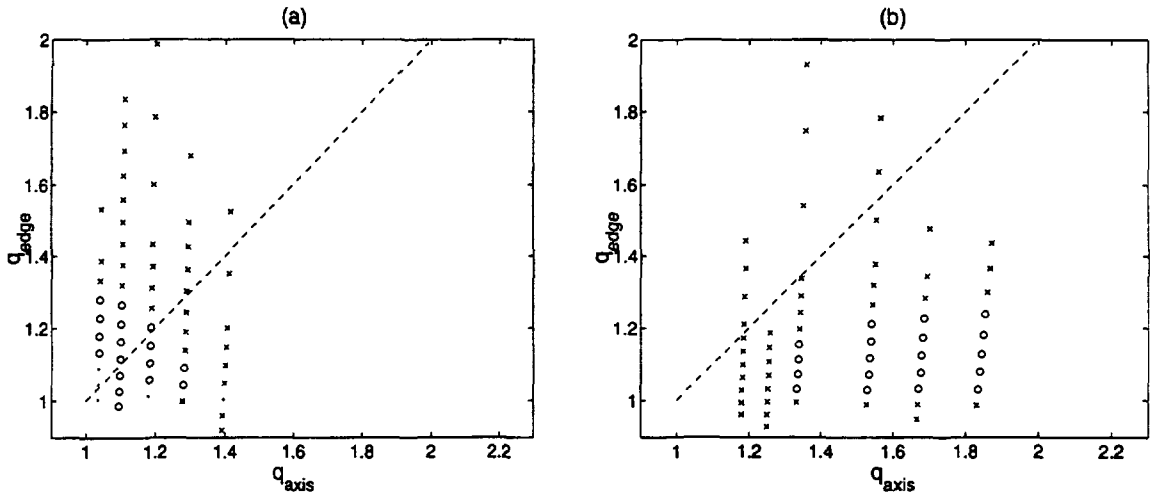

Figure 5.10: *Stability area of the* $(2,1)$ *mode studied with the* $\mathcal{T}_{2,1}^{nores}$ *set*
(a): $L = 3$ *configuration,* $N_{per} = 7$, $1/\epsilon_c = 14$, $\beta = 1\%$, $pr^B\ J'(s)/J'_{norm} = a_1(1 - s^{1.2})^2$
(b): $L = 3$ *configuration,* $N_{per} = 5$, $1/\epsilon_c = 13$, $\beta = 1\%$, $pr^B\ J'(s)/J'_{norm} = a_1(1 - s^{20})^8$

because the number of field periods are different and also because in Fig.5.8 the inverse aspect ratio varies according to Eq.(5.3). However, the previous statements were checked in numerous other cases with stability areas calculated with the same N_{per}.

Mixed configurations have been investigated by applying a simultaneous $L = 2$ and $L = 3$ boundary deformation such as to keep a constant $r = \delta_2/\delta_3$ ratio. Three values have been considered $r = 2.0$, 2.5, 3.0. Let δ^{aver} be the value obtained when one roughly estimates the average over many equilibrium sequences (for fixed current density profile) of the middle of the stability windows. The ratio $\delta_2^{aver}/\delta_3^{aver}$ estimated for different $J'(s)$ profiles is in the range 2.5 - 3.

The mixed configurations were tested only for $1/\epsilon_c = 10$, $N_{per} = 5$ and with peaked, broad and hollow current profiles. Comparing with the pure $L = 2$, we did not observe any significant enlargement of the SA. We can only say that for peaked current profiles the SA obtained with $r = 2.5$ and 3.0 were slightly larger than the SA resulting from $r = 2.0$. Fig.5.11 illustrates this difference in the case of a peaked current profile.

We have tested only a limited number of cases for $L = 1$ configurations and found no stability windows (at $\beta = 1\%$). These are however special cases in the sense that:

1) the plasma boundary is not really deformed; instead, the whole circular cross-section rotates around the axis defined by $R = R_0$

2) the q profile is lowered in a much more uniform way; q_{axis} decreases nearly at the same rate as q_{edge} and the $q = 1$ limit is quickly reached. For all cases tested, the q profiles never get inverted because the $q_{axis} < 1$ limit was reached before q_{edge} could be lower than q_{axis}. Fig.5.12 shows taht the (1,1) mode is destabilized before (2,1) becomes stable.

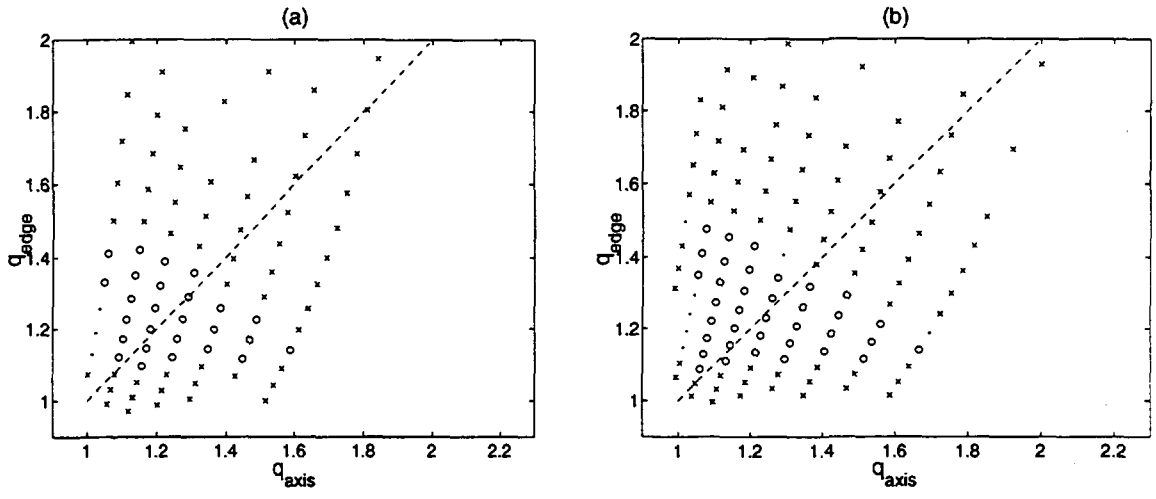

Figure 5.11: *Stability area of the* $(2,1)$ *mode* ($\mathcal{T}_{2,1}^{nores}$ *set) in mixed* $L = 2$ *and* $L = 3$ *configurations for* (a) $\delta_2/\delta_3 = 2.0$ *and* (b) $\delta_2/\delta_3 = 2.5$. *The equilibria are characterized by* $N_{per} = 5$, $1/\epsilon_c = 8$, $\beta = 1\%$, pr^B *and* $J'(s)/J'_{norm} = a_1(1 - s^{1.2})^2$

The last boundary deformation tested belonged to a new type: we superposed on the helical $L = 3$ a fixed axisymmetric triangular boundary deformation measured by a parameter δ_{axi}.

$$\begin{cases} R(s=1,u,v) &= R_0 + cosu + \delta_3(...) + \delta_{axi}\,(cos(2u)) \\ Z(s=1,u,v) &= sinu + \delta_3(...) + \delta_{axi}\,(sin(2u)) \end{cases} \tag{5.4}$$

The aim was twofold: to slow down the diminishing of q_{edge} so as to reach the Kruskhal-Shafranov limit at a higher δ and to observe the consequences of having a boundary deformation which was no longer purely helical. Two values were considered $\delta_{axi} = 0.03$ and 0.09. Fig.5.13 shows the resulting equilibrium flux surfaces produced by VMEC. It is visible how δ_3 and δ_{axi} reinforce one another at the toroidal angle $2\pi/N_{per}$ and how their effects are opposed at π/N_{per}.

The result was that the decrease of the q profile and in particular of q_{edge} was less rapid than in a pure $L = 3$ case, but the SA were sensibly reduced (Fig.5.13) indicating a less efficient stabilization.

• pressure profile and β

If the pressure on the magnetic axis i.e. the p_0 factor from Eq.(3.9) or Eq.(3.10) is kept fixed when calculating an equilibrium sequence, then β changes when δ is increased. The two plots from Fig.5.14 show that $\beta(\delta)$ is very well approximated by a linear function :

$$\beta \simeq a\delta + \beta_0 \tag{5.5}$$

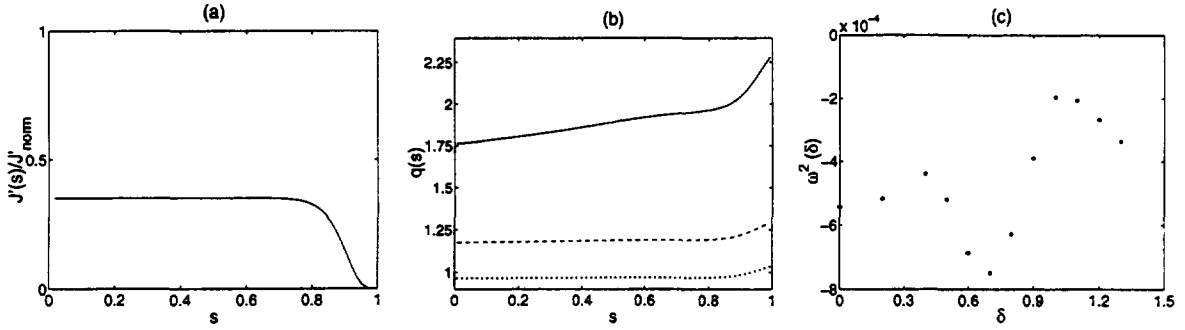

Figure 5.12: *Study of the (2,1) mode:* (a) $J'(s)$ *profile,* (b) $q(s)$ *profile and* (c) $\omega^2_{min}(\delta)$ *for a mixed* $L = 1$ *configuration,* $N_{per} = 4$, $1/\epsilon_c = 10$, *at* $\beta = 1\%$, *with pressure profile* pr^A *and toroidal current density given by* $J'(s)/J'_{norm} = 0.35(1 - s^{20})^8$. q *is represented for* $\delta_1 = 0.000$ *(–),* 1.000 *(- -) and* 1.300 *(·). For* $\delta_1 \leq 0.4$ *the (3,1) component dominantes, between* $0.5 \leq \delta_1 \leq 1.0$ *the* $(2,1)$ *component is the most unstable followed by* $(1,1)$ *for* $\delta_1 \geq 1.1$.

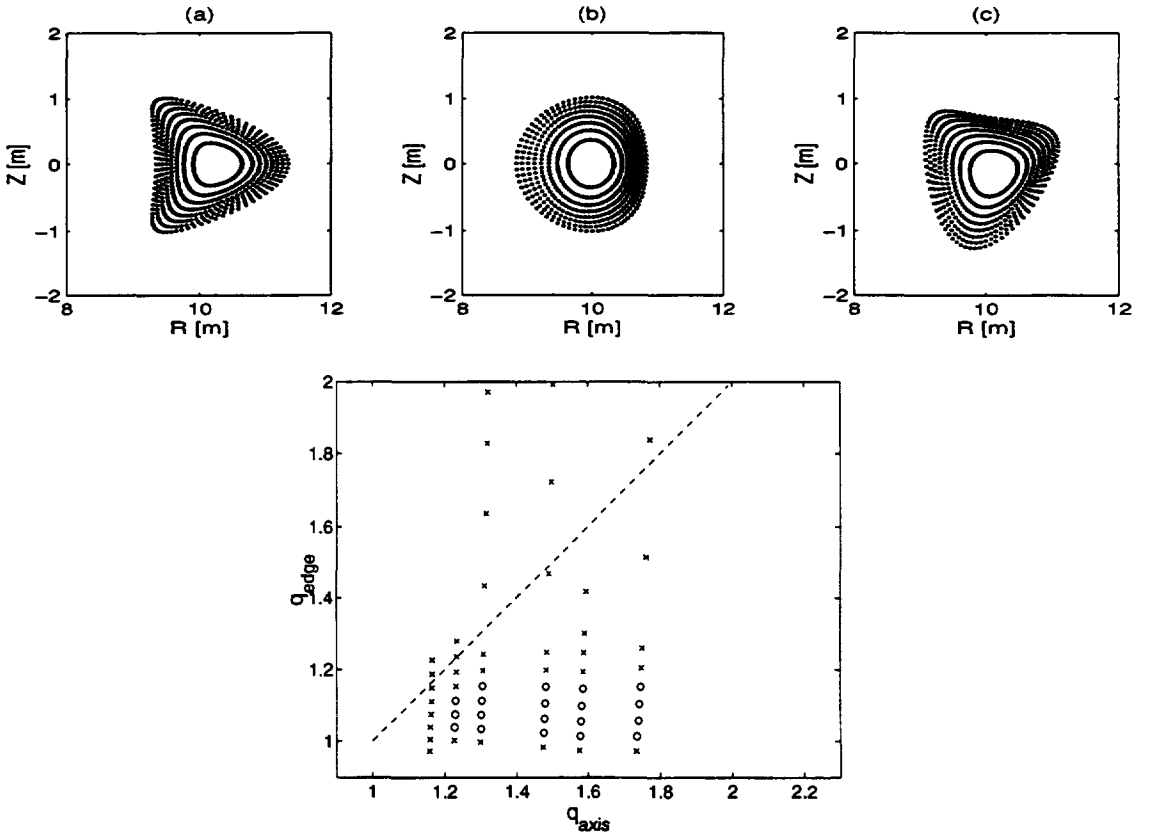

Figure 5.13: *Flux surfaces produced with VMEC for configurations with a* $L = 3$ *helical deformation and a fixed axisymetric triangular deformation at* $\delta_{axi} = 0.090$, $\delta_3 = 0.110$, $1/\epsilon_c = 10$, *and* $\beta = 1\%$. *The plots were made for toroidal angles 0 (a),* $\pi/(N_{per})$ *(b) and* $3\pi/(2N_{per})$ *(c). The stability area when the current density profile was of the form* $J'(s)/J'_{norm} = a_1(1 - s^5)^2$ *is shown above. The mode studied was* $(2,1)$

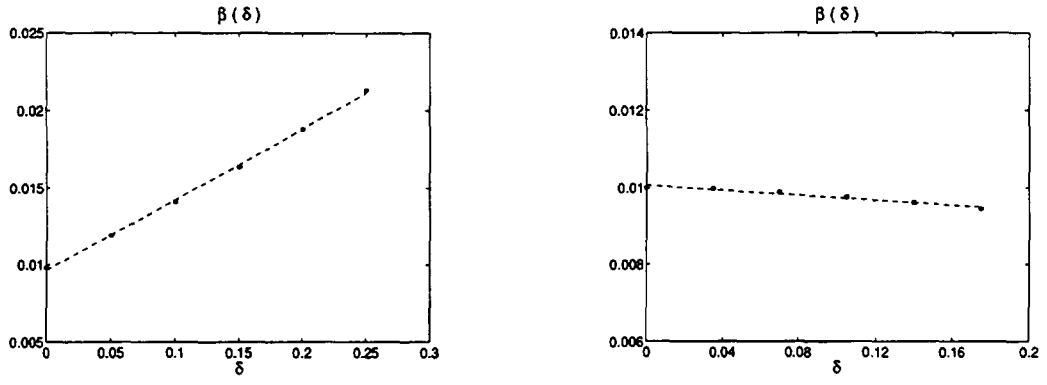

Figure 5.14: *Variation of β with δ when p_0 is constant.*
(left) *$L = 2$ configuration with $N_{per} = 5$, $1/\epsilon_c = 10$, pr^B, $J'(s)/J'_{norm} = 0.35(1 - s^{20})^8$.*
(right) *$L = 3$ configuration with $N_{per} = 4$, $1/\epsilon_c = 8$, pr^B, $J'(s)/J'_{norm} = 0.45(1 - s^{2.5})^2$.*

with $\beta_0 = \beta(\delta = 0)$ (or $\beta(\delta = \delta_{start})$. It is sufficient to estimate a from a number of preliminary runs and to make the substitution $p_0 \to p_0/(p_0 + a\delta)$ to assure a constant β throughout the whole equilibrium sequence (the remaining relative variations of β never exceeded 2%). The a coefficient has to be calculated for each combination of current density and pressure profiles, N_{per} and inverse aspect ratio. It is always positive and larger for $L = 2$ configurations and negative and smaller for $L = 3$ configurations.
Concerning the influence of the pressure profile on the stabilization process, we did not observe major modifications of the size or position of the stability areas when changing from pr^A to pr^B. At $\beta = 1\%$, SA were obtained for a large variety of combinations of L, N_{per}, ϵ and current profiles. At $\beta = 2\%$ calculations were done only for $1/\epsilon_c = 10$ and we found that it is still possible to find stable areas but they are strongly diminished and exist only for a reduced set of combinations of equilibrium parameters.
We add that the pr^A pressure profiles produce equilibria with much larger Shafranov shifts (nearly two times more) than the pr^B pressure profiles.

• limit of the stability area at high q_{axis}

The definition of a clear SA boundary at large q_{axis} stumbles on several difficulties. If the current density decreases the equilibria are characterized by large Shafranov shifts; in general at $\delta = 0$ $\Delta_{Shf} \sim 5 - 10\%$. For low, peaked current densities and with the pr^A pressure profile, $\Delta_{Shf}(\delta = 0)$ can exceed 20%. In such cases, one is skeptical about the quality of the computed equilibria. At lower currents, VMEC does not converge and the circular tokamak equilibrium does not even exist
Hopefully, when δ is increased Δ_{Shf} decreases. For $L = 2$ configurations Δ_{Shf} is diminished by a factor of 2 and more when going from $\delta = 0$ to a $\delta \in I^{stb}_{2,1}$. However, even with strong boundary deformations, a weak current can give Δ_{Shf} of the order of 15-20 % and more. When these values were encounterd we stopped the investigations; for peaked

currents at high $1/\epsilon$ such problems appeared for $q_{axis} \geq 1.8$, whereas for hollow currents Δ_{sh} remained acceptable beyond $q_{axis} = 2.0$.
The pr^B parabolic pressure profile was introduced with the aim of reducing the Shafranov shift. It effectively brought down these large Δ_{Shf} to values of $4 - 9\%$ and pushed the above mentioned limits of q_{axis}. However, we still could not continue toward lower currents, because the weak pressure gradient on the flux surfaces near the magnetic axis caused increasing convergence problems in computing the equilibria.
Another problem comes from the fact that in that part of the SA situated generally in the $q_{axis} \geq 2$ region, the stable eigenvalues ω^2_{min} tend to be very weak. In many cases convergence studies in the number of radial mesh points, indicate that the eigenvalues tend to be marginally stable or even worse they may change sign (this did not happen in the $q_{axis} \leq 2$ region). The work required to check and assure the validity of the numerical results seems to be much more important in that part of the q_{axis}, q_{edge} plane.
For these reasons we decided to avoid the exploration of the limit of the SA at large q_{axis}.

• **stability areas associated with the** $(3,2)$ **and** $(4,3)$ **modes**
All the results that follow were obtained at $\beta = 1\%$. The resonant value of this mode is $q_{res} = 1.5$. The amount of boundary deformation needed to stabilize it is less important than that for the $(2,1)$ mode but less room is left before the $q_{min} \simeq 1$ limit is reached (see Fig.5.7). It follows that the stability windows are narrower than those of the $(2,1)$ mode; the stable areas are consequently reduced in size (compare Fig.5.15 with Fig.5.9). From Fig.5.15 we see that in the $q_{axis} < 2$ region the SA are situated below $q_{edge} = 1.2$. In particular, the stability areas associated with peaked current density profiles rarely extend above the $q_{axis} = q_{edge}$ diagonal.
Above $q = 1.5$ the dominant instability come from the $(4,2)$ component or components with higher m's depending on the inverse rotational transform profile (Fig.5.7). When $q(s) < 2$, there is a single window of stability in which the $(m,2)$, $m > 2$ modes are stable and $(2,2)$ is not yet excited. This may change if $q_{axis} > 2$ and $q(s) > 1.5$; in Fig.5.15, the equilibrium sequence with the largest q_{axis} ($\simeq 2.2$) shows a stable point situated at $q_{axis} = 2.211$, $q_{edge} = 1.613$ ($q_{min} = 1.597$). Around this point ($\delta_3 = 0.107$) a stability window may exist in which the $(m,2)$, $m \geq 4$ modes are stabilized and the $(3,2)$ mode was not yet destabilized. We did not study this new stability area because our concern was the $q < 2$ region; we prefered to investigate that part of the $\{q_{axis}, q_{edge}\}$ plane where the $n = 1$ modes and the $n = 2$ modes were susceptible to have a common stability area.
The areas in which the $(4,3)$ mode is stable are even less extended; the resonant value triggering its destabilization is $q_{res} = 1.\bar{3}$ and the SA is situated below $q_{edge} = 1.1$ (see Fig.5.3). Here again we have a point ($q_{axis} = 2.403$, $q_{edge} = 1.413$, $q_{min} = 1.395$) at which the $(5,3)$ mode is stable and the $(4,3)$ mode is not yet destabilized.

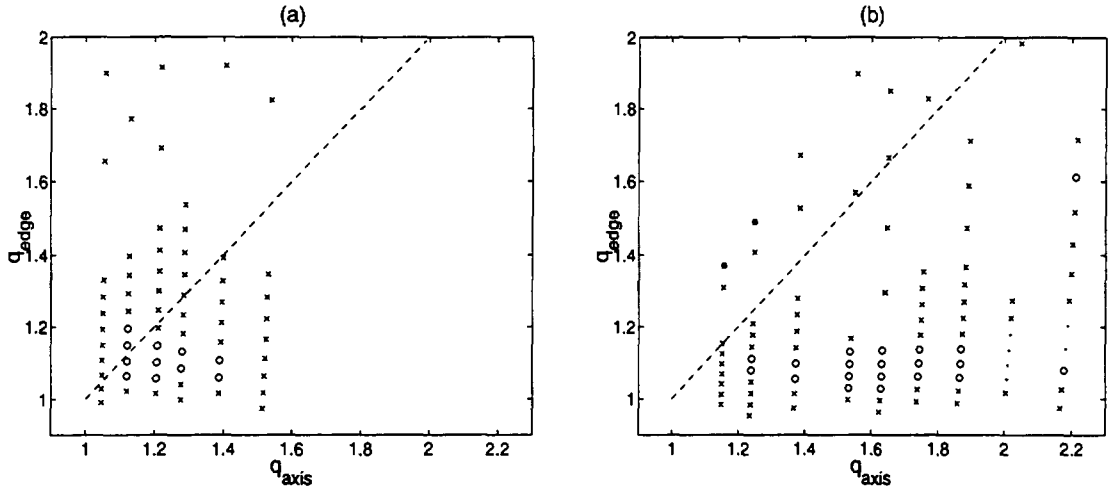

Figure 5.15: Stability area of the $(3,2)$ mode; the equilibria are characterized by $L = 3$, $N_{per} = 4$, $1/\epsilon_c = 10$, $\beta = 1\%$, pr^B. The current density profiles are peaked **(a)** $J'(s)/J'_{norm} = a_1(1-s^{2.5})^2$ or broad **(b)** $J'(s)/J'_{norm} = a_1(1-s^{20})^8$.

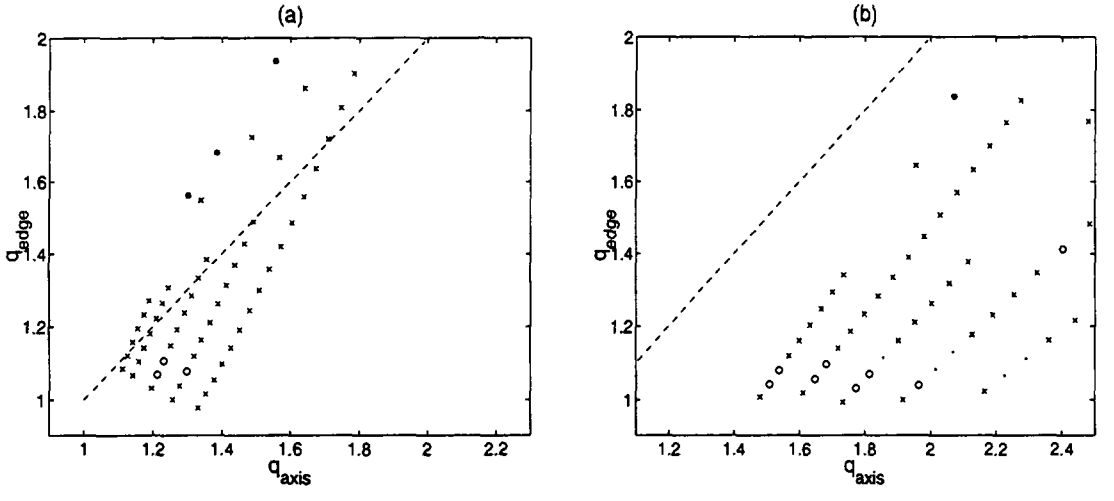

Figure 5.16: Stability area of the $(4,3)$ mode; the equilibria are characterized by $L = 2$, $N_{per} = 5$, $1/\epsilon_c = 10$, $\beta = 1\%$, pr^5. The current density profiles are broad **(a)** $J'(s)/J'_{norm} = a_1(1-s^{20})^8$ or hollow **(b)** $J'(s)/J'_{norm} = a_1(1-s^{10})^2 - 0.4(1-s^{2.5})^2$.

If we extrapolate our results to modes with $n \geq 4$ we may come to the conclusion that there is no finite common stability area associated to all n 's under the $q < 2$ region and at the values of β of the order of 1 %

5.4 Mercier and ballooning results

The study of the the dependence of the Mercier criterion on the boundary deformation lead us to the following conclusions:
- At small values of δ (including $\delta = 0$) we have found many different configurations for which D_M is stable on each flux surface. Fig.5.17 (a), Fig.5.18 (a) and Fig.5.19 (a) illustates this situation for $L = 2$, 3 and mixed boundary deformations with broad or hollow current density profiles.
- When δ is increased D_M decreases. If a threshold value δ_M is attained some flux surfaces become Mercier unstable. δ_M depends sensibly on the equilibrium parameters; its highest value was obtained with low, peaked currents and pr^A profiles.For $\delta > \delta_M$ more and more surfaces are destabilized. This is also shown in Fig.5.17 (a), Fig.5.18 (a) and Fig.5.19 (a) and (b) ; the broken lines correspond to the Mercier criterion evaluated at a value of δ superior to δ_M. The aim was to have $\delta_M > \delta_{min}$ but in almost all studied cases this was not true.
- When δ is further increased two situations may arise:
1) In most of the cases and generally in the region corresponding to $q_{axis} < 2$, significant toroidal currents and small Δ_{Shf} the Mercier criterion continues to decrease - see Fig.5.17 (a) and Fig.5.19 (a).
2) For some cases characterized by $q_{axis} > 2$ and a large Shafranov shift ($\Delta_{Shf} > 12\%$), $D_M(s)$ decreases until it attains a minimum profile after which it starts increasing. Fig.5.17 (b) and Fig.5.18 (a) illustrate this situation. With respect to the stability window (of the $(2,1)$ mode), the Mercier criterion appears to be satisfied only for $L = 3$ configurations at $1/\epsilon_c \geq 8$, weak currents i.e toward the right edge limit of the SA in the (q_{axis}, q_{edge}) plane, where the quality of the numerical equilibria degrades.

In general, for small deformations a weak magnetic well exists but it becomes smaller when δ is increased. For $L = 3$ configurations, the magnetic well almost vanishes for values of δ in the stability window and for $L = 2$ configurations it generally transforms into a magnetic hill. The evolution of the differential volume $dV(\Phi(s))/ds$ is shown in Fig.5.18 (b) for a $L = 2$ case (the same as in Fig.5.1) and in Fig.5.19 (b) for a mixed $L = 2$ and $L = 3$ case (the same as in Fig.5.19).

The study of the ballooning stability was not the purpose of this work and the results which follow come from a reduced number of calculations done for a few selected cases (15 equilibrium sequences). We worked only at $\beta = 1\%$ and with the pr^A pressure profile to avoid larger gradients toward the plasma edge associated with pr^B. For each equilibrium

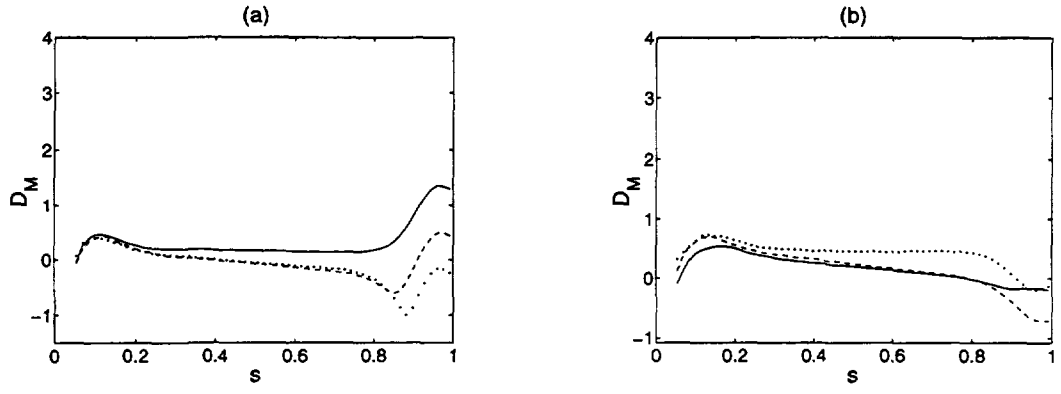

Figure 5.17: *The Mercier criterion evaluated at three values of δ in the case of two equilibrium sequences that differ in the amount of plasma current they carry. Positive/negative values of D_M indicate stability/instability. :*
(left) *$J'(s)/J'_{norm} = 0.5(1-s^{20})^8$ at $\delta_3 = 0$ (-), 0.090 (-) and 0.114 (·). The stability window is situated between the last two values and the Shafranov shift Δ_{Shf} varies between 6.3% (-) and 4.76% (·).*
(right) *$J'(s)/J'_{norm} = 0.25(1-s^{20})^8$ at $\delta_3 = 0.093$ (-), 0.121 (-) and 0.170 (·). The stability window is situated between the last two values and the Shafranov shift Δ_{Shf} varies between 15.42% (-) and 9.90% (·).*
The equilibria are characterized by $L = 3$, $N_{per} = 4$, $1/\epsilon_c = 10$, $\beta = 1\%$ and pr^B.

sequence considered we chose values of δ outside (before) and inside the stability window (corresponding to the global $(2,1)$ mode) and tested only a few number of magnetic lines (with $\alpha = 0$, $\pi/(4N_{per})$ and $\pi/(2N_{per})$. The results can be summarized as follows:
- all $L = 2$ studied configurations were unstable to ballooning modes either at small or at large boundary deformations. Fig.5.20 shows the dependence on s of the eigenvalues $\lambda(s,\theta_k)$ c.f. Eq.(2.48) and of the amplitudes of the five most important Fourier components of the normal curvature κ_n

$$\kappa_n = \vec{\kappa} \cdot \vec{\nabla}(s) \tag{5.6}$$

with the curvature vector given by $\vec{b}\cdot\vec{\nabla}\vec{b}$. The ballooning instability deteriorates when the boundary deformation is increased from a small-moderate value $\delta = 0.100 < \delta_{min} \leq 0.190$ to a stronger value $\delta = 0.240$ situated inside the stability window corresponding to the $(2,1)$ mode. We notice that the eigenvalues associated with the three magnetic lines are undistinguishable.
- for $L = 3$ configurations we found that at small boundary deformations, there are always some flux surfaces on which the magnetic lines studied are unstable; on these surfaces the shear is weak. At stronger δ 's, if the q profile is such that the shear is relatively large in the whole plasma domain, then, for the magnetic lines tested $\lambda(s,\theta_k) < 0 \ \ \forall s$. Fig.5.21 illustrates such a case. We notice that for $\delta = 0.075$ ($\delta_{min} \simeq 0.120$), the $\lambda(s,\theta_k)$

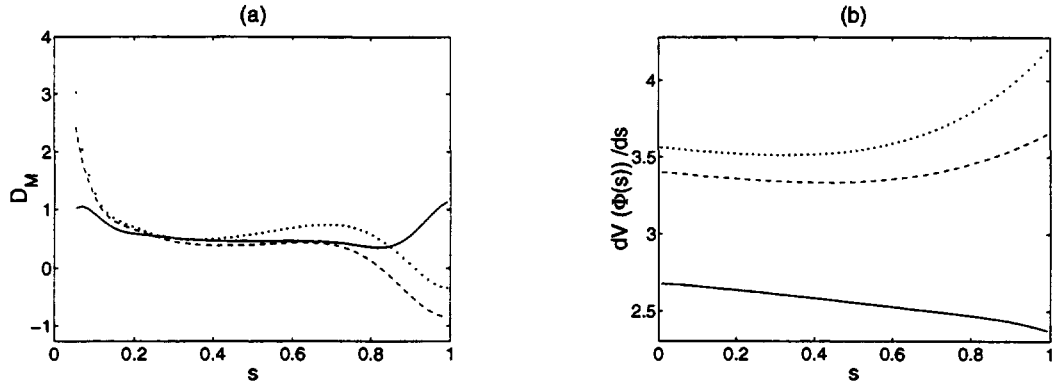

Figure 5.18: *(a) The Mercier criterion D_M and (b) the differential volume $|V'(\Phi(s))|$ as functions of s for three values of δ. The parameters are those of Fig.5.1 i.e. $L = 2$, $N_{per} = 5$, $1/\epsilon_c = 5$, pr^A pressure profile, $\beta = 1\%$, $J'(s)/J'_{norm} = 0.9(1-s^{10})^2 - 0.4(1-s^{2.5})^2$ at $\delta_2 = 0.010$ (-), 0.180 (- -) and 0.230(·). The magnetic well is changed into a magnetic hill; the Mercier criterion which is stable for the circular tokamak is unstable in the window* $0.180 < \delta_2 < 0.230$ *near the plasma edge.*

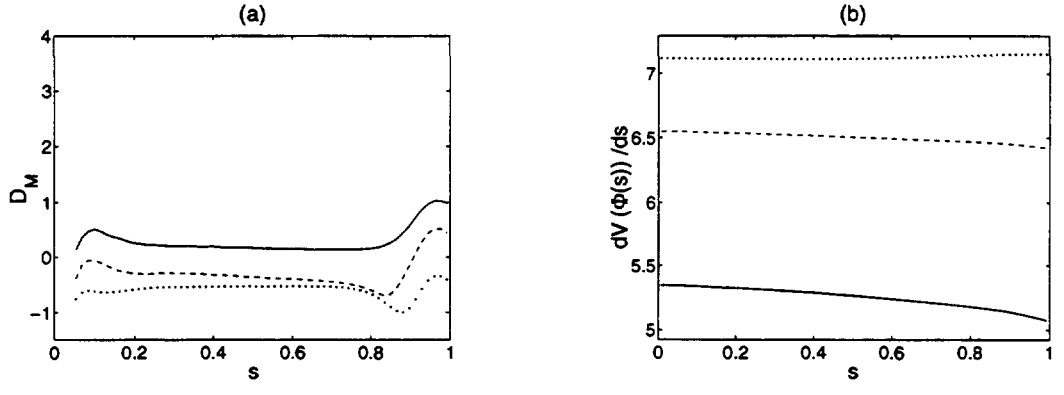

Figure 5.19: *(a) The Mercier criterion D_M and (b) the Differential volume $|V'(\Phi(s))|$ as functions of s for three values of δ. The parameters are those of Fig.5.2 i.e. a mixed L=2,3 configuration, $N_{per} = 4$, $1/\epsilon_c = 10$, pr^B pressure profile, $\beta = 1\%$, $J'(s)/J'_{norm} = 0.440(1-s^{20})^8$ at $\delta_3 = 0.010$ (-), 0.060 (- -) and 0.085 (·). The magnetic well decreases with δ and is reduced to zero at $\delta_{max} = 0.085$. The Mercier criterion, stable at $\delta_3 = 0.010$, is unstable for* $0.060 < \delta_3 < 0.095$.

eigenvalues are again nearly undistinguishable from field line to field line; κ_n is dominated by the (1,0) component followed by the (2,0) component. At $\delta = 0.150$ ($\delta_{max} \simeq 0.160$) the tested lines are stable; $(\kappa_n)_{3,3}(s)$ and $(\kappa_n)_{2,3}(s)$ come in the second and third position after $(\kappa_n)_{1,0}(s)$.

In general peaked and broad current density profiles are more likely to produce q profiles with a region of weak shear at strong δ 's (see for example Fig.5.3 and Fig.5.2) and can therefore lead more easily to ballooning instability (at strong δ in the stability windows). The case presented in Fig.5.21 was a particular optimized result.

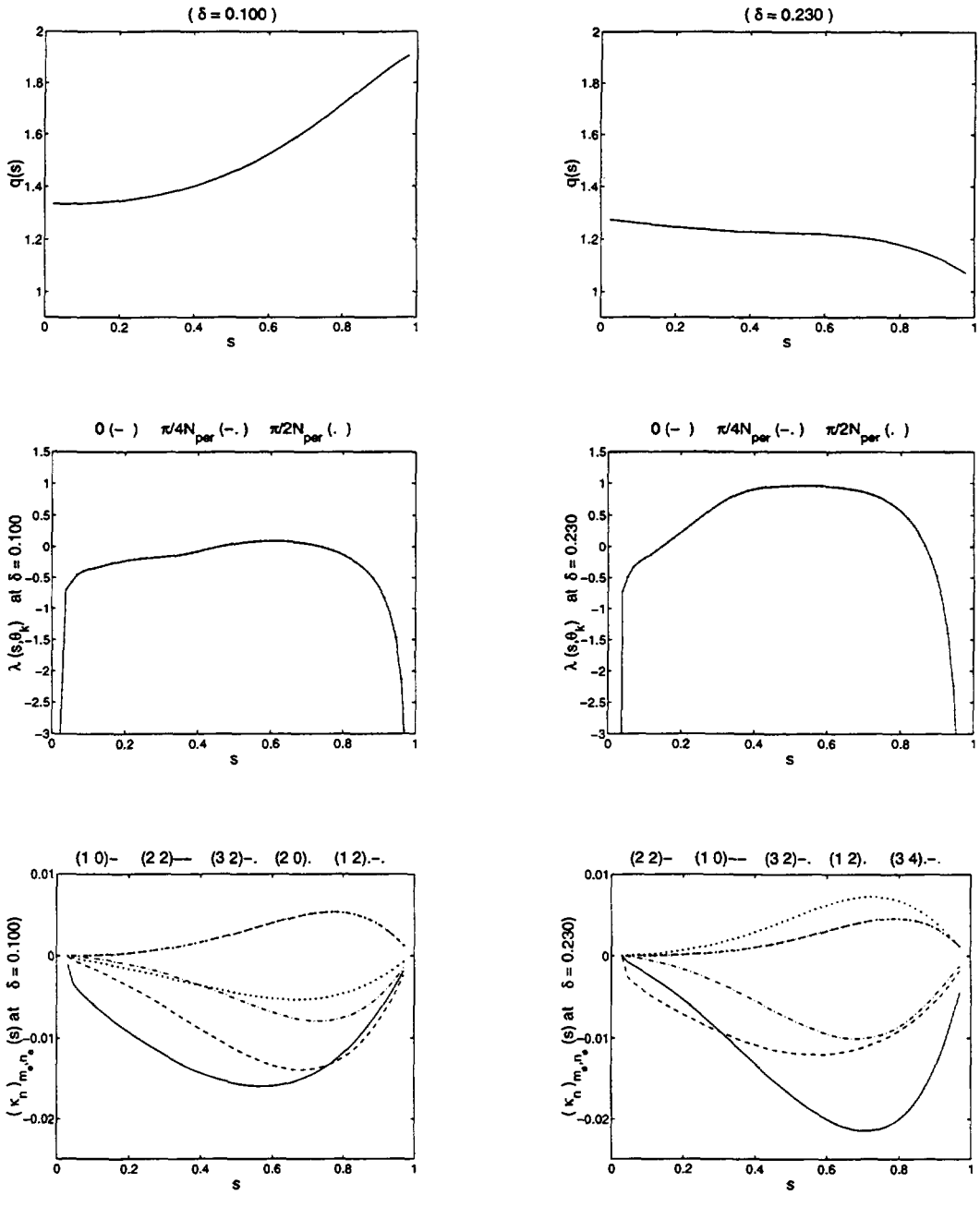

Figure 5.20: *Ballooning study results for* $L = 2$, $N_{per} = 5$, $1/\epsilon_c = 5$, *at* $\beta = 1\%$, pr^3 *and* $J'(s)/J'_{norm} = 0.9(1 - s^{2.5})^2$. *The figures on the left correspond to* $\delta_2 = 0.100$ *and the figures on the right to* $\delta_2 = 0.230$. *The first row shows the* q *profiles at these values of the boundary deformation. The eigenvalues* $\lambda(s, \theta_k)$ *c.f. Eq.(2.48) associated with three particular field lines are shown in the two middle plots and the dominant Fourier components of* $(\kappa_n)_{m_e,n_e}$ *of the normal curvature, are displayed in the lower two plots. Positive values of* $\lambda(s, \theta_k)$ *are unstable and negative values are stable. The stability window of the* $(2, 1)$ *mode is* $0.190 < \delta_2 < 0.240$.

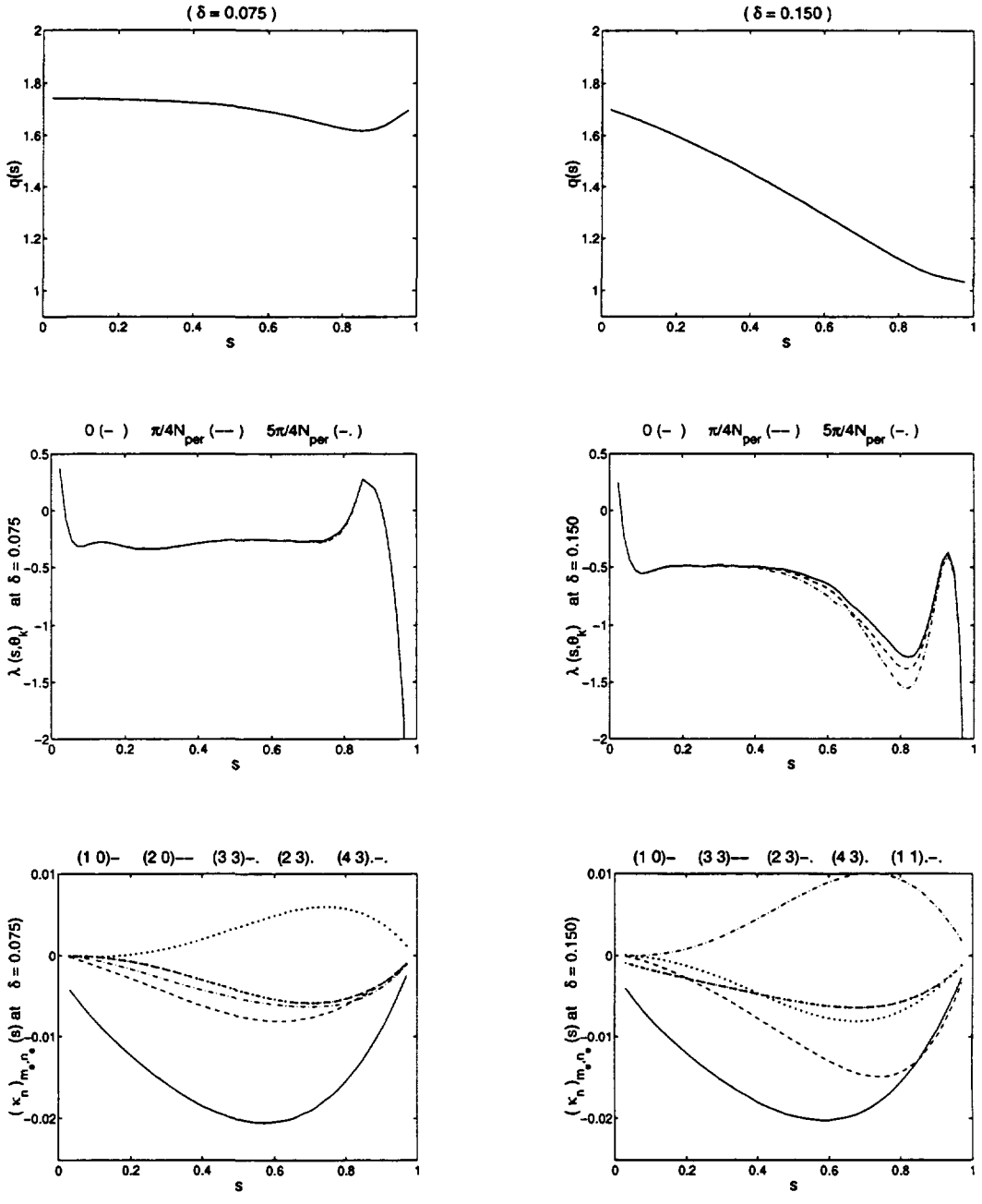

Figure 5.21: *Ballooning study results for* $L = 3$, $N_{per} = 4$, $1/\epsilon_c = 10$, *at* $\beta = 1\%$, pr^3 *and* $J'(s)/J'_{norm} = 0.35(1 - s^{20})^8$. *The figures on the left correspond to* $\delta_3 = 0.075$ *and the figures on the right to* $\delta_3 = 0.150$. *The first row shows the* q *profiles at these values of the boundary deformation. The eigenvalues* $\lambda(s, \theta_k)$ *c.f. Eq.(2.48) associated with three particular field lines are shown in the two middle plots and the dominant Fourier components of* $(\kappa_n)_{m_e,n_e}$ *of the normal curvature, are displayed in the lower two plots. Positive values of* $\lambda(s, \theta_k)$ *are unstable and negative values are stable. The stability window of the* $(2, 1)$ *mode is* $0.120 < \delta_3 < 0.160$.

Chapter 6

Free Boundary calculations

6.1 Introduction

In this chapter we reconsider the study of the global stability of the external kinks when the equilibria are calculated with a free boundary code. The aim is twofold:
1) To test how difficult it is to obtain free boundary equilibria with single helicity bounadry deformation at nonzero plasma current and positive β. For this purpose we design a system of coils producing a toroidal, a vertical and a helical field and find the currents (flowing through the coils) needed to obtain the desired type of boundary deformation. The field produced by these external currents is given then as input to the free-boundary equilibrium code NEMEC (c.f. Appendix E).
2) To determine the validity of the fixed boundary calculations; we hope to obtain stability windows for the mode studied when the amount of boundary deformation is monotonously increased.
It is not a systematic study. We do not consider the coil optimization aspect of the problem and work with a minimum number of coils, each of them being approximated by a single current filament. We avoid increasing the number of variables (more coils or more filaments per coil) even if this offers more flexibility for the fine tuning of the flux surfaces. We also do not explore the consequences of the additional parameters as the coil geometry and the external currents on the investigation procedure (of the global stability). This would possibly lead to new stability diagrams (areas) in the $\{q_{axis}, q_{edge}\}$ plane, but we do not follow this approach.
Our concern is to find one combination of parameters (coil geometry, external currents, plasma parameters) which fulfills objectives 1) and 2) and opens thus the way for future investigations.

6.2 Flux surfaces in vacuum

The vacuum field necessary to calculate the free boundary equilibrium is produced by the COILS code which was written for that purpose. We assume a configuration consisting of a set of circular coils producing the toroidal field (TF),a set of circular coils which create the vertical field (VF) and a set of helical coils that generate the helical field (HF). The resulting $\vec{B}$ is calculated from the Biot-Savart law.
The TF coils are characterized by their radius R_t which is the same for all coils, their number N_t and the current flowing through them I_t. These coils are aligned vertically and their centers are placed equidistantly around a major circle of radius R_h.
The HF coils lay on a circular torus of minor radius r_h and major radius R_h; the cartesian coordinates of the segments that describe the coils are given by

$$\begin{aligned} x &= (R_h + r_h cosu)cosv \\ y &= (R_h + r_h cosu)sinv \\ z &= r_h sinu \end{aligned} \tag{6.1}$$

with u and v the geometrical poloidal and toroidal angles. The helical conductors are wound on the torus with the following winding law:

$$\begin{aligned} \tilde{u} &= u + 2\pi\frac{l-1}{L} + u_0 \\ v &= \frac{1}{N_{per}}(\tilde{u} + \alpha sin(\tilde{u})) - \frac{l}{L}\frac{2\pi}{N_{per}} \end{aligned} \tag{6.2}$$

Here $l = 1,..L$ is an index specifying a particular coil and α is a pitch modulation coefficient which is introduced to compensate for the loss of the helical symmetry due to toroidicity. The L and N_{per} parameters have the same meaning as in the previous chapters. The effect of $\alpha \neq 0$ on the coil shape is shown in Fig.F.1.
Eq.(6.2) describes a heliotron configuration (or torsatron configuration if the TF coils are not present) with exactly L coils and all the currents flowing in the same direction. Stellarator-like configurations can also be studied by intercalating another set of L helical wires such that the resulting $2L$ currents flow in alternate directions.

There are three pairs of VF coils; a coil belonging to the i pair, i = 1,2,3, is parametrized by R_{vi} the radius of the coil, Z_{vi} the height at which its center is placed ($-Z_{vi}$ for the second coil) and I_{vi} the current flowing through it - see Fig.F.2.

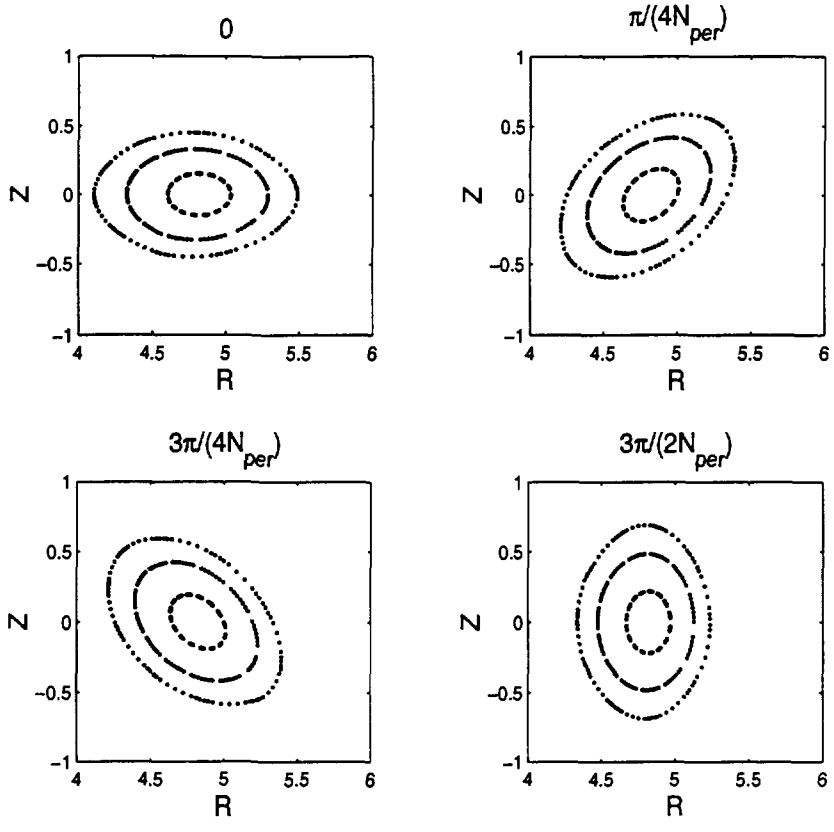

Figure 6.1: *Cross sections at four toroidal angles showing three field lines for a* $L = 2$ *stellarator configuration. There are 16 TF coils with* $R_h = 5.0\,[m]$, $R_t = 1.8[m]$, $I_t = -1.6 \cdot 10^5[A]$ *and two pairs of HF coils* $r_h = 1.4[m]$, $\alpha = -0.15$, $I_h = \pm 1 \times 10^5[A]$. *An estimation of the inverse rotational transform values gives* $q \simeq 4.50$, *3.75 and 2.50 for the inner, middle and outer surfaces respectively*

Field line tracing routines were added to COILS and a preliminary study was done in order to determine the coil parameters necessary to produce closed flux surfaces in vacuum. We arrived at the following results:

A. Flux surfaces in vacuum produced with a $L = 2$ stellarator configuration of coils.

Fig.6.1 shows closed flux surfaces produced by a configuration characterized by

$$R_h = 5.0\,[\mathrm{m}]\ ,\ R_t = 1.8\,[\mathrm{m}]\ ,\ r_h = 1.4\,[\mathrm{m}]\ ,\ \alpha = -0.150$$
$$I_t = -1.6 \times 10^5[A]\ ,\ I_h = \pm 1 \times 10^5[A]$$

There are no currents in the VF coils; a negative current flows clockwise through the coil considered. A rough estimate of the inverse rotational transform gives $q_i \simeq 4.5$ and $q_o \simeq 2.5$ for the innermost and outermost field lines respectively. The flux surfaces are relatively robust with respect to small changes of the geometry or of currents flowing

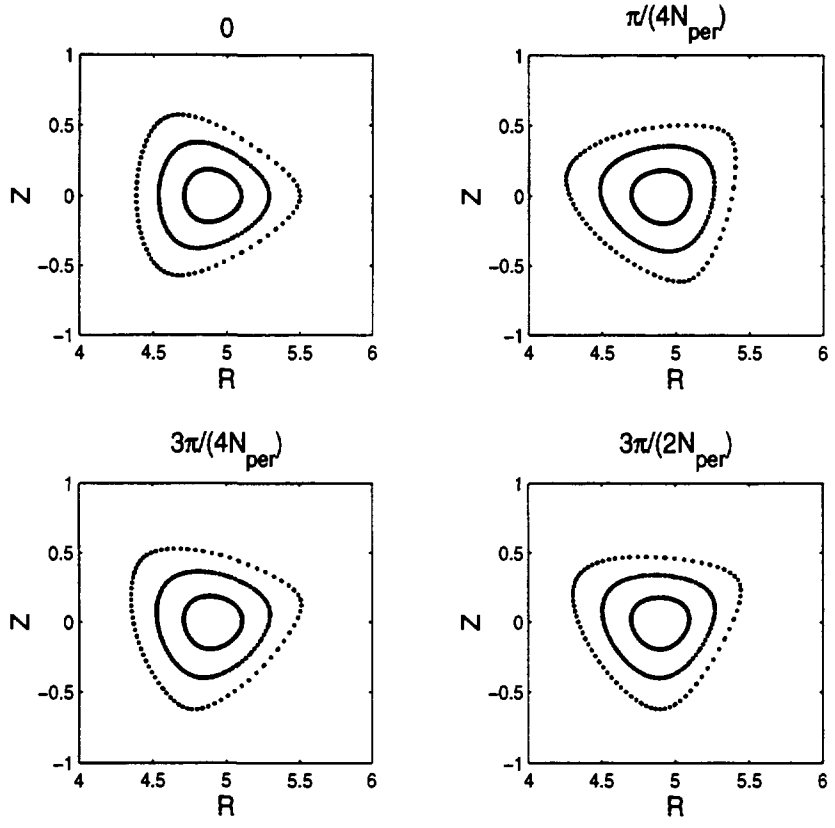

Figure 6.2: *The same as in Fig.6.1 for a $L = 3$ stellarator configuration. There are 16 TF coils with $R_h = 5.0\,[m]$, $R_t = 1.8[m]$, $I_t = -0.5 \times 10^5[A]$, and six HF coils with $r_h = 1.4\,[m]$, $\alpha = -0.05$ and $I_h = \pm 0.66 \times 10^5[A]$. An estimation of the inverse rotational transform values gives $q \simeq 25$, 7.50 and 2.14 for the inner, middle and outer surfaces respectively*

through the coils. We mean by this that the cross sections continue to have a helical shape even if the current intensities or coil radii are varied by 10% or more. However, the inverse rotational transform may change strongly. For example if r_h is augmented to 1.5 [m], then the cross sections remain very similar but the previous two magnetic lines will be characterized by $q_i \simeq 7.5$ and $q_o \simeq 3.75$. If I_h is decreased to $0.9 \times 10^5\,[kA]$, the corresponding values are $q_i \simeq 5.62$ and $q_o \simeq 3.21$. The value of α represents a compromise; smaller or larger α 's cause pear-shaped deformations of the flux surfaces.

B. Flux surfaces in vacuum produced with a $L = 3$ stellarator configuration of coils.

The example shown in Fig.6.2 comes from the following choice of coils parameters:

$$R_h = 5.0\,[\mathrm{m}]\ ,\ R_t = 1.8\,[\mathrm{m}]\ ,\ r_h = 1.4\,[\mathrm{m}]\ ,\ \alpha = -0.050$$
$$I_t = -5.0 \times 10^4\,[A]\ ,\ I_h = \pm 6.6 \times 10^4\,[A]$$

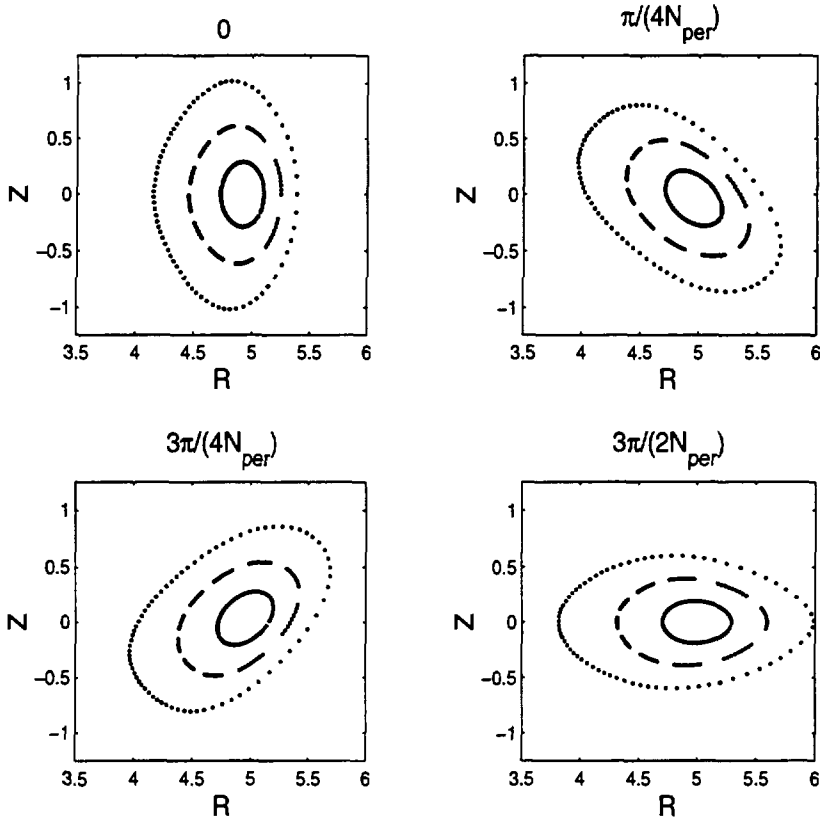

Figure 6.3: *Flux surfaces in vacuum produced with a $L = 2$ torsatron configuration consisting in one pair of HF coils and two pairs of VF coils (indexed with $_1$ and $_3$). The geometry is described by $R_h = 5.0\,[m]$, $r_h = 1.6\,[m]$, $\alpha = -0.175$, $R_{v1} = 7.0\,[m]$, $Z_{v1} = 2.1\,[m]$, $R_{v3} = 3.0\,[m]$ and $Z_{v3} = 0.5\,[m]$. The currents in the coils are $I_h = 1 \times 10^5[A]$, $I_{v1} = -3.9 \times 10^4[A]$, $I_{v3} = 2.1 \times 10^4[A]$. An estimation of the inverse rotational transform values give $q \simeq 3.21$, 2.81, and 1.73 for the inner, middle and outer surfaces respectively*

No VF coils are needed to produce closed flux surfaces in vacuum. Varying the above mentioned parameters and comparing the results with the preceding $L = 2$ case we have observed the following:

- the shear is very high: $q_i \simeq 25$ and $q_o \simeq 2.14$ on the innermost and outermost surfaces respectively. Huge q_{axis} values in vacuum are characteristic of this type of coil configuration; we recall that for a $L = 3$ linear stellarator magnetic field, ι is zero on the axis [41]. It is difficult to reduce the inverse rotational transform in the central region to lower values (typically < 10) by varying the ratio I_h/I_t or r_h.
- the maximum volumes that can be enclosed by the last closed surface seem to be smaller than those of the $L = 2$ configurations (In Fig.6.2 the outer surface is nearly the last closed surface; this is not the case in Fig.6.1)
- the cross sections of the flux surfaces are not strongly perturbed by small changes in the parameters of the coils.

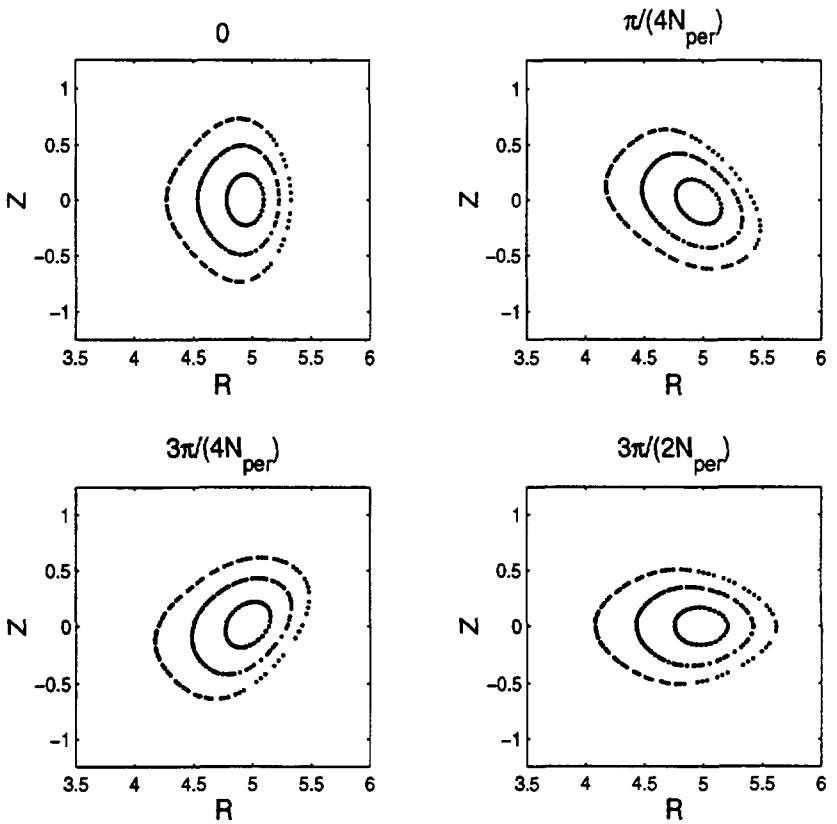

Figure 6.4: *Flux surfaces in vacuum produced with a $L = 2$ torsatron configuration consisting in one pair of HF coils and three pairs of VF coils. The geometry is described by $R_h = 5.0\,[m]$, $r_h = 1.7\,[m]$, $\alpha = 0.$, $R_{v1} = 7.0\,[m]$, $Z_{v1} = 2.1\,[m]$, $R_{v2} = 8.0\,[m]$, $Z_{v2} = 1.2\,[m]$, $R_{v3} = 3.0\,[m]$, $Z_{v3} = 0.5\,[m]$. The currents in the coils are $I_h = 1.0\times10^5[A]$, $I_{v1} = -3.9\times10^4[A]$, $I_{v2} = -1.0\times10^4[A]$, $I_{v3} = 2.1\times10^4[A]$. An estimation of the inverse rotational transform values give $q \simeq 5.20$, 4.50 and 3.75 for the inner, middle and outer surface respectively.*

C. Flux surfaces in vacuum produced with a $L = 2$ torsatron configuration of coils.

Since all the curents flow in a single direction, the HF coils produce a net toroidal field. We decided adopt the least flexible method for generating closed flux surfaces by eliminating the TF coils. Shape control of the flux surfaces is enabled with the introduction of several pairs of VF coils. An example of such a configuration is shown in Fig.F.4 (see also Fig.F.2). Two cases are presented.

1) $\underline{\alpha \neq 0}$ - with pitch modulation and two pairs of VF coils ($I_{v2} = 0$ it is possible to obtain closed magnetic surfaces with the desired helical shape - see Fig.6.3; the coils parameters are

$$R_h = 5.0\,[\mathrm{m}]\ ,\ r_h = 1.6\,[\mathrm{m}]\ \alpha = -0.175$$
$$R_{v1} = 7.0\,[\mathrm{m}]\ ,\ Z_{v1} = 2.1\,[\mathrm{m}]\ ,\ R_{v3} = 3.0\,[\mathrm{m}]\ ,\ Z_{v3} = 0.5\,[\mathrm{m}]$$

$$I_h = 1. \times 10^5\,[A],\ I_{v1} = -3.9 \times 10^4\,[A]\ ,\ I_{v3} = 2.1 \times 10^4\,[A]$$

The magnetic surfaces enclose a large volume and are relatively robust with respect to small variations ($\leq 5\%$) of the coil parameters.

2) $\underline{\alpha = 0}$ - even if the pitch modulation effect is abandoned, it is still possible to obtain cross section shapes dominated by a single helical component if a third pair of VF coils is added. One of the best result we have obtained is shown in Fig.6.4 for

$$R_h = 5.0\,[\mathrm{m}]\ ,\ r_h = 1.7\,[\mathrm{m}]\ \alpha = 0.$$
$$R_{v1} = 7.0\,[\mathrm{m}]\ ,\ Z_{v1} = 2.1\,[\mathrm{m}]\ ,\ R_{v2} = 8.0\,[\mathrm{m}]\ ,\ Z_{v2} = 1.2\,[\mathrm{m}]\ ,\ R_{v3} = 3.0\,[\mathrm{m}]\ ,\ Z_{v3} = 0.5\,[\mathrm{m}]$$
$$I_h = 1. \times 10^5\,[A],\ I_{v1} = -3.9 \times 10^4\,[A]\ ,\ I_{v2} = -1. \times 10^4\,[A]\ ,\ I_{v3} = 2.1 \times 10^4\,[A]$$

The deviations from the desired $L = 2$ helical cross section shape become visible (especially for the outer surface); the flux surfaces are very sensitive to small changes in the coil geometry or variations of the currents. As an example Fig.F.3 shows the deformations of the flux surfaces when the I_{v3} current is increased by 10% compared with Fig.6.4.
In both cases, the volume enclosed by the flux surfaces are very large.

6.3 NEMEC results

After having shown how to produce closed magnetic flux surfaces in vacuum we proceed to the next step which is the calculation of free boundary equilibria with finite β and nonzero toroidal plasma current. The aim is to obtain a sequence of equilibria with increasing helical boundary deformations and inverse rotational transform profiles in the region $1 < q(s) < 2$.The different equilibria are labelled by the current intensity in the HF coils I_h instead of the δ parameter. We are not going to study all the configurations presented in the previous Section; we select one type after considering the following points:

- At nonzero plasma current, the q profile will be totally different from that of the vacuum. The currents in the coils have to be adjusted such that the resulting q profile falls in the region of interest. It is important to have a configuration of coils which enables such a fine tuning.
- When I_h is monotonically increased, the Fourier coefficients describing the deformation of the free boundary should remain (strongly) dominated by the $(l-1, l)$ and $(l-1, l-2)$ components (for a $L = l$ configuration, in VMEC coordinates).

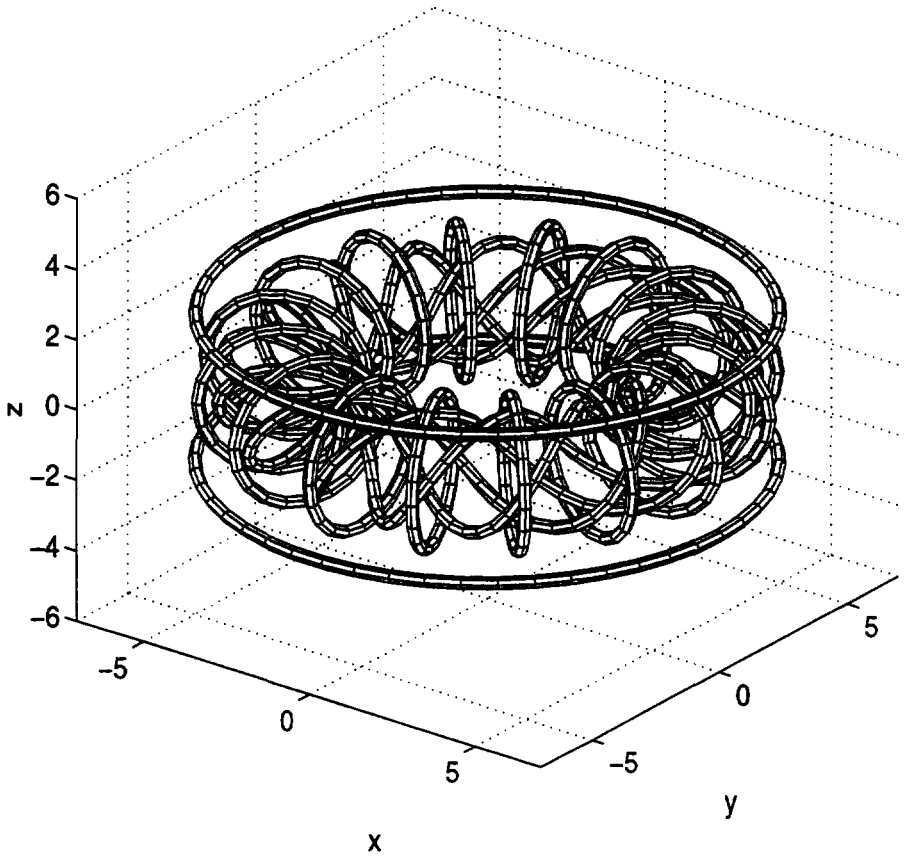

Figure 6.5: Configuration consisting in 16 TF coils, 2 pairs of HF coils (stellarator) and 1 pair of VF coils. Fig.6.1 shows the flux surfaces in vacuum obtained with this configuration when $I_v = 0$ (c.f. Section 6.2). If the coils and plasma input parameters are given by Eq.(6.3) and Eq.(6.4), the flux surfaces produced with NEMEC are displayed in Fig.6.6

• For $\beta > 0$, the flux surfaces will be not only shifted but also deformed and one should be able to correct this effect with appropiate changes of the coil currents.

We decided to consider the $L = 2$ stellarator configuration because it appears to be very flexible in coping with the constraints described above. We present a case with 16 TF coils and two pairs of HF coils to which we added one pair of VF coils - see Fig.6.5:

$$\begin{gathered} R_h = 5.0\,[m] \;\; R_t = 1.8\,[m] \;\; r_h = 1.4\,[m] \;\; \alpha = -0.150 \\ R_{v1} = 7.0\,[m] \;\; Z_{v1} = 2.1\,[m] \\ N_{per} = 4 \end{gathered} \tag{6.3}$$

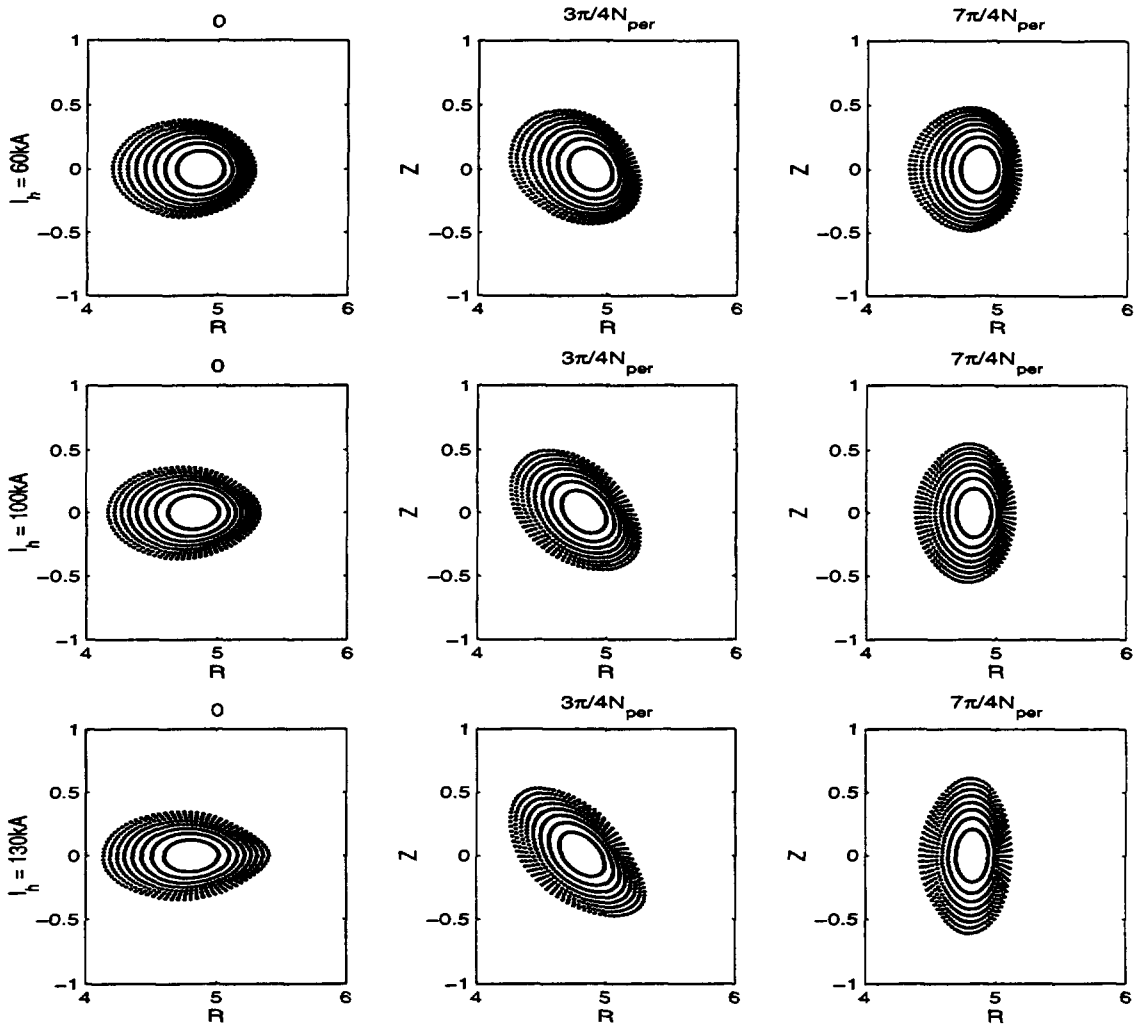

Figure 6.6: *Free boundary equilibrium flux surfaces produced with NEMEC. Each column represents the cross sections at one toroidal angle and each row is associated with one value of I_h. The coil geometry and plasma parameters are described by Eq.(6.3) and Eq.(6.4) respectively - see also Fig.6.5; the most important Fourier coefficients that describe the boundary are given in Tab.(6.1)*

The input plasma parameters for NEMEC were chosen

$$\begin{aligned} \beta &= 1\% \quad , pr^B \text{ pressure profile (Eq.(3.10))} \\ J'(s) &\sim (1 - s^{20})^8 \\ J &= 1.27 \cdot 10^5 [A] \text{ toroidal current} \end{aligned} \tag{6.4}$$

A number of preliminary runs (COILS + NEMEC) were done with the parameters given above to find at least one combination of coil currents i.e. I_t,I_h and I_{v1} such that the resulting equilibrium had a helical plasma boundary with a dominant $l = 2$ helicity and an inverse rotational transform profile satisfying $1 < q(s) < 2$. At this stage, the

$I_h \cdot 10^5\,[A]$	m_e^v	n_e^v	$R_{m_e^v n_e^v}$	m_e^v	n_e^v	$Z_{m_e^v n_e^v}$
0.6	1	0	4.886e-01	1	0	4.363e-01
	1	2	5.798e-02	1	2	-5.171e-02
	0	2	-1.040e-02	0	2	8.065e-03
	1	-4	-8.753e-03	1	-4	-7.542e-03
	2	0	-4.252e-03	2	2	-4.312e-03
1.0	1	0	4.806e-01	1	0	4.611e-01
	1	2	9.902e-02	1	2	-9.597e-02
	0	2	-1.535e-02	0	2	1.149e-02
	1	-4	-9.838e-03	1	-4	-9.251e-03
	2	2	6.765e-03	2	2	-7.076e-03
1.3	1	0	4.906e-01	1	0	4.795e-01
	1	2	1.419e-01	1	2	-1.422e-01
	0	2	-1.421e-02	0	2	1.678e-02
	1	-4	-1.126e-02	2	2	-1.118e-02
	2	2	1.050e-02	1	-4	-1.103e-02

Table 6.1: *The most important Fourier components (R_{00} and Z_{00} are not displayed) in VMEC coordinates describing the plasma boundary at three values of the current in the helical coils. The coil geometry and plasma parameters are those of Eq.(6.3) and Eq.(6.4), respectively; the corresponding flux surfaces cross sections are shown in Fig.6.6*

experience acquired when tracing field lines in vacuum with COILS was very useful. Once this particular equilibrium was found we proceeded further by varying I_h in several steps such as to cover the whole $1 \leq q_{edge} \leq 2$ interval. We did not change either I_t or I_{v1} ; at each step we adjusted the p_0 parameter (c.f. Eq.(3.9) or Eq.(3.10)) such as to keep $\beta \simeq 1\%$. If the conventional (tokamak) definition of normalized beta is used, $\beta_N = \beta / I_N$ with $I_N = J\,[MA]/(a\,[m]\,B_0\,[T])$ where a and B_0 are the averaged minor radius and the magnetic field intensity on the axis, respectively, we obtain $\beta_N \sim 4 - 6$.
Fig.6.6 shows an example of flux surfaces produced by NEMEC for three values of the HF coils current

$$I_h = 0.6 \times 10^5[A]\ ,\ 1 \times 10^5[A] \text{ and } 1.3 \times 10^5[A]$$

when the currents flowing in the TF and VF coils are given by

$$I_t = -1.6 \times 10^5[A]\ ,\ I_{v1} = 1. \times 10^4[A]$$

The corresponding q profiles are presented in Fig.6.8 (b) and the most important equilibrium Fourier amplitudes (in VMEC coordinates) $R_{m_e^v n_e^v}$, $Z_{m_e^v n_e^v}$ describing the boundary are given in Tab.(6.1). The boundary shape is dominated by the $(1,0)$, $(1,2)$ helical components; the ratio of the helical (1,2) component to the next biggest component (2,0) varies between $\sim$ 5.9 and 10. The largest distortion from the pure $L = 2$ helical shape occurs at small HF current i.e. $I_h = 0.60 \times 10^5[A]$.

6.4 Stability window of the $(2,1)$ mode

Only the $(2,1)$ mode was considered in this stability analysis. We proceeded as in the fixed boundary case and went through the following steps :

• Determination of the $\mathcal{T}^{nores}_{m,n}$ and $\mathcal{T}_{m,n}$ sets

As the configuration has four equilibrium field periods, the (m_l, n_l) resonant modes in the $1 < q(s) < 2$ region have $n_l = 3, 5, 7, 9,..$ see Tab.(3.2). According to Tab.(3.6), the equilibrium terms coupling the (m_l, n_l) in question with the $(2,1)$ mode are $(m_e, N_{per}n_e = 4)$ for $m_e \geq 4$, $(m_e, N_{per}n_e = 8)$ for $m_e \geq 8$, $(m_e, N_{per}n_e = 12)$ for $m_e \geq 12$ etc.

The equilibrium Fourier components retained in the calculation, the $\sqrt{g}_{m_e,n_e}$ amplitudes and the perturbation components coupled with the (2,1) mode via the equilibrium components are given in Tab.(B.4) - see also Fig.6.7. The equilibrium was calculated with $I_h = 1.1 \times 10^5\,[A]$ and the $\sqrt{g}_{m_e,n_e}$ were evaluated on the plasma boundary. If we compare this table with Tab.(B.1) or Tab.(B.3) which are representative for the pure helical $L = 2$ fixed boundary case (no matter if N_{per} is different), we observe that the equilibrium components with odd n_e are no longer negligible. We can also see that there is a larger set of $\sqrt{g}_{m_e,n_e}$ amplitudes with $m_e \leq 3$ of the order $O(10^{-1})$ to $O(10^{-3})$. For lack of space, only 120 equilibrium components were represented in Tab.(B.4); those leading to couplings of $(2,1)$ with resonant (m_l, n_l) having $n_l = 7, 9, 11$ are not shown but have been retained in the calculations.

The consequence of having a boundary which is no longer purely $L = 2$ helical is that resonant modes can be coupled to the $(2,1)$ mode via a larger number of non negligible $(m_e, N_{per}n_e)$. However, these equilibrium components are still small compared with the dominant ones; the $\sqrt{g}_{m_e,1}$ amplitudes with $m_e \geq 4$ (involving couplings with the $(m_l, n_l = 3,5)$ resonant modes) are of the order $\sim O(10^{-5})$ compared with $O(10^{-1})$ for $\sqrt{g}_{0,0}$ or $O(10^{-2})$ for $\sqrt{g}_{1,0}$, $\sqrt{g}_{1,2}$, etc. The $\mathcal{T}^{nores}_{2,1}$ and $\mathcal{T}_{2,1}$ sets are then constructed as explained in Section 3.3.

• TERPSICHORE results

Fig.6.8 shows the evolution of the most unstable eigenvalue $\omega^{2\,nores}_{min}(\delta_i)$ calculated with the $\mathcal{T}^{nores}_{2,1}$ set. A stability window is obtained for values of the current in the HF coils between $1 \times 10^5\,[A] < I_h < 1.3 \times 10^5\,[A]$. For lower I_h values, the $(2,1)$ mode is the most unstable; at larger I_h, the $(1,1)$ mode becomes the main destabilizing factor. In the stability window, the q profiles are inverted and have low shear.

In order to verify that the $(2,1) \times (m_l, n_l)$ couplings with $m_l > n_l > 1$ are negligible, we selected three equilibria from the stability window with $I_h = 1.05$, 1.10 ,$1.20 \times 10^5\,[A]$ and

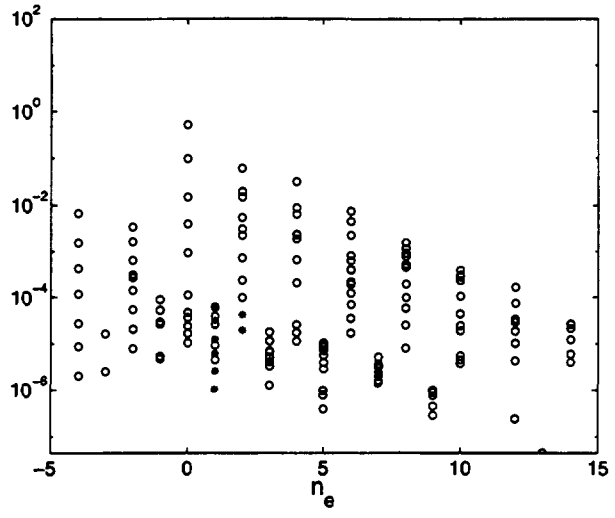

Figure 6.7: $\sqrt{g}_{m_e,n_e}$ *amplitudes in a free boundary equilibrium; the coil geometry and plasma parameters are described by Eq.(6.3) and Eq.(6.4) respectively and* $I_h = \pm 1.1 \times 10^5[A]$. *The x-axis corresponds to the* n_e *equilibrium mode number (not* $N_{per}n_e$*). The points marked with '*' represent the equilibrium components responsible for couplings between the* $(2,1)$ *mode and the* (m_l, n_l) *perturbation components with* $m_l > n_l > 1$ *(only the* $n_e \leq 2$ *i.e.* $n_l \leq 11$ *are shown). All other equilibrium components are marked with 'o'. See Tab.(B.4) for detailed informations.*

ran TERPSICHORE with the $\mathcal{T}_{2,1}$ set. The procedure followed was the same as in Section 5.2: the hierarchy of the unstable eigenvalues $\omega^2_{min}(I_h) < \omega^2_1(I_h) < \omega^2_2(I_h) < .. < 0$ was calculated for each of the I_h choosen and the associated (m_l, n_l) unstable modes were identified; some of the most unstable eigenvalues are given in Tab.(6.2). For each of these eigenvalues, the most important $W_p^{(m_{l1},n_{l1})\times(m_{l2},n_{l2})}$ couplings together with the $W_p^{(2,1)\times(m_l,n_l)}$ and $W_p^{(1,1)\times(m_l,n_l)}$ contributions to the potential energy (c.f. Section 5.2, Eq.(5.1)) are shown in Tab.(D3)

The particular case $I_h = 1.10 \times 10^5\,[A]$ and $\omega^2 = -5.832 \cdot 10^{-4}$ deserves attention because the value of $W_p^{max\,res}$ is quite large, i.e. -2.20×10^{-5}, which is about 20 times smaller than W_p^{max}. The perturbation components involved in the coupling are $(1,1)$ and $(4,3)$ - see Tab.(D3) ; the $(2,1) \times (m_l, n_l)$ couplings continue to have a negligible role in determining the value of the potential energy. In this case the stability window calculated with the $\mathcal{T}_{2,1}^{nores}$ set was not affected.

$I_h \cdot 10^5[A]$	q_{axis}	q_{min}	q_{edge}	ω^2	$(m_l, n_l)_\xi$		$(m_l, n_l)_\eta$		W_p^{max}	$W_p^{max\ res}$
1.050	1.437	1.273	1.273	-9.889E-04	4	3	4	3	-7.05E-04	-4.81E-08
				-7.314E-04	9	7	9	7	-6.80E-04	-2.37E-11
				-2.073E-04	7	5	7	5	-7.61E-04	-4.22E-09
				-1.097E-04	4	3	4	3	-3.45E-04	-3.09E-09
				-9.354E-05	7	5	7	5	-8.43E-04	-6.85E-09
1.100	1.386	1.202	1.202	-6.210E-04	11	9	11	9	-3.58E-04	-1.28E-08
				-5.832E-04	4	3	4	3	-5.15E-04	-2.20E-05
				-1.232E-04	4	3	4	3	-6.89E-04	-6.93E-07
				-9.435E-05	4	3	4	3	-6.32E-04	-4.09E-07
				-1.787E-05	4	3	4	3	-4.17E-04	-4.63E-07
1.200	1.286	1.065	1.065	-3.104E-04	6	5	6	5	-5.27E-04	-3.20E-08
				-1.979E-04	8	7	8	7	-2.20E-04	1.26E-09
				-1.877E-04	11	9	11	9	-6.48E-04	-5.41E-10
				-1.808E-04	6	5	6	5	-5.03E-04	-3.94E-08
				-1.145E-04	11	9	11	9	-6.47E-04	-1.99E-09

Table 6.2: *The unstable eigenvalues obtained when studying the* $(2,1)$ *mode with the* $\mathcal{T}_{2,1}$ *set for free boundary equilibria. The three values of* I_h *belong to the stability window showb in Fig.6.8. The plasma parameters and coil configuration characteristics are given by Eq.(6.3) and Eq.(6.4) - see also Fig.6.5. The perturbation components with the largest* ξ_{max} *and* η_{max} *amplitudes are given in the columns at the right of* ω^2*. The quantities* W_p^{max} *and* $W_p^{max\ res}$ *were defined by Eq.(5.1) and the paragraph that follows, respectively.*

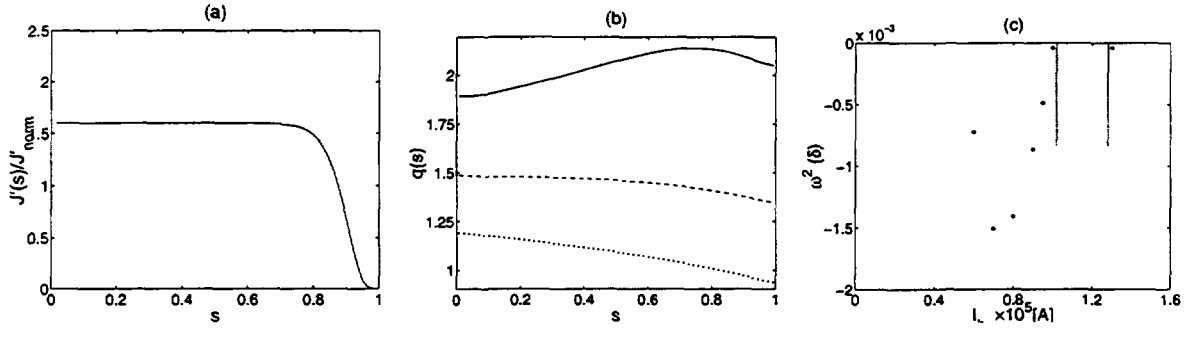

Figure 6.8: *Study of the (2,1) mode with the* $\mathcal{T}_{2,1}^{nores}$ *set:* **(a)** $J'(s)$ *profile,* **(b)** $q(s)$ *profile,* **(c)** $\omega^2_{min}(I_h)$ *for* $L = 2, N_{per} = 4, 1/\epsilon_c = 10$*,* $\beta = 1\%$*, pressure profile* pr^B *toroidal plasma current* $J = 1.27 \cdot 10^5[A]$ *with the toroidal current density of the form* $J'(s) \sim (1 - s^{20})^8$*. The coil geometry and plasma parameters are given by Eq.(6.3) and Eq.(6.4). The TF and VF coil currents are* $I_t = -1.6 \times 10^5[A]$*,* $I_{vl} = 1.0 \times 10^4[A]$ *and the inverse rotational transform profile is represented for* $I_h = 0.60 \times 10^5 A$ *(-),* $1.00 \times 10^5[A]$ *(- -) and* $I_h = 1.30 \times 10^5[A]$ *(·). The stable window is associated with values of* I_h *between* $1 \times 10^5[A]$ *and* $1.3 \times 10^5[A]$

6.5 Unexplored directions for future investigations

We have seen that the calculation of free boundary equilibrium sequences are more complex and require additional steps than in the correponding fixed boundary case. From a technical point of view, it is also more difficult to generate equilibrium sequences and study their global stability properties using a chaining procedure.
Nevertheless, the possibility of specifying independently the contribution of each coil system to the vacuum field introduces flexibility in the exploration of the parameter space. As an example, we may consider the relation between the boundary deformation and the inverse rotational transform profile: The systematic decrease of $q(s)$ when augmenting δ and keeping all other plasma parameters fixed was specific to the fixed boundary equilibrium sequences. We could not study equilibrium sequences with a (nearly) constant q profile and increasing δ's or conversely equilibria with a constant boundary deformation and different q profiles. We believe that to a certain extent, such a control of the inverse rotational transform profile is possible if the different equilibria are computed with suitable I_t, I_h and I_{vi} currents.

In order to show this we recalculate the equilibrium sequence described in Sections 6.4 and 6.5 with the same parameters except the current in the HF coils. We increase I_t from $-1.6 \times 10^5[A]$ to $-1.8 \cdot 10^5[A]$ which represents a variation of 12.5%; the larger toroidal field skews the magnetic field lines in the toroidal direction and in principle, the inverse rotational transform increases. The sequence of the most unstable eigenvalues resulting from this choice is shown in Fig.6.9 (c). The stability window corresponds to $1.15 \times 10^5\ [A] < I_h < 1.5 \cdot 10^5\ [A]$ and the q profiles delimiting this interval are displayed in Fig.6.9 (b). A larger current in the HF coils is needed to reach the stability window and this occurs at an increased $q_{edge} \simeq 1.4$ (in the preceding case $q_{edge} \simeq 1.33$ see Fig.6.8).

The stability window is apparently extended toward larger q_{edge} but the comparison of the two equilibrium sequences is complicated by the fact that the q_{axis} (at bigger I_t) are shifted toward larger values. We recall that a larger q_{axis} can also be obtained by decreasing the plasma current at constant I_t.
Additional variables enter the stability analysis and one cannot guess a priori to what extent the shape or size of the stability areas in the q_{axis}, q_{edge} plane will be changed compared with the fixed boundary cases. Only a systematic study may elucidate this point.

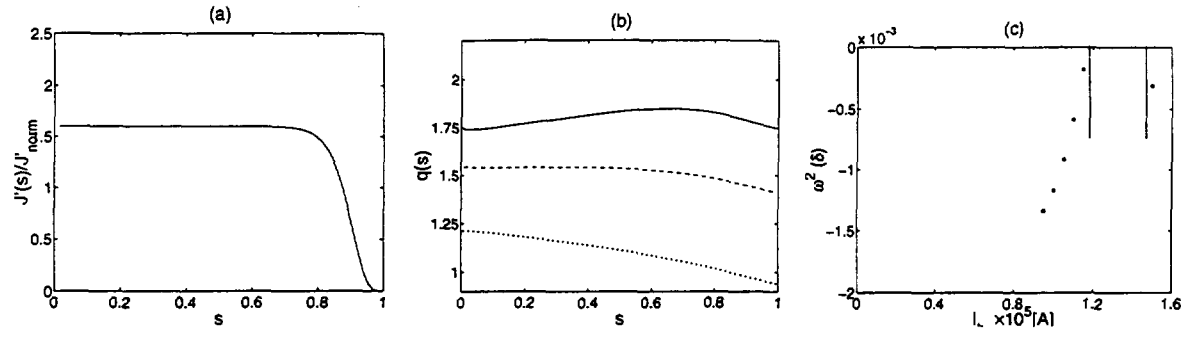

Figure 6.9: *The same as in Fig.6.8 but* $I_t = -1.8 \times 10^5[A]$. *The inverse rotational transform profile is represented for* $I_h = 0.95 \times 10^5\,[A]$ *(-),* $1.15 \times 10^5[A]$ *(- -), and* $I_h = 1.50 \times 10^5[A]$ *(·) and the stability window corresponds to* $1.15 \times 10^5[A] < I_h < 1.50 \times 10^5[A]$

6.6 Numerical aspects

The vacuum field was calculated on 21 vertical planes equally distributed along the toroidal direction for one equilibrium field period. The mesh was formed by 51 × 51 points in the R, Z directions; a refined mesh of 81 × 81 points was used to check the results. The coils were prescribed with 500 to 600 segments each and the rough estimation of q (c.f. Section 6.3) was based on 40 to 80 toroidal transits tracing the field lines.
The field line following routines of COILS were based on a standard Burlish-Stoer integration method [42]. The contribution of the TF, HF coils and of each pair of VF coils was calculated and given separately in the input file for NEMEC. One can vary the currents in the coils one by one when determining the equilibria without having to recalculate the vacuum field.
TERPSICHORE was run with 64 radial mesh points and 116 perturbation components.

Chapter 7

Summary and conclusions

In this work we have studied the global ideal MHD stability of plasmas with prescribed helical boundary deformation and nonzero toroidal plasma current. It has been demonstrated that these configurations are characterized by a spectrum of equilibrium Fourier components such that couplings between the $(m = n + 1, n)$, $n = 1, 2, 3$ perturbation modes studied and resonant (m_l, n_l) perturbation components with $m_l > n_l > n$ are negligible. It has been shown that a helical boundary deformation can stabilize the $(m = n + 1, n)$, $n = 1, 2, 3$ external global modes at values of q below 2.0 and β's of the order of 1-2%. Stabilization occurs for a great number of combinations of equilibrium parameters (i.e. the shape of the boundary deformation, number of field periods, aspect ratio, parabolic as well as nearly linear pressure profiles) and a large variety of current density profiles. When all these parameters are kept fixed and only the amplitude of the boundary deformation δ is varied, then stabilization occurs in an interval $[\delta_{min}, \delta_{max}]$. Weak toroidal plasma currents require more deformation for stabilization than larger currents. When two parameters are varied (i.e. δ and the amount of current at fixed current density profile) then an area of stability associated with the (m, n) mode appears in the (q_{axis}, q_{edge}) plane. The position, shape and size of this area depends on the other equilibrium parameters. At $\beta \simeq 1\%$, the common stability area associated with modes that have n = 1,2,3 in the region q_{axis}, $q_{edge} < 2.0$ is extremely reduced; taking into account modes with higher n's will possibly render this area equal to zero. The Mercier stability criterion is generally not satisfied and the absence of magnetic wells at strong δ (especially for the $L = 2$ configurations) indicates rather poor local stability properties. Ballooning modes are often unstable.

Our conclusions concerning the global stability results are more pessimistic than those formulated by M.I.Mikhailov and V.D.Shafranov c.f. Chap.1. An explanation may be found when considering the following. 1) We investigated 3D geometries; the couplings between perturbation components with different toroidal mode numbers are non negligible.

2) We considered cases with $\beta > 0$. 3) The stability diagrams presented in [19] were calculated with the assumption of a constant external rotational transform ι_h and a monotonic q profile. ι_h was added artificially to the tokamak rotational transform whereas in our study the variation of the rotational transform was due to the modification of the plasma boundary. We have also shown that our equilibrium sequences are not characterized by a uniform (constant with s) decrease of the inverse rotational transform. The q profiles in the stability windows and the q profiles at $\delta = \delta_{start}$ can be significantly different; these profiles are not necessarily monotonic.

A simple $L = 2$ stellarator-like configuration of coils was proposed for generating the external rotational transform for the free boundary calculations. We gave an example of a complete set of plasma and coil parameters which permitted the calculation of a sequence of free boundary equilibria which approximately recovered the desired boundary shapes and q profiles in the region of interest $1 < q < 2$. The parameter which was varied throughout the equilibrium sequence was the amount of current in the helical coils; when it was increased, a stability window for the (m, n) mode studied was found.

To arrive at these results, a general method for investigating the global MHD stability of 3D systems has been conceived. Due to toroidal periodicity, a partial coupling occurs between perturbation modes with different toroidal mode numbers. The method exploits the consequences of this coupling and aims at automatizing the investigation process. It consists of several steps which are either entirely executed or monitored by small programs and shell scripts:

- A chaining procedure computes sequences of equilibria by modifying iteratively one input parameter. Feedback contol can be implemented to ensure the constancy of some particular physical quantity(ies) (i.e. β) over the whole equilibrium sequence.
- The Fourier spectrum for an accurate representation of one equilibrium sequence in Boozer coordinates is identified. Depending on it and on the perturbation modes which are studied, the appropiate input data is generated for TERPSICHORE.
- A chaining mechanism can compute for each equilibrium the most unstable eigenvalue of the stability problem. A more complex procedure, consisting in the identification of the whole hierarchy of unstable eigenvalues with the associated perturbation modes and the most important couplings of perturbation components, has been implemented. The necessary modifications of input data for the stability code are performed with shell scripts, automatically, before each run.

Concerning the pertinence of future investigations we would like to point out some aspects which were not explored and which deserve further attention

• Wall stabilization was not exploited in the sense that during our whole study the wall was circular, axisymmetric and relatively far from the plasma boundary. One should reduce the plasma boundary-wall distance and, if necessary, impose a helical wall (shape conforming to avoid plasma-wall contacts).
• Free boundary calculations introduce additional parameters in the specification of the equilibrium and enlarge the investigation field. Through variation of the coil currents and/or coil geometry, the q profile can be modulated even if the plasma current and the amount of boundary deformation are kept constant. This was not the case in the previous fixed boundary calculations. The aim is to discover how to extend the stability areas toward large q_{edge} so as to maximize the chance of having a common SA for all the modes. Also, separating the variation of the boundary deformation from that of the q profile may help to get a clearer image of the stabilization process.
• Our fixed-boundary results concern mainly the $1 < q < 2$ region. The examination of the $q_{axis} > 2$, $q_{edge} < 2$ domain did not constitute an important focus of these studies partly because we detected equilibrium convergence and/or stability convergence problems. One should (re)consider this region carefully and systematically taking advantage of the wall stabilization effect and using free boundary calculations.
• Configurations with more complex helical boundary cross section may also be considered. For example, a $L = 2$ and/or $L = 3$ helical boundary deformations could be tested in combination with a $L = 1$ deformation driving a helical magnetic axis.
We conclude that in spite of the rather pessimistic results, numerous paths for future investigations remain open and available.

Finally, the investigation procedure designed in this thesis can be directly applied to the study of the global MHD properties of the proposed tokamak-torsatron hybrid EPEIUS, provided one adds the appropiate routines to the COILS code for specifying the modular twisted coils.

Bibliography

[1] J.Jacquinot, V.P.Bhatnagar, C.Gormezano and the JET Team, Plasma Phys. Controlled Fusion A **35**, 35, (1993)

[2] R.J.Hawryluk and the TFTR Team, "Review of recent D-T experiments from TFTR", Proceedings of the 15th International Conference on Plasma Physics and Controled Fusion Research, Seville 1994, (International Atomic Energy Vienna, 1995), **1**, 11

[3] M.Kikuchi and the JT60 Team, "Recent JT-60U results towards steady state operation of tokamaks", Proceedings of the 15th International Conference on Plasma Physics and Controled Fusion Research, Seville 1994, (International Atomic Energy Vienna, 1995), **1**, 31

[4] C.Beidler, G.Grieger, F.Herrnegger, E.Harmeyer, J.Kisslinger, W.Lotz, H.Massberg, P.Merkel, J.Nuhrenberg, F.Rau, J.Sapper, F.Sardei, R.Scardovelli, A.Schluter, H.Wobig, Fusion Technology, **17**, 148 (1990)

[5] C.Alejaldre and the TJ-II Team, Nuclear Fusion **17**, 131 (1990)

[6] A.Hyoshi, M.Fujiwara, 0.Motojima, N.Ohyabu ,K.Yamazaki, Fusion Technology, **17**, 169 (1990)

[7] K.Nishimura, K.Matsuoka, M.Fujimara, K.Yamazaki, J.Todoroki, T.Kamimura, T.Amano, H.Sanuki ,S.Okamura, M.Hosokawa, H.Yamada, S.Tanahashi, S.Kubo, Y.Takita ,T.Shoji, O.Kaneko, H.Iguchi, C.Takahashi, Fusion Technology, **17**, 86 (1990)

[8] S.F.Knowlton, R.F.Gandy, J.D.Hanson, G.J.Hartwell, H.Lin, J. Fusion Energy **12**, 261, (1993)

[9] A.Sykes,"The START spherical tokamak", Proceedings of the 15th International Conference on Plasma Physics and Controled Fusion Research, Seville 1994, Vol.1, IAEA (1995), 719

[10] Y.S.Hwang, M.Yamada, T.G.Jones, M.Ono, W.Choe, S.C.Jardin, E.Lo, A.Fredrisken, R.Nazikian, N.Pomphrey, S.Yoshikawa, "Exploration of low aspect ratio tokamak regimes in the CDX-U and TS-3 devices", Proceedings of the 15th International Conference on Plasma Physics and Controled Fusion Research, Seville 1994, Vol.1, IAEA (1995), 737

[11] P.E.Moroz, Phys. Plasmas **3**, No.8, 3055, (1996)

[12] P.E.Moroz - Fusion Technology **30**, 40, (1996)

[13] D.W.Ross,P.M.Valanju,H.He,W.H.Minner,P.E.Phillips,J.C.Wiley, A.J.Wootton,S.H.Zheng, Plasma Physics Reports, Vol.23, No.6, p.492 (1996)

[14] K.Miyamoto, *Plasma Physics for Nuclear Fusion*, MIT Press (1980)

[15] J.P.Freidberg, *Ideal Magnetohydrodynamics*, Plenum Press (1987)

[16] L.E.Zakharov in Plasma Physics and Controlled Nuclear Fusion Research 1986 (Proc. 11th Int. Conf. Kyoto, 1986), Vol.2, IAEA, Vienna (1987) 75

[17] K.Miyamoto, Nuclear Fusion **18**, 243, (1978)

[18] M.I.Mikhailov, V.D.Shafranov, Nuclear Fusion **30**, 413, (1990)

[19] M.I.Mikhailov, V.D.Shafranov, A.Subbotin, Proc. 22nd EPS Conf., Bournemouth, July 1995, Vol. 19C, Part III, p.193

[20] S.P.Hirshman, U.Schwenn, J.Nührenberg, J. Comput. Phys. **87**, 396, (1990)

[21] S.P.Hirshman, O.Betancourt, J. Comput. Phys. **96**, 99 (1991)

[22] S.P.Hirshman, J.C.Whitson - "Steepest-descent moment method for the three-dimensional magnetohydrodynamic equilibria" - *Phys. Fluids* **26**(12), pp.3553-3568, 1983

[23] W.A.Cooper,S.P.Hirshman, S.Merazzi, R.Gruber, Computer Physics Communications **72**, 1-13 (1992)

[24] A.H.Boozer - Phys. Fluids **23**, 904 (1980)

[25] J.Nührenberg, R.Zille in *Equilibrium and stability of low shear stellarators*, Theory of Fusion Plasmas, Proceedings of the joint Varenna-Lausanne Workshop, Varenna (1987) p.3-23

[26] J.P.Freidberg, *Ideal Magnetohydrodynamics*, Plenum Press, p.242 (1987)

[27] I.Bernstein, E.A.Frieman, M.D.Kruskal, R.M.Kulsrud, *Proc. R. Soc. London*, Ser. A **244**, 17

[28] G.Laval, C.Mercier, R.M.Pellat, Nucl.Fusion **5**, 156 (1965)

[29] J.P.Freidberg, *Ideal Magnetohydrodynamics*, Plenum Press, p.255 (1987)

[30] J.P.Freidberg, *Ideal Magnetohydrodynamics*, Plenum Press, p.259 (1987)

[31] W.A.Cooper, *Variational formulation of the linear MHD stability of 3D Plasmas with noninteracting hot electrons* - Plasma Physics and Controlled Fusion, Vol 34, No 6, p.1011-1036, (1992)

[32] D.B.Nelson, C.L.Hedrick, Nucl. Fusion **19**, 285 (1979)

[33] R.Gruber, S.Semenzato, F.Troyon, T.Tsunematu, W.K.Kerner, P.Merkel, W.Schneider, Computer Physics Communications **24**, pp.363-376 (1981)

[34] D.V.Anderson, W.A.Cooper, R.Gruber, S.Merazzi, U.Schwenn, Int. J. Supercomp. Appl. **4**, p.34 (1990)

[35] J.W.Connor,R.J.Hastie,J.B.Taylor, *High mode number stability of an axisymetric toroidal plasma* in Proc. R. Soc. Lond. A.**365**, p.1-17 (1979)

[36] R.L.Dewar, A.H.Glasser, *Ballooning mode spectrum in general toroidal systems*, Phys. Fluids **26**(10), pp.3038-3052, 1983

[37] B.R.Suydam - Proceedings of the Second United Nations International Conference on the Peaceful Uses of Atomic Energy, United Nations, Geneva **31** (1958) p.157

[38] J.P.Freidberg, *Ideal Magnetohydrodynamics*, Plenum Press, pp.296 (1987)

[39] W.A.Newcomb, Ann.Phys.(NY) **10**, (1960) 232

[40] C.Mercier, Nucl. Fusion **1**, p.47, (1960)

[41] K.Miyamoto, *Plasma Physics for Nuclear Fusion*, MIT Press, p. 40, (1980)

[42] W.H.Press, B.P.Flannery, S.A.Teukolsky, W.T.Vetterling, Numerical Recipes, Cambridge University Press, 563 (1986)

[43] P.Merkel, Journal of Comp. Phys. **66**, 83-98 (1986)

[44] S.P.Hirshman, W.I.van Rij, P.Merkel, Comp. Phys. Communications, **43**, 143 (1986)

Appendix A

Current density profiles

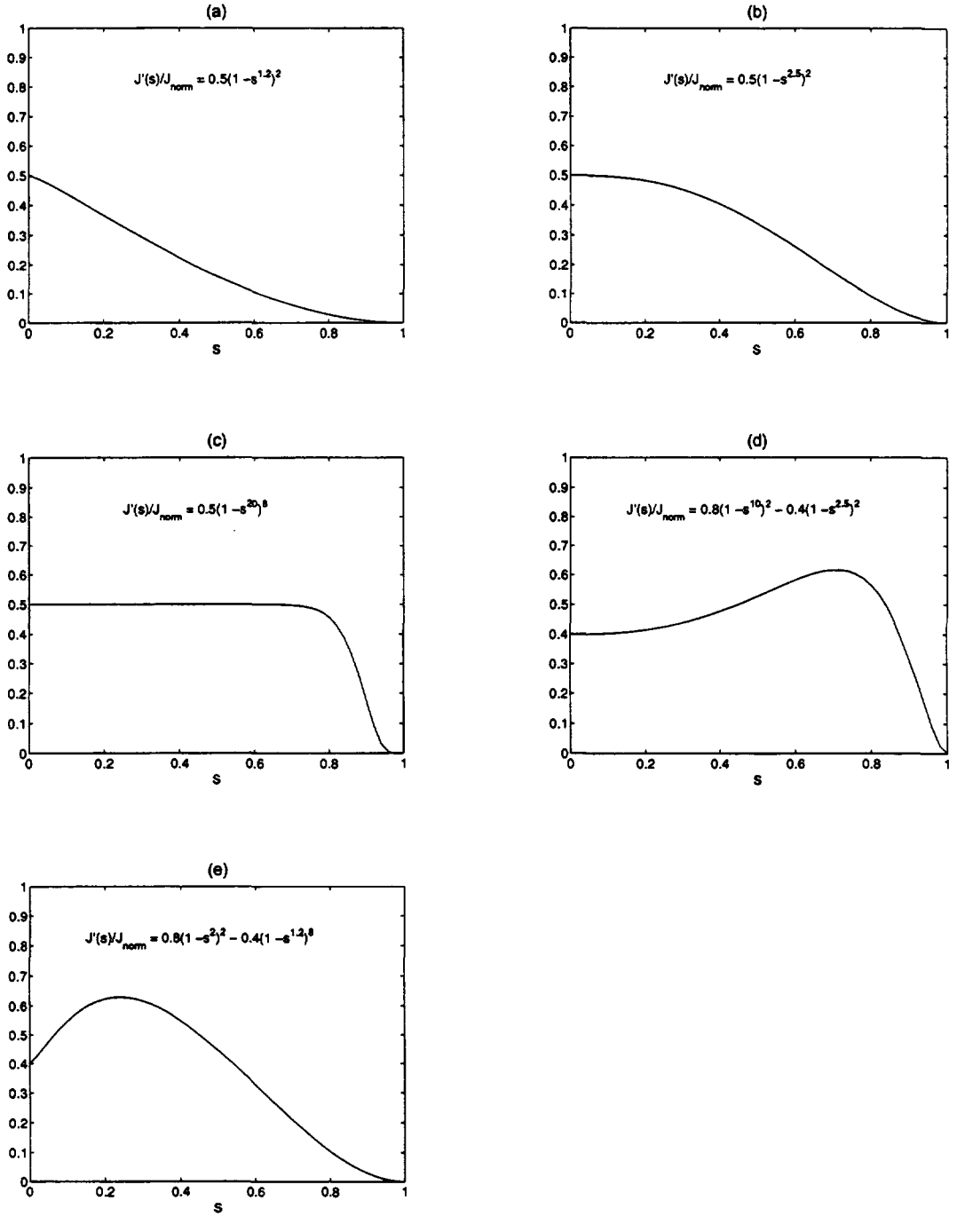

Figure A.1: Types of current density profiles used in the study

Appendix B

Amplitudes of equilibrium Fourier components and perturbation components involved in couplings with the (m, n) mode studied

i	$(m_e,\ n_e)$		$\sqrt{g}_{m_e,n_e}$	(m_{l1}, n_{l1})			(m_{l2}, n_{l2})		
1	0	0	-3.752E+00	2	1	*	2	1	*
2	0	1	6.515E-12	2	-4		2	6	
3	0	2	7.604E-03	2	-9		2	11	
4	0	3	3.935E-12	2	-14		2	16	
5	0	4	3.028E-04	2	-19		2	21	
6	0	6	6.333E-06	2	-29		2	31	
7	1	-2	6.675E-05	1	11		3	-9	
8	1	0	-1.543E+00	1	1		3	1	
9	1	1	2.219E-12	1	-4		3	6	
10	1	2	2.358E-01	1	-9		3	11	
11	1	3	9.899E-12	1	-14		3	16	
12	1	4	2.489E-03	1	-19		3	21	
13	1	6	-3.695E-05	1	-29		3	31	
14	2	-2	3.861E-05	0	-11		4	-9	
15	2	0	-2.639E-01	0	-1		4	1	
16	2	1	-4.538E-13	0	4		4	6	
17	2	2	-1.747E+00	0	9		4	11	
18	2	3	1.173E-12	0	14		4	16	
19	2	4	-6.433E-02	0	19		4	21	
20	2	6	-1.308E-03	0	29		4	31	
21	2	8	-8.261E-06	0	39		4	41	
22	3	-2	4.695E-06	1	-11		5	-9	
23	3	0	-4.614E-02	1	-1		5	1	
24	3	1	-7.344E-13	1	4		5	6	
25	3	2	-5.640E-01	1	9		5	11	
26	3	3	-5.185E-13	1	14		5	16	
27	3	4	2.751E-01	1	19		5	21	
28	3	6	1.565E-02	1	29		5	31	
29	3	8	4.628E-04	1	39		5	41	
30	3	10	7.339E-06	1	49		5	51	
31	4	-2	-1.366E-06	2	-11		6	-9	
32	4	0	-8.231E-03	2	-1		6	1	
33	4	1	-5.572E-14	2	4		6	6	
34	4	2	-1.380E-01	2	9		6	11	
35	4	3	2.128E-12	2	14		6	16	
36	4	4	-2.638E-01	2	19		6	21	
37	4	6	-6.301E-02	2	29		6	31	
38	4	8	-4.038E-03	2	39		6	41	
39	4	10	-1.487E-04	2	49		6	51	
40	4	12	-3.386E-06	2	59		6	61	
41	5	-2	-1.105E-06	3	-11		7	-9	
42	5	0	-1.483E-03	3	-1		7	1	
43	5	1	-6.987E-13	3	4		7	6	*
44	5	2	-3.009E-02	3	9		7	11	
45	5	3	1.019E-12	3	14		7	16	
46	5	4	-1.254E-01	3	19		7	21	
47	5	6	9.521E-02	3	29		7	31	
48	5	8	1.587E-02	3	39		7	41	
49	5	10	1.088E-03	3	49		7	51	
50	5	12	4.626E-05	3	59		7	61	
51	6	0	-2.690E-04	4	-1		8	1	
52	6	1	5.590E-14	4	4		8	6	*
53	6	2	-6.228E-03	4	9		8	11	
54	6	3	2.595E-13	4	14		8	16	
55	6	4	-3.877E-02	4	19		8	21	
56	6	6	-2.105E-02	4	29		8	31	
57	6	8	-2.975E-02	4	39		8	41	
58	6	10	-4.217E-03	4	49		8	51	
59	6	12	-3.019E-04	4	59		8	61	
60	7	0	-4.903E-05	5	-1		9	1	
61	7	1	8.967E-14	5	4	*	9	6	*
62	7	2	-1.252E-03	5	9		9	11	
63	7	3	-2.608E-13	5	14		9	16	
64	7	4	-9.970E-03	5	19		9	21	
65	7	6	-2.002E-02	5	29		9	31	
66	7	8	2.083E-02	5	39		9	41	
67	7	10	8.996E-03	5	49		9	51	
68	7	12	1.160E-03	5	59		9	61	
69	8	0	-8.953E-06	6	-1		10	1	
70	8	1	-3.369E-15	6	4	*	10	6	*
71	8	2	-2.478E-04	6	9		10	11	
72	8	3	-6.380E-14	6	14		10	16	
73	8	4	-2.334E-03	6	19		10	21	
74	8	6	-8.214E-03	6	29		10	31	
75	8	8	2.434E-03	6	39		10	41	
76	8	10	-9.490E-03	6	49		10	51	
77	8	12	-2.699E-03	6	59		10	61	
78	9	1	-2.755E-14	7	4	*	11	6	*
79	9	2	-4.877E-05	7	9		11	11	
80	9	3	-1.758E-15	7	14		11	16	
81	9	4	-5.173E-04	7	19		11	21	
82	9	6	-2.577E-03	7	29		11	31	
83	9	8	-1.788E-03	7	39		11	41	
84	9	10	2.842E-03	7	49		11	51	
85	9	12	3.596E-03	7	59		11	61	
86	10	1	-3.284E-14	8	4	*	12	6	*
87	10	2	-9.611E-06	8	9		12	11	*
88	10	3	-5.516E-15	8	14		12	16	
89	10	4	-1.111E-04	8	19		12	21	
90	10	6	-7.094E-04	8	29		12	31	
91	10	8	-1.256E-03	8	39		12	41	
92	10	10	1.326E-03	8	49		12	51	
93	10	12	-2.215E-03	8	59		12	61	
94	11	2	-1.905E-06	9	9		13	11	*
95	11	3	-1.062E-14	9	14		13	16	
96	11	4	-2.350E-05	9	19		13	21	
97	11	6	-1.815E-04	9	29		13	31	
98	11	8	-5.150E-04	9	39		13	41	
99	11	10	1.563E-04	9	49		13	51	
100	11	12	5.693E-05	9	59		13	61	
101	12	2	-3.811E-07	10	9	*	14	11	*
102	12	3	-2.297E-14	10	14		14	16	
103	12	4	-4.940E-06	10	19		14	21	
104	12	6	-4.448E-05	10	29		14	31	
105	12	8	-1.723E-04	10	39		14	41	
106	12	10	-9.017E-05	10	49		14	51	
107	12	12	2.631E-04	10	59		14	61	
108	13	2	-7.732E-08	11	9	*	15	11	*
109	13	3	-9.280E-15	11	14		15	16	
110	13	4	-1.040E-06	11	19		15	21	
111	13	6	-1.063E-05	11	29		15	31	
112	13	8	-5.184E-05	11	39		15	41	
113	13	10	-7.040E-05	11	49		15	51	
114	14	2	-1.604E-08	12	9	*	16	11	*
115	14	3	7.560E-15	12	14		16	16	
116	14	4	-2.204E-07	12	19		16	21	
117	14	6	-2.503E-06	12	29		16	31	
118	14	8	-1.464E-05	12	39		16	41	
119	15	2	-3.436E-09	13	9	*	17	11	*
120	15	3	-3.668E-15	13	14		17	16	*

Table B.1: Equilibrium Fourier components and their amplitudes together with the perturbation components which are coupled to the $(2,1)$ mode studied via Eq.(3.5). The indexes $_1$ and $_2$ are related to the "-" and "+" signs. The equilibrium is characterized by $L = 2$, $N_{per} = 5$, $1/\epsilon_c = 5$, $\beta = 1\%$, pressure profile pr^A, $J'/J'_{norm} = 0.90(1-s^{10})^2 - 0.40(1-s^{2.5})^2$ and $\delta_2 = 0.190$. m_l/n_l resonances with $m_l > n_l > 1$ are indicated by "*".

i	$(m_e,$	$n_e)$	$\sqrt{g}_{m_e,n_e}$	$(m_{l1},$	$n_{l1})$		$(m_{l2},$	$n_{l2})$		i	$(m_e,$	$n_e)$	$\sqrt{g}_{m_e,n_e}$	$(m_{l1},$	$n_{l1})$		$(m_{l2},$	$n_{l2})$	
1	0	0	-6.710E+00	2	1	*	2	1	*	61	5	7	-3.432E-03	3	27		7	29	
2	0	1	5.002E-02	2	-3		2	5		62	5	8	-4.854E-04	3	31		7	33	
3	0	2	4.190E-03	2	-7		2	9		63	5	9	1.461E-04	3	35		7	37	
4	0	3	-8.900E-05	2	-11		2	13		64	5	10	2.386E-05	3	39		7	41	
5	0	4	-1.746E-05	2	-15		2	17		65	5	11	-3.525E-06	3	43		7	45	
6	0	5	4.467E-06	2	-19		2	21		66	6	0	-1.531E-04	4	-1		8	1	
7	1	-4	-6.769E-06	1	17		3	-15		67	6	1	-3.586E-04	4	3	*	8	5	*
8	1	-3	-1.843E-05	1	13		3	-11		68	6	2	1.114E-03	4	7		8	9	
9	1	-2	6.783E-04	1	9		3	-7		69	6	3	-6.922E-03	4	11		8	13	
10	1	-1	4.265E-03	1	5		3	-3		70	6	4	-8.731E-04	4	15		8	17	
11	1	0	-1.524E+00	1	1		3	1		71	6	5	7.293E-03	4	19		8	21	
12	1	1	-6.727E-02	1	-3		3	5		72	6	6	-3.466E-03	4	23		8	25	
13	1	2	1.781E-02	1	-7		3	9		73	6	7	2.828E-03	4	27		8	29	
14	1	3	4.028E-04	1	-11		3	13		74	6	8	1.447E-03	4	31		8	33	
15	1	4	1.166E-03	1	-15		3	17		75	6	9	-2.869E-04	4	35		8	37	
16	1	5	6.326E-05	1	-19		3	21		76	6	10	-1.130E-04	4	39		8	41	
17	1	6	-9.201E-06	1	-23		3	25		77	6	11	9.327E-06	4	43		8	45	
18	2	-3	2.037E-06	0	-13		4	-11		78	7	0	-2.542E-05	5	-1		9	1	
19	2	-2	1.303E-04	0	-9		4	-7		79	7	1	-9.595E-05	5	3	*	9	5	*
20	2	-1	4.450E-04	0	-5		4	-3		80	7	2	1.618E-04	5	7		9	9	
21	2	0	-2.255E-01	0	-1		4	1		81	7	3	-1.291E-03	5	11		9	13	
22	2	1	-4.444E-02	0	3		4	5		82	7	4	-5.310E-04	5	15		9	17	
23	2	2	6.263E-01	0	7		4	9		83	7	5	2.401E-03	5	19		9	21	
24	2	3	3.649E-02	0	11		4	13		84	7	6	-2.960E-03	5	23		9	25	
25	2	4	-1.213E-02	0	15		4	17		85	7	7	6.723E-04	5	27		9	29	
26	2	5	-1.441E-03	0	19		4	21		86	7	8	-1.446E-03	5	31		9	33	
27	2	6	1.433E-04	0	23		4	25		87	7	9	1.615E-04	5	35		9	37	
28	2	7	2.307E-05	0	27		4	29		88	7	10	2.838E-04	5	39		9	41	
29	3	-2	2.086E-05	1	-9		5	-7		89	7	11	-3.762E-06	5	43		9	45	
30	3	-1	5.599E-05	1	-5		5	-3		90	7	12	-1.791E-05	5	47		9	49	
31	3	0	-3.548E-02	1	-1		5	1		91	8	0	-4.265E-06	6	-1		10	1	
32	3	1	-1.338E-02	1	3		5	5		92	8	1	-2.330E-05	6	3	*	10	5	*
33	3	2	1.691E-01	1	7		5	9		93	8	2	1.481E-05	6	7		10	9	*
34	3	3	-3.260E-01	1	11		5	13		94	8	3	-2.134E-04	6	11		10	13	
35	3	4	3.563E-02	1	15		5	17		95	8	4	-2.368E-04	6	15		10	17	
36	3	5	1.032E-02	1	19		5	21		96	8	5	5.599E-04	6	19		10	21	
37	3	6	-5.527E-04	1	23		5	25		97	8	6	-1.150E-03	6	23		10	25	
38	3	7	-2.678E-04	1	27		5	29		98	8	7	-2.024E-04	6	27		10	29	
39	3	8	3.168E-06	1	31		5	33		99	8	8	-2.709E-04	6	31		10	33	
40	3	9	4.696E-06	1	35		5	37		100	8	9	1.571E-04	6	35		10	37	
41	4	-2	5.218E-06	2	-9		6	-7		101	8	10	-3.290E-04	6	39		10	41	
42	4	-1	1.276E-05	2	-5		6	-3		102	8	11	-4.028E-05	6	43		10	45	
43	4	0	-5.723E-03	2	-1		6	1		103	8	12	4.069E-05	6	47		10	49	
44	4	1	-3.833E-03	2	3		6	5	*	104	8	13	5.311E-06	6	51		10	53	
45	4	2	3.522E-02	2	7		6	9		105	9	1	-5.261E-06	7	3		11	5	
46	4	3	-1.248E-01	2	11		6	13		106	9	2	-1.933E-06	7	7		11	9	*
47	4	4	2.064E-03	2	15		6	17		107	9	3	-3.117E-05	7	11		11	13	
48	4	5	-2.642E-02	2	19		6	21		108	9	4	-8.185E-05	7	15		11	17	
49	4	6	-3.902E-04	2	23		6	25		109	9	5	9.140E-05	7	19		11	21	
50	4	7	1.407E-03	2	27		6	29		110	9	6	-3.011E-04	7	23		11	25	
51	4	8	5.626E-05	2	31		6	33		111	9	7	-2.142E-04	7	27		11	29	
52	4	9	-3.626E-05	2	35		6	37		112	9	8	2.826E-04	7	31		11	33	
53	5	-1	3.290E-06	3	-5		7	-3		113	9	9	-1.223E-05	7	35		11	37	
54	5	0	-9.321E-04	3	-1		7	1		114	9	10	6.996E-05	7	39		11	41	
55	5	1	-1.204E-03	3	3		7	5	*	115	9	11	8.294E-05	7	43		11	45	
56	5	2	6.565E-03	3	7		7	9		116	9	12	-4.822E-05	7	47		11	49	
57	5	3	-3.236E-02	3	11		7	13		117	9	13	-1.684E-05	7	51		11	53	
58	5	4	-1.088E-03	3	15		7	17		118	9	14	4.195E-06	7	55		11	57	
59	5	5	1.007E-02	3	19		7	21		119	10	2	-1.675E-06	8	7	*	12	9	*
60	5	6	5.328E-03	3	23		7	25		120	10	3	-4.012E-06	8	11		12	13	

Table B.2: Equilibrium Fourier components and their amplitudes together with the perturbation components which are coupled to the $(2,1)$ mode studied via Eq.(3.5). The indexes $_1$ and $_2$ are related to the "-" and "+" signs. The equilibrium is characterized by mixed $L = 2$ and $L = 3$ boundary deformation ($\delta_2/\delta_3 = 2.5$), $N_{per} = 4$, $1/\epsilon_c = 10$, $\beta = 1\%$, pressure profile pr^B, $J'/J'_{norm} = 0.44(1 - s^{20})^8$ and $\delta_2 = 0.175$, $\delta_3 = 0.070$.

i	$(m_e,\ n_e)$		$\sqrt{g}_{m_e,n_e}$	(m_{l1}, n_{l1})			(m_{l2}, n_{l2})		
1	0	0	-7.815E+00	3	2	*	3	2	*
2	0	2	-3.989E-03	3	-8		3	12	
3	0	4	2.054E-05	3	-18		3	22	
4	1	-4	3.631E-07	2	22		4	-18	
5	1	-2	-3.030E-04	2	12		4	-8	
6	1	0	-1.838E+00	2	2		4	2	*
7	1	1	1.464E-12	2	-3		4	7	
8	1	2	1.099E-01	2	-8		4	12	
9	1	4	2.339E-03	2	-18		4	22	
10	1	6	1.657E-05	2	-28		4	32	
11	1	8	4.091E-08	2	-38		4	42	
12	2	-4	2.073E-06	1	22		5	-18	
13	2	-2	-5.043E-05	1	12		5	-8	
14	2	0	-2.412E-01	1	2		5	2	
15	2	1	-2.777E-13	1	-3		5	7	
16	2	2	-1.768E+00	1	-8		5	12	
17	2	4	-3.364E-02	1	-18		5	22	
18	2	6	-4.914E-04	1	-28		5	32	
19	2	8	-5.519E-06	1	-38		5	42	
20	3	-2	-8.852E-06	0	-12		6	-8	
21	3	0	-3.469E-02	0	-2		6	2	
22	3	1	1.220E-12	0	3		6	7	
23	3	2	-4.307E-01	0	8		6	12	
24	3	4	1.313E-01	0	18		6	22	
25	3	6	4.382E-03	0	28		6	32	
26	3	8	8.630E-05	0	38		6	42	
27	3	10	1.280E-06	0	48		6	52	
28	4	-2	-1.206E-06	1	-12		7	-8	
29	4	0	-5.194E-03	1	-2		7	2	
30	4	1	1.548E-12	1	3		7	7	
31	4	2	-8.405E-02	1	8		7	12	
32	4	4	-1.185E-01	1	18		7	22	
33	4	6	-1.636E-02	1	28		7	32	
34	4	8	-6.111E-04	1	38		7	42	
35	4	10	-1.438E-05	1	48		7	52	
36	4	12	-2.573E-07	1	58		7	62	
37	5	-2	-1.282E-07	2	-12		8	-8	
38	5	0	-7.952E-04	2	-2		8	2	
39	5	1	-6.205E-13	2	3		8	7	*
40	5	2	-1.540E-02	2	8		8	12	
41	5	4	-4.925E-02	2	18		8	22	
42	5	6	2.329E-02	2	28		8	32	
43	5	8	2.217E-03	2	38		8	42	
44	5	10	8.862E-05	2	48		8	52	
45	5	12	2.356E-06	2	58		8	62	
46	6	0	-1.236E-04	3	-2		9	2	
47	6	1	3.004E-13	3	3		9	7	*
48	6	2	-2.788E-03	3	8		9	12	
49	6	4	-1.362E-02	3	18		9	22	
50	6	6	-2.935E-03	3	28		9	32	
51	6	8	-3.890E-03	3	38		9	42	
52	6	10	-3.165E-04	3	48		9	52	
53	6	12	-1.322E-05	3	58		9	62	
54	6	14	-3.842E-07	3	68		9	72	
55	7	0	-1.948E-05	4	-2		10	2	
56	7	1	-7.511E-13	4	3	*	10	7	*
57	7	2	-5.102E-04	4	8		10	12	
58	7	4	-3.321E-03	4	18		10	22	
59	7	6	-4.002E-03	4	28		10	32	
60	7	8	2.315E-03	4	38		10	42	
61	7	10	6.311E-04	4	48		10	52	
62	7	12	4.676E-05	4	58		10	62	
63	7	14	2.014E-06	4	68		10	72	
64	8	0	-3.113E-06	5	-2		11	2	
65	8	1	-6.669E-13	5	3	*	11	7	*
66	8	2	-9.533E-05	5	8		11	12	
67	8	4	-7.735E-04	5	18		11	22	
68	8	6	-1.753E-03	5	28		11	32	
69	8	8	5.650E-04	5	38		11	42	
70	8	10	-5.948E-04	5	48		11	52	
71	8	12	-1.016E-04	5	58		11	62	
72	8	14	-7.078E-06	5	68		11	72	
73	9	0	-5.048E-07	6	-2		12	2	
74	9	1	-3.416E-13	6	3	*	12	7	*
75	9	2	-1.822E-05	6	8		12	12	
76	9	4	-1.768E-04	6	18		12	22	
77	9	6	-5.875E-04	6	28		12	32	
78	9	8	-1.479E-04	6	38		12	42	
79	9	10	1.030E-04	6	48		12	52	
80	9	12	1.232E-04	6	58		12	62	
81	9	14	1.636E-05	6	68		12	72	
82	9	16	1.091E-06	6	78		12	82	
83	10	0	-8.311E-08	7	-2		13	2	
84	10	1	-1.314E-13	7	3		13	7	*
85	10	2	-3.551E-06	7	8		13	12	*
86	10	4	-4.000E-05	7	18		13	22	
87	10	6	-1.739E-04	7	28		13	32	
88	10	8	-1.623E-04	7	38		13	42	
89	10	10	1.045E-04	7	48		13	52	
90	10	12	-6.059E-05	7	58		13	62	
91	10	14	-2.339E-05	7	68		13	72	
92	10	16	-2.642E-06	7	78		13	82	
93	11	2	-7.016E-07	8	8		14	12	*
94	11	4	-8.970E-06	8	18		14	22	
95	11	6	-4.777E-05	8	28		14	32	
96	11	8	-7.909E-05	8	38		14	42	
97	11	10	2.057E-05	8	48		14	52	
98	11	12	-1.063E-05	8	58		14	62	
99	11	14	1.755E-05	8	68		14	72	
100	11	16	4.246E-06	8	78		14	82	
101	12	2	-1.398E-07	9	8	*	15	12	*
102	12	4	-1.994E-06	9	18		15	22	
103	12	6	-1.249E-05	9	28		15	32	
104	12	8	-2.988E-05	9	38		15	42	
105	12	10	-6.578E-06	9	48		15	52	
106	12	12	8.341E-06	9	58		15	62	
107	13	2	-2.797E-08	10	8	*	16	12	*
108	13	4	-4.400E-07	10	18		16	22	
109	13	6	-3.153E-06	10	28		16	32	
110	13	8	-9.878E-06	10	38		16	42	
111	13	10	-7.384E-06	10	48		16	52	
112	14	2	-5.598E-09	11	8	*	17	12	*
113	14	4	-9.644E-08	11	18		17	22	
114	14	6	-7.757E-07	11	28		17	32	
115	14	8	-3.004E-06	11	38		17	42	
116	15	2	-1.118E-09	12	8	*	18	12	*
117	15	4	-2.103E-08	12	18		18	22	
118	16	2	-2.228E-10	13	8	*	19	12	*
119	16	4	-4.570E-09	13	18		19	22	
120	17	2	-4.430E-11	14	8	*	20	12	*

Table B.3: Equilibrium Fourier components and their amplitudes together with the perturbation components which are coupled to the $(2,1)$ mode studied via Eq.(3.5). The indexes $_1$ and $_2$ are related to the "-" and "+" signs. The equilibrium is characterized by $L = 2$, $N_{per} = 5$, $1/\epsilon_c = 10$, $\beta = 1\%$, pressure profile pr^A, $J'/J'_{norm} = 0.35(1 - s^{20})^8$ and $\delta_2 = 0.265$. The mode studied is the $(3,2)$.

i	$(m_e,\ n_e)$		$\sqrt{g}_{m_e,n_e}$	(m_{l1}, n_{l1})			(m_{l2}, n_{l2})			i	$(m_e,\ n_e)$		$\sqrt{g}_{m_e,n_e}$	(m_{l1}, n_{l1})			(m_{l2}, n_{l2})		
1	0	0	-5.104E-01	2	1	*	2	1	*	61	4	1	-3.897E-05	2	3		6	5	*
2	0	1	4.568E-06	2	-3		2	5		62	4	2	-5.515E-03	2	7		6	9	
3	0	2	-3.097E-03	2	-7		2	9		63	4	3	4.136E-06	2	11		6	13	
4	0	3	-1.792E-05	2	-11		2	13		64	4	4	-2.349E-03	2	15		6	17	
5	0	4	3.160E-02	2	-15		2	17		65	4	5	-5.687E-06	2	19		6	21	
6	0	5	-1.040E-05	2	-19		2	21		66	4	6	3.843E-04	2	23		6	25	
7	0	6	1.905E-04	2	-23		2	25		67	4	7	3.660E-06	2	27		6	29	
8	0	7	3.247E-06	2	-27		2	29		68	4	8	9.001E-04	2	31		6	33	
9	0	8	-7.625E-04	2	-31		2	33		69	4	9	2.850E-07	2	35		6	37	
10	0	10	4.545E-06	2	-39		2	41		70	4	10	2.292E-04	2	39		6	41	
11	1	-6	8.526E-05	1	25		3	-23		71	4	12	-3.366E-05	2	47		6	49	
12	1	-4	6.799E-03	1	17		3	-15		72	5	-6	2.370E-05	3	-25		7	-23	
13	1	-3	-1.644E-05	1	13		3	-11		73	5	-4	2.699E-05	3	-17		7	-15	
14	1	-2	2.669E-04	1	9		3	-7		74	5	-2	3.083E-04	3	-9		7	-7	
15	1	-1	5.259E-05	1	5		3	-3		75	5	-1	-4.823E-06	3	-5		7	-3	
16	1	0	-9.532E-02	1	1		3	1		76	5	0	-1.133E-04	3	-1		7	1	
17	1	1	9.353E-06	1	-3		3	5		77	5	1	-6.449E-05	3	3		7	5	*
18	1	2	1.509E-02	1	-7		3	9		78	5	2	-2.232E-03	3	7		7	9	
19	1	3	-6.686E-06	1	-11		3	13		79	5	3	-7.054E-06	3	11		7	13	
20	1	4	8.889E-03	1	-15		3	17		80	5	4	-1.855E-03	3	15		7	17	
21	1	5	-3.947E-06	1	-19		3	21		81	5	5	7.173E-06	3	19		7	21	
22	1	6	-2.188E-03	1	-23		3	25		82	5	6	8.057E-04	3	23		7	25	
23	1	7	5.187E-06	1	-27		3	29		83	5	7	-1.568E-06	3	27		7	29	
24	1	8	-4.460E-04	1	-31		3	33		84	5	8	1.161E-03	3	31		7	33	
25	1	10	1.900E-05	1	-39		3	41		85	5	9	8.942E-07	3	35		7	37	
26	2	-6	-1.376E-06	0	-25		4	-23		86	5	10	-3.048E-04	3	39		7	41	
27	2	-4	1.517E-03	0	-17		4	-15		87	5	12	-1.652E-04	3	47		7	49	
28	2	-3	2.498E-06	0	-13		4	-11		88	5	14	2.615E-05	3	55		7	57	
29	2	-2	3.407E-03	0	-9		4	-7		89	6	-4	8.692E-06	4	-17		8	-15	
30	2	-1	2.958E-05	0	-5		4	-3		90	6	-2	1.402E-04	4	-9		8	-7	
31	2	0	-1.481E-02	0	-1		4	1		91	6	-1	-5.443E-06	4	-5		8	-3	
32	2	1	2.606E-05	0	3		4	5		92	6	0	-4.702E-05	4	-1		8	1	
33	2	2	-6.017E-02	0	7		4	9		93	6	1	-3.158E-05	4	3	*	8	5	*
34	2	3	-5.285E-06	0	11		4	13		94	6	2	-7.337E-04	4	7		8	9	
35	2	4	-2.280E-03	0	15		4	17		95	6	3	-1.167E-05	4	11		8	13	
36	2	5	-8.654E-06	0	19		4	21		96	6	4	-6.467E-04	4	15		8	17	
37	2	6	7.375E-03	0	23		4	25		97	6	5	7.426E-06	4	19		8	21	
38	2	7	-1.402E-06	0	27		4	29		98	6	6	6.228E-04	4	23		8	25	
39	2	8	5.144E-04	0	31		4	33		99	6	7	-3.361E-06	4	27		8	29	
40	2	10	-2.754E-04	0	39		4	41		100	6	8	4.927E-04	4	31		8	33	
41	3	-6	1.135E-05	1	-25		5	-23		101	6	9	9.029E-07	4	35		8	37	
42	3	-4	4.274E-04	1	-17		5	-15		102	6	10	-1.068E-04	4	39		8	41	
43	3	-2	1.625E-03	1	-9		5	-7		103	6	12	-2.417E-07	4	47		8	49	
44	3	-1	-8.840E-05	1	-5		5	-3		104	6	14	2.116E-05	4	55		8	57	
45	3	0	-3.936E-03	1	-1		5	1		105	7	-4	2.074E-06	5	-17		9	-15	
46	3	1	6.070E-05	1	3		5	5		106	7	-2	5.452E-05	5	-9		9	-7	
47	3	2	-1.959E-02	1	7		5	9		107	7	0	-3.664E-05	5	-1		9	1	
48	3	3	5.175E-06	1	11		5	13		108	7	1	-1.247E-05	5	3	*	9	5	*
49	3	4	6.473E-03	1	15		5	17		109	7	2	-2.366E-04	5	7		9	9	
50	3	5	-9.421E-06	1	19		5	21		110	7	3	-1.136E-05	5	11		9	13	
51	3	6	4.457E-03	1	23		5	25		111	7	4	-2.059E-04	5	15		9	17	
52	3	7	1.610E-06	1	27		5	29		112	7	5	7.729E-07	5	19		9	21	
53	3	8	-1.530E-03	1	31		5	33		113	7	6	3.966E-04	5	23		9	25	
54	3	10	-3.849E-04	1	39		5	41		114	7	7	1.981E-06	5	27		9	29	
55	3	12	7.522E-05	1	47		5	49		115	7	8	1.923E-04	5	31		9	33	
56	4	-6	2.069E-05	2	-25		6	-23		116	7	9	1.011E-06	5	35		9	37	
57	4	-4	1.188E-04	2	-17		6	-15		117	7	10	4.271E-05	5	39		9	41	
58	4	-2	6.306E-04	2	-9		6	-7		118	7	12	-2.935E-05	5	47		9	49	
59	4	-1	-2.676E-05	2	-5		6	-3		119	7	14	-2.623E-05	5	55		9	57	
60	4	0	-9.321E-04	2	-1		6	1		120	8	-2	2.078E-05	6	-9		10	-7	

Table B.4: Free boundary calculated (with NEMEC) equilibrium Fourier components and their amplitudes together with the perturbation components which are coupled to the $(2,1)$ mode studied via Eq.(3.5). The coils geometry and plasma parameters are given by Eq.(6.3) and Eq.(6.4).

Appendix C

The chaining procedure

When calculating an equilibrium sequence and testing its global stability one varies essentially a restricted number of input parameters. The bulk of the calculation is done with VMEC and TERPSICHORE and a certain number of operations, always the same, have to be performed before and after each run. The aim of the chaining procedure is to automatize these repetitive tasks; depending on their complexity, the chaining process is monitored by one or more shell scripts written in Korn or Bourne shell language. There are scripts for equilibrium calculations, for stability analysis and for the verification procedures (c.f. Section 4.3).
At each step of the sequence, the script enters the appropiate NQS queue, executes some pre-run operations, runs the equilibrium or stability code only once, does some final job and exits. The script reenters the queue automatically till the end of the sequence is reached. Compared with the case in which the whole chain is processed during a unique submission in a much longer (CPU time) NQS queue, this procedure offers two main advantages:
1) it enables the script to run in shorter queues which are less overloaded than the longer queues. A single run for both VMEC and TERPSICHORE (for our configurations) takes between 100 $\sim$ 200 CPUs.
2) it is more flexible because one can intefere at each step in the chaining process and make appropiate modifications when they are needed.
A brief description of the main tasks executed with these scripts is given below.

A. Chaining the equilibrium calculations
The first task of the chaining script is to find how many steps were already executed and to determine the new δ_i input parameter according to Eq.(4.1). The appropiate values for the $R_{m_c^v,n_c^v}(s=1)$ and $Z_{m_c^v,n_c^v}(s=1)$ Fourier amplitudes that specify the new boundary shape - see Eq.(3.1) to Eq.(3.4), are replaced in the VMEC input file using non-interactive editing utilities like *awk* and *sed*. At the same time, in order to keep β constant, the p_0

coefficient (Eq.(3.9) or Eq.(3.10)) is also modified as is explained in the paragraph that follows Eq.(5.5).
After running VMEC, the actual value of β is compared with the desired value; if the difference is larger than a prescribed limit, the next job will calculate an equilibrium with the same δ_i and a new interpolated p_0.

B. Chaining the stability calculations

The script determines how many stability runs were already executed and identifies the equilibrium data files together with the input files containing the appropiate $\mathcal{T}_{m,n}^{nores}$ sets. Because TERPSICHORE uses an inverse vector iteration procedure to calculate $\omega_{min}^{2\,nores}(\delta_i)$, the initial guess of the most unstable eigenvalue is important. The guess is made on the basis of the previous calculated $\omega_{min}(\delta_{i-1})$, $\omega_{min}(\delta_{i-2})$, .. values using an extrapolation technique.

Data related to the program execution like the number of iterations, the value of the residual forces F_R, F_Z and F_λ (c.f. Eq.(2.11)), the number of Jacobian resets, etc, for VMEC or the relative errors of the equilibrium reconstruction in Boozer coordinates (c.f.Eq.(4.4) and paragraph that follows), etc, for TERPSICHORE, together with some representative physical quantities i.e. β, $\omega_{min}^{2\,nores}(\delta_i)$, etc are gathered in tables after each run. These tables offer a rapid view of the evolution of the chaining process; if something unexpected occurs, they permit an easy diagnosis of the problem and appropiate measures can be readily taken.

C. Automatizing the verification procedure

As explained in Section 4.3, applying this procedure means running TERPSICHORE with the $\mathcal{T}_{m,n}$ set over two loops. The first loop deal with those δ_i 's for which the (m,n) mode is stable when studied with the $\mathcal{T}_{m,n}^{nores}$ set. In the second loop, the hierarchy of unstable eigenvalues $\omega_{min}^2(\delta_i) < \omega_1^2(\delta_i) < \omega_2^2(\delta_i) < .. < 0$ is found for each of the preceeding δ_i and the corresponding unstable modes (m_j, n_j) are identified - Fig.C.1 illustrates a fictious example. Before starting the execution of TERPSICHORE, the script determines the appropiate equilibrium data files, estimates the initial guess value for $\omega_j^2(\delta_i)$ - let us call it $\omega_j^{2\,guess}(\delta_i\ )$ and does the necessary changes in the input files.
When the TERPSICHORE calculates an eigenvalue, it also indicates how many eigenvalues are smaller (more unstable) than the one which was found. At the beginning of each inner loop, the choice of $\omega_{min}^{2\,guess}(\delta_i\ )$ is simple: it should be taken sufficiently low to be sure that the eigenvalue found by the solver is indeed $\omega_{min}^2(\delta_i\ )$ and not $\omega_1^2(\delta_i\ )$ or other greater value.
Suppose that the eigenvalues $\omega_{min}^2(\delta_i) < .. < \omega_{j-1}^2(\delta_i)$ have already been found, the next

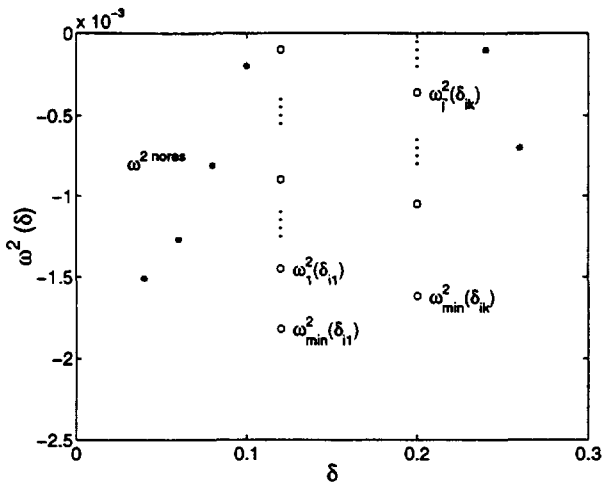

Figure C.1: *An ilustration of the most unstable eigenvalues ω^2_{min} obtained when studying the (m,n) mode with the $\mathcal{T}^{nores}_{m,n}$ set are labelled with "*". Some eigenvalues (for two values of δ) from the $\omega^2_{min}(\delta_i) < \omega^2_1(\delta_i) < \omega^2_2(\delta_i) < .. < 0$ ensemble obtained when studying the (m,n) mode with the $\mathcal{T}_{m,n}$ set are represented with "o". The numerical values are purely fictious.*

guess $\omega_j^{2\ guess}(\delta_i)$ is chosen larger than $\omega^2_{j-1}(\delta_i)$. It is possible that
1) if $\omega_j^{2\ guess}(\delta_i\ )$ is too high, the calculated eigenvalue may correspond to ω^2_{j+1} or even worse to ω^2_{j+2}, etc
2) if $\omega_j^{2\ guess}(\delta_i\ )$ is too low, we may recompute ω^2_{j-1}
If one of these two cases occurs, then new trials are made until the calculated eigenvalue corresponds to $\omega^2_j(\delta_i)$. This may require a single run or more. Let us imagine the following situation: case 1) occurs and the eigenvalue found corresponds to ω^2_{j+1}. The new $\omega_j^{2\ guess}(\delta_i)$ must be smaller than the former one but the correction (decrease) should not be too large because $\omega^2_{j-1}(\delta_i)$ may be found again; the correction should also not be too weak to recompute ω^2_{j+1}. If these last two situations occur, several scenarios can again be imagined but the worst is that where the succesive guesses lead to calculate eigenvalues which oscillates between $\omega^2_{j-1}(\delta_i)$ and $\omega^2_{j+1}(\delta_i)$. Therefore the complete history of guesses and results should be examined within the script in order to detect such situations and take appropiate measures.
Using a trial and error technique it was finally possible to write a script which, when submitted, manages to determine the complete $\omega^2_{min}(\delta_i) < \omega^2_1(\delta_i) < \omega^2_2(\delta_i) < .. < 0$ hierarcy in a number of runs rarely exceeding $3\times$ number of eigenvalues in the hierarchy.

Appendix D

Contribution to the potential energy of the couplings between the (m, n) mode studied and the (m_l, n_l) perturbation components with $m_l/n_l > 1$ resonances.

δ	$(m_{l1}, n_{l1}) \times (m_{l2}, n_{l2})$ couplings				$W_p^{(m_{l1},n_{l1})\times(m_{l2},n_{l2})}$			
0.190	(11,9) × (11,9)	(11,9) × (12,9)	(9,−1) × (11,9)	(12,9) × (12,9)	-3.89E-04	-1.94E-04	-1.06E-04	7.64E-05
	(2,1) × (5,4)	(2,1) × (6,4)	(1,1) × (5,4)	(1,1) × (6,4)	-4.66E-19	4.13E-19	1.40E-18	-1.30E-18
	(2,1) × (10,9)	(2,1) × (11,9)	(1,1) × (10,9)	(1,1) × (11,9)	-5.68E-17	-3.06E-15	1.27E-16	-6.37E-15
	(2,1) × (12,11)	(2,1) × (13,11)	(1,1) × (12,11)	(1,1) × (13,11)	6.63E-20	4.46E-19	2.35E-19	-3.88E-20
	(14,11) × (14,11)	(13,11) × (14,11)	(14,11) × (15,11)	(12,1) × (14,11)	-2.43E-04	-2.21E-04	-1.87E-04	-1.79E-04
	(2,1) × (5,4)	(2,1) × (6,4)	(1,1) × (5,4)	(1,1) × (6,4)	-1.69E-23	1.69E-23	2.52E-22	-2.46E-22
	(2,1) × (10,9)	(2,1) × (11,9)	(1,1) × (10,9)	(1,1) × (11,9)	3.34E-21	-5.51E-19	4.20E-21	-7.61E-19
	(2,1) × (12,11)	(2,1) × (13,11)	(1,1) × (12,11)	(1,1) × (13,11)	2.38E-17	2.78E-16	8.13E-17	1.66E-16
	(5,4) × (5,4)	(5,4) × (6,4)	(4,4) × (5,4)	(6,4) × (6,4)	-1.07E-04	-8.03E-05	-4.75E-05	4.13E-05
	(2,1) × (5,4)	(2,1) × (6,4)	(1,1) × (5,4)	(1,1) × (6,4)	-1.04E-15	-1.58E-16	-9.86E-16	1.01E-16
	(2,1) × (10,9)	(2,1) × (11,9)	(1,1) × (10,9)	(1,1) × (11,9)	-3.56E-20	-8.86E-21	1.87E-20	-4.22E-21
	(2,1) × (12,11)	(2,1) × (13,11)	(1,1) × (12,11)	(1,1) × (13,11)	1.04E-22	2.93E-21	3.43E-21	2.90E-22
	(7,6) × (8,6)	(8,6) × (9,6)	(8,6) × (8,6)	(7,6) × (7,6)	-8.43E-05	-7.22E-05	4.98E-05	4.33E-05
	(2,1) × (5,4)	(2,1) × (6,4)	(1,1) × (5,4)	(1,1) × (6,4)	-6.19E-17	-6.63E-18	4.46E-17	-1.45E-18
	(2,1) × (10,9)	(2,1) × (11,9)	(1,1) × (10,9)	(1,1) × (11,9)	-1.68E-21	-1.75E-22	7.39E-22	-5.07E-23
	(2,1) × (12,11)	(2,1) × (13,11)	(1,1) × (12,11)	(1,1) × (13,11)	-1.01E-17	-3.40E-18	2.56E-18	-8.16E-18
0.200	(7,6) × (7,6)	(7,6) × (8,6)	(8,6) × (8,6)	(6,6) × (7,6)	-2.76E-04	-8.94E-05	4.06E-05	-2.47E-05
	(2,1) × (5,4)	(2,1) × (6,4)	(1,1) × (5,4)	(1,1) × (6,4)	1.06E-19	-1.45E-20	-8.65E-20	2.34E-20
	(2,1) × (10,9)	(2,1) × (11,9)	(1,1) × (10,9)	(1,1) × (11,9)	-1.94E-17	-1.56E-17	2.23E-18	-7.98E-17
	(2,1) × (12,11)	(2,1) × (13,11)	(1,1) × (12,11)	(1,1) × (13,11)	-4.18E-19	3.16E-20	7.83E-20	3.14E-20
	(9,−1) × (11,9)	(10,9) × (11,9)	(11,9) × (12,9)	(11,9) × (11,9)	-1.30E-04	-1.21E-04	-1.10E-04	-8.14E-05
	(2,1) × (5,4)	(2,1) × (6,4)	(1,1) × (5,4)	(1,1) × (6,4)	4.07E-19	-2.29E-19	-1.64E-18	1.02E-18
	(2,1) × (10,9)	(2,1) × (11,9)	(1,1) × (10,9)	(1,1) × (11,9)	-3.74E-16	-4.05E-16	3.95E-16	-1.30E-13
	(2,1) × (12,11)	(2,1) × (13,11)	(1,1) × (12,11)	(1,1) × (13,11)	7.28E-20	1.35E-18	-7.05E-19	2.87E-17
	(13,11) × (14,11)	(11,1) × (13,11)	(14,11) × (14,11)	(11,1) × (11,1)	-5.73E-05	-5.67E-05	3.06E-05	2.76E-05
	(2,1) × (5,4)	(2,1) × (6,4)	(1,1) × (5,4)	(1,1) × (6,4)	3.84E-19	2.29E-20	-2.03E-19	2.55E-20
	(2,1) × (10,9)	(2,1) × (11,9)	(1,1) × (10,9)	(1,1) × (11,9)	-1.11E-22	1.06E-23	6.09E-23	1.51E-22
	(2,1) × (12,11)	(2,1) × (13,11)	(1,1) × (12,11)	(1,1) × (13,11)	-2.49E-17	-2.12E-15	7.11E-16	-1.38E-17
	(5,4) × (6,4)	(4,4) × (5,4)	(6,4) × (6,4)	(4,4) × (4,4)	-3.52E-05	-3.44E-05	1.86E-05	1.71E-05
	(2,1) × (5,4)	(2,1) × (6,4)	(1,1) × (5,4)	(1,1) × (6,4)	-1.18E-15	-1.28E-16	-4.94E-15	4.87E-17
	(2,1) × (10,9)	(2,1) × (11,9)	(1,1) × (10,9)	(1,1) × (11,9)	-3.54E-20	1.06E-21	1.44E-20	7.99E-21
	(2,1) × (12,11)	(2,1) × (13,11)	(1,1) × (12,11)	(1,1) × (13,11)	-8.69E-21	-7.31E-20	-5.25E-21	4.46E-21
0.220	(12,11) × (12,11)	(11,11) × (12,11)	(10,1) × (12,11)	(12,11) × (13,11)	-1.70E-04	-2.93E-05	-2.72E-05	-2.68E-05
	(2,1) × (5,4)	(2,1) × (6,4)	(1,1) × (5,4)	(1,1) × (6,4)	-3.65E-21	-1.51E-22	6.56E-21	5.65E-23
	(2,1) × (10,9)	(2,1) × (11,9)	(1,1) × (10,9)	(1,1) × (11,9)	-9.07E-20	-2.26E-22	1.57E-18	-1.07E-20
	(2,1) × (12,11)	(2,1) × (13,11)	(1,1) × (12,11)	(1,1) × (13,11)	-9.02E-15	5.50E-16	8.47E-15	5.40E-26
	(10,9) × (10,9)	(10,9) × (11,9)	(8,−1) × (10,9)	(11,9) × (11,9)	-4.42E-05	-1.55E-05	-1.28E-05	8.48E-06
	(2,1) × (5,4)	(2,1) × (6,4)	(1,1) × (5,4)	(1,1) × (6,4)	-1.45E-19	1.33E-19	7.63E-19	-7.35E-19
	(2,1) × (10,9)	(2,1) × (11,9)	(1,1) × (10,9)	(1,1) × (11,9)	-5.52E-16	1.88E-19	-3.49E-14	7.50E-18
	(2,1) × (12,11)	(2,1) × (13,11)	(1,1) × (12,11)	(1,1) × (13,11)	-4.34E-20	-3.50E-21	-4.98E-16	9.90E-18

Table D.1: *For each unstable eigenvalue from Tab.(5.1) a set of four block rows with detailed information is presented. The first row of each block shows the four most important coupling contributions (components and amplitudes) to the potential energy. The following three rows in each block give the contribution to the potential energy of the* $(m,1) \times (m_l, n_l)$ *with* $m = 2,1$ *couplings;* (m_l, n_l) *is either the dominant unstable component or is coupled to* $(2,1)$ *via one of the three strongest equilibrium components marked with "*" in Tab.(B.1)*

δ	$(m_{l1},n_{l1})\times(m_{l2},n_{l2})$ couplings				$W_p^{(m_{l1},n_{l1})\times(m_{l2},n_{l2})}$			
0.065	(4,3) × (5,3)	(5,3) × (5,3)	(3,3) × (4,3)	(3,3) × (3,3)	-4.94E-04	2.33E-04	-1.54E-04	6.65E-05
	(2,1) × (4,3)	(2,1) × (5,3)	(1,1) × (4,3)	(1,1) × (5,3)	-6.31E-10	-4.10E-12	-1.54E-08	9.10E-11
	(2,1) × (6,5)	(2,1) × (7,5)	(1,1) × (6,5)	(1,1) × (7,5)	1.54E-13	1.35E-12	5.35E-12	7.68E-14
	(2,1) × (11,9)	(2,1) × (12,9)	(1,1) × (11,9)	(1,1) × (12,9)	-8.93E-16	2.24E-16	1.40E-17	2.38E-17
	(6,5) × (7,5)	(7,5) × (7,5)	(6,5) × (6,5)	(5,5) × (6,5)	-4.23E-04	2.37E-04	1.57E-04	-1.48E-04
	(2,1) × (4,3)	(2,1) × (5,3)	(1,1) × (4,3)	(1,1) × (5,3)	-8.57E-16	1.65E-16	-6.73E-16	1.41E-15
	(2,1) × (6,5)	(2,1) × (7,5)	(1,1) × (6,5)	(1,1) × (7,5)	-2.68E-08	-6.37E-09	-1.18E-08	-3.06E-11
	(2,1) × (11,9)	(2,1) × (12,9)	(1,1) × (11,9)	(1,1) × (12,9)	-3.23E-13	-3.78E-13	4.45E-14	-1.82E-14
	(8,7) × (9,7)	(9,7) × (9,7)	(9,7) × (10,7)	(7,7) × (8,7)	-3.36E-04	2.06E-04	-1.35E-04	-9.18E-05
	(2,1) × (4,3)	(2,1) × (5,3)	(1,1) × (4,3)	(1,1) × (5,3)	-5.39E-14	-1.96E-16	-1.10E-12	3.41E-14
	(2,1) × (6,5)	(2,1) × (7,5)	(1,1) × (6,5)	(1,1) × (7,5)	-2.17E-15	-2.69E-15	-8.66E-15	6.34E-19
	(2,1) × (11,9)	(2,1) × (12,9)	(1,1) × (11,9)	(1,1) × (12,9)	-9.98E-17	3.32E-17	-4.69E-17	1.04E-18
	(11,9) × (12,9)	(10,9) × (11,9)	(11,9) × (11,9)	(12,9) × (12,9)	-2.63E-04	-2.14E-04	1.81E-04	1.32E-04
	(2,1) × (4,3)	(2,1) × (5,3)	(1,1) × (4,3)	(1,1) × (5,3)	3.73E-17	1.11E-18	2.55E-16	2.25E-18
	(2,1) × (6,5)	(2,1) × (7,5)	(1,1) × (6,5)	(1,1) × (7,5)	-4.44E-12	-4.66E-12	-4.52E-12	-3.62E-15
	(2,1) × (11,9)	(2,1) × (12,9)	(1,1) × (11,9)	(1,1) × (12,9)	-1.55E-12	7.92E-13	-4.52E-12	-3.62E-15
	(8,7) × (9,7)	(7,7) × (8,7)	(9,7) × (9,7)	(7,7) × (7,7)	-1.51E-05	-1.47E-05	7.81E-06	7.28E-06
	(2,1) × (4,3)	(2,1) × (5,3)	(1,1) × (4,3)	(1,1) × (5,3)	5.35E-17	-2.09E-17	6.36E-15	1.38E-15
	(2,1) × (6,5)	(2,1) × (7,5)	(1,1) × (6,5)	(1,1) × (7,5)	6.64E-20	1.72E-21	-3.25E-19	1.65E-21
	(2,1) × (11,9)	(2,1) × (12,9)	(1,1) × (11,9)	(1,1) × (12,9)	1.29E-23	-6.45E-24	-2.98E-24	-1.23E-23
0.070	(6,5) × (7,5)	(7,5) × (7,5)	(5,5) × (6,5)	(5,5) × (5,5)	-4.28E-04	2.16E-04	-1.55E-04	7.25E-05
	(2,1) × (4,3)	(2,1) × (5,3)	(1,1) × (4,3)	(1,1) × (5,3)	-5.65E-14	1.46E-13	3.52E-12	-1.44E-13
	(2,1) × (6,5)	(2,1) × (7,5)	(1,1) × (6,5)	(1,1) × (7,5)	-5.80E-08	-2.35E-09	-6.05E-09	1.66E-10
	(2,1) × (11,9)	(2,1) × (12,9)	(1,1) × (11,9)	(1,1) × (12,9)	-1.28E-12	-1.24E-13	-1.44E-13	3.77E-14
	(4,3) × (5,3)	(5,3) × (5,3)	(3,3) × (4,3)	(4,3) × (4,3)	-4.69E-04	2.29E-04	-1.85E-04	1.77E-04
	(2,1) × (4,3)	(2,1) × (5,3)	(1,1) × (4,3)	(1,1) × (5,3)	-3.63E-10	5.91E-12	-5.63E-09	-1.20E-10
	(2,1) × (6,5)	(2,1) × (7,5)	(1,1) × (6,5)	(1,1) × (7,5)	1.37E-15	-2.57E-14	-4.22E-14	-1.32E-15
	(2,1) × (11,9)	(2,1) × (12,9)	(1,1) × (11,9)	(1,1) × (12,9)	1.17E-14	1.27E-15	-7.82E-14	1.96E-15
	(10,9) × (11,9)	(11,9) × (11,9)	(11,9) × (12,9)	(9,9) × (10,9)	-3.03E-04	1.74E-04	-9.75E-05	-9.47E-05
	(2,1) × (4,3)	(2,1) × (5,3)	(1,1) × (4,3)	(1,1) × (5,3)	3.67E-15	-5.68E-16	-2.34E-14	7.50E-17
	(2,1) × (6,5)	(2,1) × (7,5)	(1,1) × (6,5)	(1,1) × (7,5)	-2.59E-12	6.51E-14	-1.08E-12	1.65E-14
	(2,1) × (11,9)	(2,1) × (12,9)	(1,1) × (11,9)	(1,1) × (12,9)	-1.36E-12	1.94E-14	8.99E-13	-9.61E-15
	(8,7) × (9,7)	(9,7) × (9,7)	(7,7) × (8,7)	(8,7) × (8,7)	-3.38E-04	1.89E-04	-1.07E-04	7.33E-05
	(2,1) × (4,3)	(2,1) × (5,3)	(1,1) × (4,3)	(1,1) × (5,3)	-8.47E-13	1.83E-14	-1.59E-11	-2.31E-13
	(2,1) × (6,5)	(2,1) × (7,5)	(1,1) × (6,5)	(1,1) × (7,5)	-3.21E-16	3.42E-16	1.33E-15	-1.55E-17
	(2,1) × (11,9)	(2,1) × (12,9)	(1,1) × (11,9)	(1,1) × (12,9)	-4.37E-16	-4.91E-17	-6.37E-17	1.78E-18
	(9,9) × (10,9)	(10,9) × (11,9)	(9,9) × (9,9)	(11,9) × (11,9)	-4.63E-05	-4.63E-05	2.38E-05	2.36E-05
	(2,1) × (4,3)	(2,1) × (5,3)	(1,1) × (4,3)	(1,1) × (5,3)	-1.35E-19	-4.28E-20	-9.45E-19	9.17E-20
	(2,1) × (6,5)	(2,1) × (7,5)	(1,1) × (6,5)	(1,1) × (7,5)	-4.25E-13	3.82E-15	-1.54E-13	-4.88E-15
	(2,1) × (11,9)	(2,1) × (12,9)	(1,1) × (11,9)	(1,1) × (12,9)	-2.26E-14	1.05E-15	-5.44E-16	3.86E-17
0.080	(10,9) × (11,9)	(11,9) × (11,9)	(9,9) × (10,9)	(10,9) × (10,9)	-3.57E-04	1.87E-04	-1.76E-04	1.08E-04
	(2,1) × (4,3)	(2,1) × (5,3)	(1,1) × (4,3)	(1,1) × (5,3)	2.30E-16	2.67E-17	6.40E-16	9.24E-17
	(2,1) × (6,5)	(2,1) × (7,5)	(1,1) × (6,5)	(1,1) × (7,5)	-9.95E-12	1.08E-12	-1.81E-13	-5.27E-14
	(2,1) × (11,9)	(2,1) × (12,9)	(1,1) × (11,9)	(1,1) × (12,9)	-1.32E-12	-1.03E-13	-6.17E-14	8.76E-14
	(8,7) × (9,7)	(8,7) × (8,7)	(9,7) × (9,7)	(7,7) × (8,7)	-3.35E-04	2.41E-04	1.81E-04	-1.74E-04
	(2,1) × (4,3)	(2,1) × (5,3)	(1,1) × (4,3)	(1,1) × (5,3)	9.58E-15	1.31E-15	-5.37E-13	-4.79E-14
	(2,1) × (6,5)	(2,1) × (7,5)	(1,1) × (6,5)	(1,1) × (7,5)	1.42E-15	-1.03E-15	-5.15E-15	-5.91E-16
	(2,1) × (11,9)	(2,1) × (12,9)	(1,1) × (11,9)	(1,1) × (12,9)	6.86E-17	5.58E-18	2.39E-17	-6.27E-18

Table D.2: *For each unstable eigenvalue from Tab.(5.2) a set of four block rows with detailed information is associated. The first row of each block shows the four most important coupling contributions (components and amplitudes) to the potential energy. The following three rows in each block give the contribution to the potential energy of the* $(m,1)\times(m_l,n_l)$ *with* $m=2,1$ *couplings;* (m_l,n_l) *is either the dominant unstable component or is coupled to* $(2,1)$ *via one of the three strongest equilibrium components marked with "*" in Tab.(B.2)*

$I_h \cdot 10^5[A]$	$(m_{l1}, n_{l1}) \times (m_{l2}, n_{l2})$ couplings				$W_p^{(m_{l1}, n_{l1}) \times (m_{l2}, n_{l2})}$			
1.050	(4,3) × (4,3)	(4,3) × (5,3)	(2,−5) × (4,3)	(2,−5) × (2,−5)	-7.05E-04	-1.99E-04	-1.97E-04	9.52E-05
	(2,1) × (4,3)	(2,1) × (5,3)	(1,1) × (4,3)	(1,1) × (5,3)	-4.81E-08	4.41E-10	-3.18E-08	3.54E-09
	(2,1) × (6,5)	(2,1) × (7,5)	(1,1) × (6,5)	(1,1) × (7,5)	-8.16E-12	-9.84E-14	-4.56E-12	-1.35E-11
	(2,1) × (10,9)	(2,1) × (11,9)	(1,1) × (10,9)	(1,1) × (11,9)	2.32E-12	4.90E-13	-9.07E-10	2.19E-10
	(9,7) × (9,7)	(8,7) × (9,7)	(8,7) × (8,7)	(5,−1) × (9,7)	-6.80E-04	-8.96E-05	4.33E-05	-7.72E-06
	(2,1) × (4,3)	(2,1) × (5,3)	(1,1) × (4,3)	(1,1) × (5,3)	2.37E-11	-3.03E-12	3.78E-12	2.01E-11
	(2,1) × (6,5)	(2,1) × (7,5)	(1,1) × (6,5)	(1,1) × (7,5)	1.93E-12	-1.12E-12	9.53E-13	2.88E-12
	(2,1) × (10,9)	(2,1) × (11,9)	(1,1) × (10,9)	(1,1) × (11,9)	4.84E-15	9.55E-16	6.67E-16	7.82E-16
	(7,5) × (8,5)	(7,5) × (7,5)	(6,5) × (7,5)	(8,5) × (8,5)	-7.61E-04	4.93E-04	-4.89E-04	4.46E-04
	(2,1) × (4,3)	(2,1) × (5,3)	(1,1) × (4,3)	(1,1) × (5,3)	2.96E-11	5.58E-12	4.71E-11	-2.59E-11
	(2,1) × (6,5)	(2,1) × (7,5)	(1,1) × (6,5)	(1,1) × (7,5)	-1.57E-09	-4.22E-09	-2.76E-10	-1.88E-08
	(2,1) × (10,9)	(2,1) × (11,9)	(1,1) × (10,9)	(1,1) × (11,9)	-4.78E-11	-2.14E-11	-9.76E-10	-1.88E-08
	(4,3) × (5,3)	(3,3) × (4,3)	(4,3) × (4,3)	(3,3) × (3,3)	-3.45E-04	-3.33E-04	2.49E-04	1.86E-04
	(2,1) × (4,3)	(2,1) × (5,3)	(1,1) × (4,3)	(1,1) × (5,3)	-1.37E-08	-1.04E-09	-3.09E-08	8.92E-09
	(2,1) × (6,5)	(2,1) × (7,5)	(1,1) × (6,5)	(1,1) × (7,5)	-7.38E-12	-3.05E-11	-4.62E-12	-2.22E-11
	(2,1) × (10,9)	(2,1) × (11,9)	(1,1) × (10,9)	(1,1) × (11,9)	1.26E-12	5.16E-13	-6.73E-13	1.69E-13
	(6,5) × (7,5)	(7,5) × (8,5)	(7,5) × (7,5)	(6,5) × (6,5)	-8.43E-04	-7.92E-04	7.40E-04	4.54E-04
	(2,1) × (4,3)	(2,1) × (5,3)	(1,1) × (4,3)	(1,1) × (5,3)	-2.44E-13	-8.81E-15	-3.07E-12	7.61E-14
	(2,1) × (6,5)	(2,1) × (7,5)	(1,1) × (6,5)	(1,1) × (7,5)	-1.95E-09	-6.85E-09	-4.44E-09	-4.55E-09
	(2,1) × (10,9)	(2,1) × (11,9)	(1,1) × (10,9)	(1,1) × (11,9)	-3.52E-12	2.00E-12	-4.90E-12	6.98E-12
1.100	(11,9) × (11,9)	(9,1) × (11,9)	(9,1) × (9,1)	(11,9) × (12,9)	-3.58E-04	-2.43E-04	1.22E-04	-1.20E-04
	(2,1) × (4,3)	(2,1) × (5,3)	(1,1) × (4,3)	(1,1) × (5,3)	-1.52E-10	1.76E-11	-3.16E-08	3.43E-11
	(2,1) × (6,5)	(2,1) × (7,5)	(1,1) × (6,5)	(1,1) × (7,5)	5.17E-11	-2.80E-10	-8.59E-09	-1.73E-10
	(2,1) × (10,9)	(2,1) × (11,9)	(1,1) × (10,9)	(1,1) × (11,9)	2.11E-09	-1.28E-08	-2.90E-08	-4.88E-09
	(4,3) × (5,3)	(5,3) × (5,3)	(3,3) × (4,3)	(2,−5) × (4,3)	-5.15E-04	2.55E-04	-2.21E-04	-1.35E-04
	(2,1) × (4,3)	(2,1) × (5,3)	(1,1) × (4,3)	(1,1) × (5,3)	-1.93E-08	4.78E-09	-2.20E-05	-4.06E-09
	(2,1) × (6,5)	(2,1) × (7,5)	(1,1) × (6,5)	(1,1) × (7,5)	-2.06E-09	1.69E-08	-6.04E-07	1.01E-09
	(2,1) × (10,9)	(2,1) × (11,9)	(1,1) × (10,9)	(1,1) × (11,9)	-1.56E-10	5.51E-10	-5.87E-08	2.70E-09
	(3,3) × (4,3)	(4,3) × (5,3)	(4,3) × (4,3)	(3,3) × (3,3)	-6.89E-04	-5.88E-04	5.24E-04	3.66E-04
	(2,1) × (4,3)	(2,1) × (5,3)	(1,1) × (4,3)	(1,1) × (5,3)	-1.37E-09	-1.94E-10	-6.93E-07	1.35E-10
	(2,1) × (6,5)	(2,1) × (7,5)	(1,1) × (6,5)	(1,1) × (7,5)	-7.09E-11	8.32E-10	-2.84E-08	2.66E-12
	(2,1) × (10,9)	(2,1) × (11,9)	(1,1) × (10,9)	(1,1) × (11,9)	-7.11E-12	1.72E-11	-6.46E-08	-2.36E-10
	(3,3) × (4,3)	(4,3) × (5,3)	(4,3) × (4,3)	(3,3) × (3,3)	-6.32E-04	-5.78E-04	5.16E-04	3.31E-04
	(2,1) × (4,3)	(2,1) × (5,3)	(1,1) × (4,3)	(1,1) × (5,3)	-5.55E-10	2.27E-10	-4.09E-07	9.94E-10
	(2,1) × (6,5)	(2,1) × (7,5)	(1,1) × (6,5)	(1,1) × (7,5)	-4.57E-11	5.55E-10	-1.80E-08	-5.93E-12
	(2,1) × (10,9)	(2,1) × (11,9)	(1,1) × (10,9)	(1,1) × (11,9)	-4.45E-12	1.03E-11	3.55E-09	-2.87E-11
	(3,3) × (4,3)	(4,3) × (4,3)	(4,3) × (5,3)	(3,3) × (3,3)	-4.17E-04	3.75E-04	-3.54E-04	2.23E-04
	(2,1) × (4,3)	(2,1) × (5,3)	(1,1) × (4,3)	(1,1) × (5,3)	-1.17E-09	-1.77E-10	-4.63E-07	-3.93E-10
	(2,1) × (6,5)	(2,1) × (7,5)	(1,1) × (6,5)	(1,1) × (7,5)	-5.00E-11	6.77E-10	-1.97E-08	-7.75E-12
	(2,1) × (10,9)	(2,1) × (11,9)	(1,1) × (10,9)	(1,1) × (11,9)	-5.09E-12	9.43E-12	-2.18E-10	6.80E-11
1.200	(6,5) × (7,5)	(5,5) × (6,5)	(7,5) × (7,5)	(5,5) × (5,5)	-5.27E-04	-4.64E-04	2.92E-04	2.55E-04
	(2,1) × (4,3)	(2,1) × (5,3)	(1,1) × (4,3)	(1,1) × (5,3)	4.32E-13	1.56E-13	-2.05E-11	-4.07E-12
	(2,1) × (6,5)	(2,1) × (7,5)	(1,1) × (6,5)	(1,1) × (7,5)	-5.44E-09	1.55E-09	-3.20E-08	-4.20E-09
	(2,1) × (10,9)	(2,1) × (11,9)	(1,1) × (10,9)	(1,1) × (11,9)	5.44E-12	-5.25E-11	7.01E-10	3.59E-11
	(8,7) × (9,7)	(7,7) × (8,7)	(9,7) × (9,7)	(7,7) × (7,7)	-2.20E-04	-1.82E-04	1.08E-04	1.08E-04
	(2,1) × (4,3)	(2,1) × (5,3)	(1,1) × (4,3)	(1,1) × (5,3)	2.87E-11	5.50E-12	5.64E-11	1.36E-11
	(2,1) × (6,5)	(2,1) × (7,5)	(1,1) × (6,5)	(1,1) × (7,5)	-2.23E-12	2.44E-13	-1.10E-11	-2.94E-12
	(2,1) × (10,9)	(2,1) × (11,9)	(1,1) × (10,9)	(1,1) × (11,9)	1.96E-10	1.26E-09	8.81E-10	-9.97E-11
	(10,9) × (11,9)	(11,9) × (12,9)	(11,9) × (11,9)	(10,9) × (10,9)	-6.48E-04	-5.44E-04	4.30E-04	3.69E-04
	(2,1) × (4,3)	(2,1) × (5,3)	(1,1) × (4,3)	(1,1) × (5,3)	-7.00E-14	-4.51E-15	-7.02E-14	-1.33E-14
	(2,1) × (6,5)	(2,1) × (7,5)	(1,1) × (6,5)	(1,1) × (7,5)	5.10E-12	-2.41E-12	-9.32E-11	-8.98E-12
	(2,1) × (10,9)	(2,1) × (11,9)	(1,1) × (10,9)	(1,1) × (11,9)	-5.41E-10	-5.14E-10	-2.11E-10	6.91E-10
	(5,5) × (6,5)	(6,5) × (7,5)	(6,5) × (6,5)	(5,5) × (5,5)	-5.03E-04	-4.78E-04	3.29E-04	2.68E-04
	(2,1) × (4,3)	(2,1) × (5,3)	(1,1) × (4,3)	(1,1) × (5,3)	3.38E-12	5.27E-13	-3.37E-11	-2.13E-12
	(2,1) × (6,5)	(2,1) × (7,5)	(1,1) × (6,5)	(1,1) × (7,5)	-2.97E-09	2.00E-09	-3.94E-08	-3.82E-09
	(2,1) × (10,9)	(2,1) × (11,9)	(1,1) × (10,9)	(1,1) × (11,9)	-2.49E-11	2.22E-11	-4.90E-11	8.40E-12
	(10,9) × (11,9)	(11,9) × (12,9)	(11,9) × (11,9)	(10,9) × (10,9)	-6.47E-04	-5.68E-04	5.06E-04	3.56E-04
	(2,1) × (4,3)	(2,1) × (5,3)	(1,1) × (4,3)	(1,1) × (5,3)	1.47E-13	3.19E-15	-5.88E-14	-2.87E-15
	(2,1) × (6,5)	(2,1) × (7,5)	(1,1) × (6,5)	(1,1) × (7,5)	-1.82E-11	7.79E-12	1.97E-11	1.16E-12
	(2,1) × (10,9)	(2,1) × (11,9)	(1,1) × (10,9)	(1,1) × (11,9)	-8.30E-10	-1.99E-09	-4.41E-10	-2.17E-10

Table D.3

Table D.3 (on previous page): *For each unstable eigenvalue from Tab.(6.2) a set of four block rows with detailed information is associated. The first row of each block shows the four most important coupling contributions (components and amplitudes) to the potential energy. The following three rows in each block give the contribution to the potential energy of the* $(m,1) \times (m_l, n_l)$ *with* $m = 2, 1$ *couplings;* (m_l, n_l) *is either the dominant component or is coupled to* $(2,1)$ *via one of the three strongest equilibrium components marked with "*" in Tab.(B.4)*

Appendix E

NEMEC and free boundary equilibria

The NEMEC code is a combination between the fixed boundary spectral code VMEC and the vacuum Green's function code NESTOR (NEuman Solver for TOroidal Regions) [43], [44].
The vacuum magnetic field that confines the plasma $\vec{B_V}$ is written in the form $\vec{B_V} = \vec{B_0} + \vec{\nabla}\Phi$ where $\vec{B_0}$ is the field arising from the net toroidal plasma current and the external coil currents, and Φ is a single-valued potential. A free boundary equilibrium is reached when at the plasma boundary Σ_p, the total pressure $B^2/2 + p$ is continous and $\vec{B_V}$ satisfies the Neuman condition

$$(\vec{B_0} + \vec{\nabla}\Phi) \cdot \vec{n_p} = 0 \tag{E.1}$$

For a given $\vec{B_0}$ the vacuum field solution is obtained by solving the exterior Neuman problem for the potential Φ. In the exterior of the plasma domain, Φ obeys to the Laplace equation $\Delta\Phi = 0$ and on the plasma boundary, its normal derivative assumes the prescribed value $\partial\Phi/\partial n = -\vec{B_0} \cdot \vec{n}$.
Using Green's theorem, the Laplace equation for Φ is converted into a surface integral equation

$$\Phi(\vec{x}) + \frac{1}{2\pi} \int d\,\Sigma'_p \, \frac{\partial G(\vec{x}, \vec{x'})}{\partial n'} \Phi(\vec{x'}) = \frac{1}{2\pi} \int d\,\Sigma'_p \, G(\vec{x}, \vec{x'}) \, \frac{\partial \Phi(\vec{x'})}{\partial n'} \tag{E.2}$$

where the points $\vec{x}$ and $\vec{x'}$ belong to the boundary Σ_p and $G(\vec{x}, \vec{x'}) = 1/|\vec{x} - \vec{x'}|$ is the Green's function. If the condition Eq.(E.1) is imposed, the right hand side of this eqaution can be explicitely evaluated and acts as a source term. The potential Φ in the interior of the toroidal region is obtained in a similar way from the potential and its normal derivative on the boundary.

The surface Σ_p and the potential Φ are represented by Fourier series in the angular variables u and v (c.f. Section 2.1). From the Fourier transform of the integral equation, a set of linear equations for the Fourier coefficients of Φ are obtained. The principal technical difficulty inherent to this method is the calculation of the Fourier transform of the singular Green's function and its normal derivative. A regularization procedure was introduced to solve this problem: appropiate functions with the same singularity and periodicity are substracted from the integral kernels and their analytical calculated Fourier transforms are added to the Fourier transformed integral equations. Detailed explanations and other information can be found in [43].

Appendix F

Coil configurations

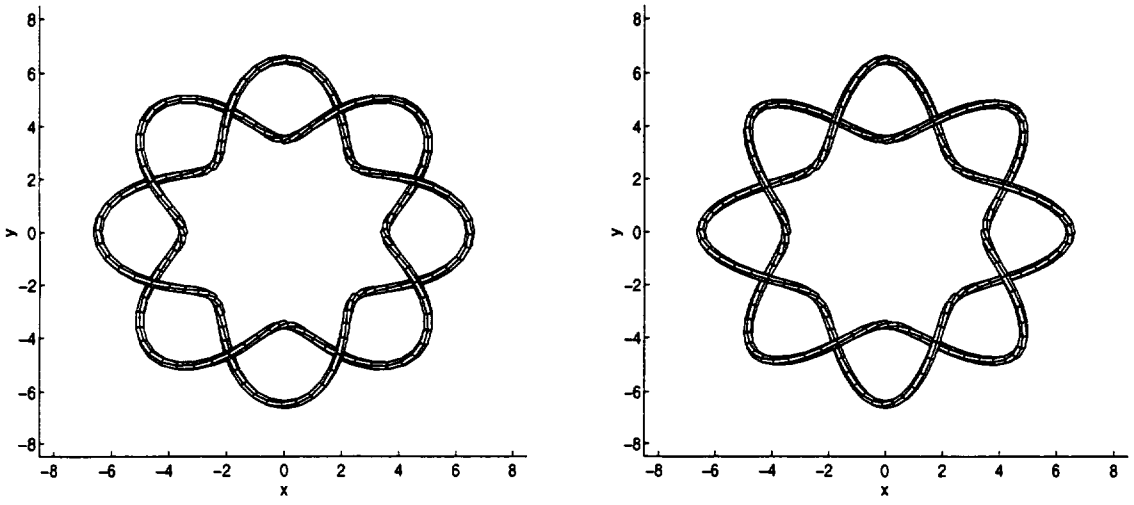

Figure F.1: Topview of one pair of HF coils with $\alpha = 0$ (**left**) and $\alpha = -0.3$ (**right**)

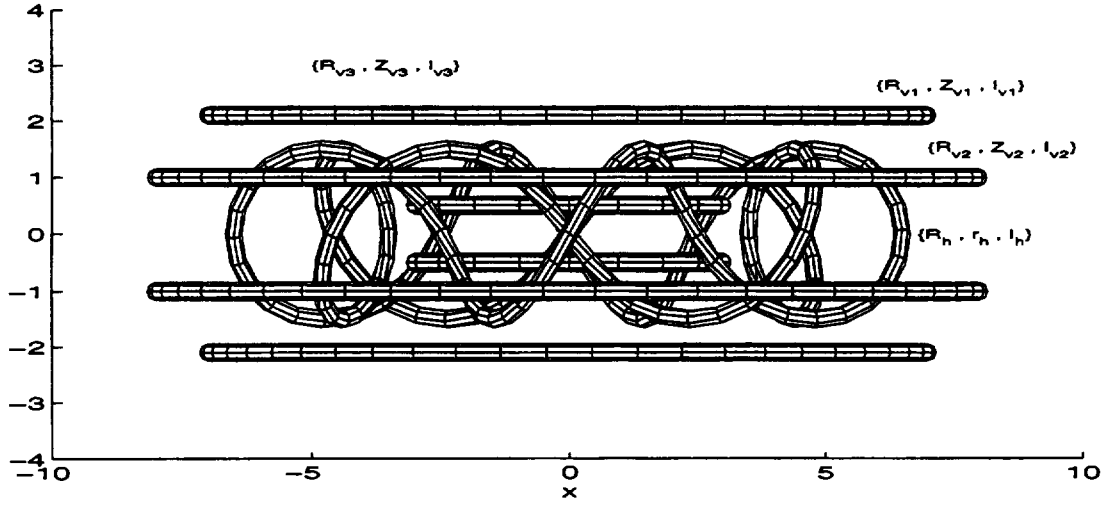

Figure F.2: Sidewiew of three pairs of VF coils characterized by $\{R_{vi}, Z_{vi}, I_{vi}\}$, $i = 1, 2, 3$ and one pair of HF coils characterized by $\{R_h, Z_h, I_h\}$.

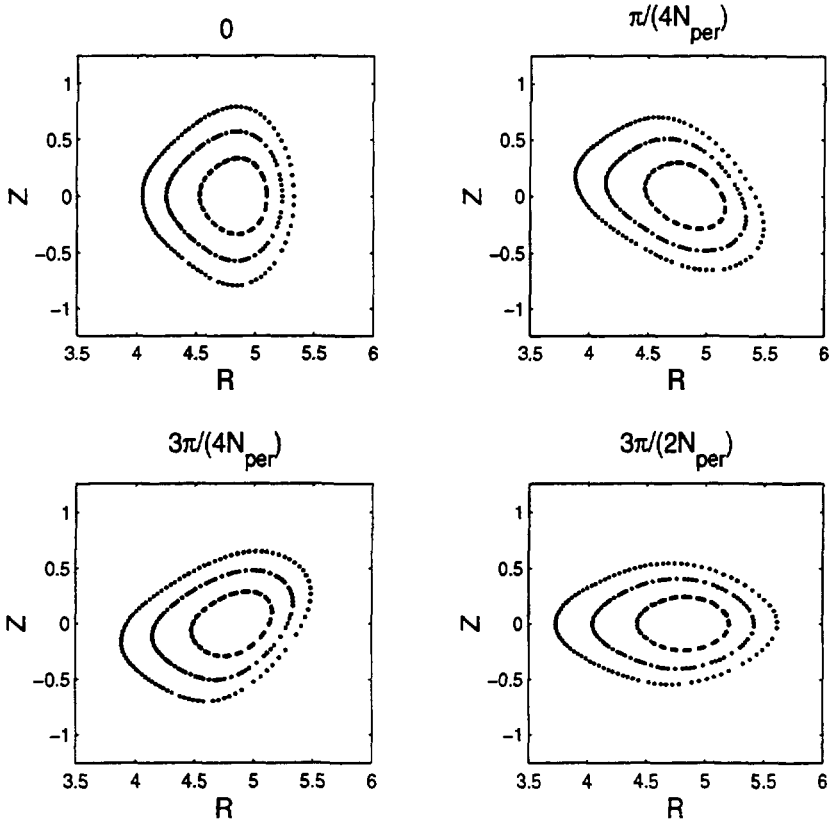

Figure F.3: Flux surfaces in vacuum produced with a $L = 2$ torsatron configuration consisting in one pair of HF coils and three pairs of VF coils. The geometry is described by $R_h = 5.0\,[\mathrm{m}]$, $r_h = 1.7\,[\mathrm{m}]$, $\alpha = 0.$, $R_{v1} = 7.0\,[\mathrm{m}]$, $Z_{v1} = 2.1\,[\mathrm{m}]$, $R_{v2} = 8.0\,[\mathrm{m}]$, $Z_{v2} = 1.2\,[\mathrm{m}]$, $R_{v3} = 3.0\,[\mathrm{m}]$, $Z_{v3} = 0.5\,[\mathrm{m}]$. The currents in the coils are $I_h = 1.0 \cdot 10^5[A]$, $I_{v1} = -3.9 \cdot 10^4[A]$, $I_{v2} = -1.0 \cdot 10^4[A]$, $I_{v3} = 2.3 \cdot 10^4[A]$.

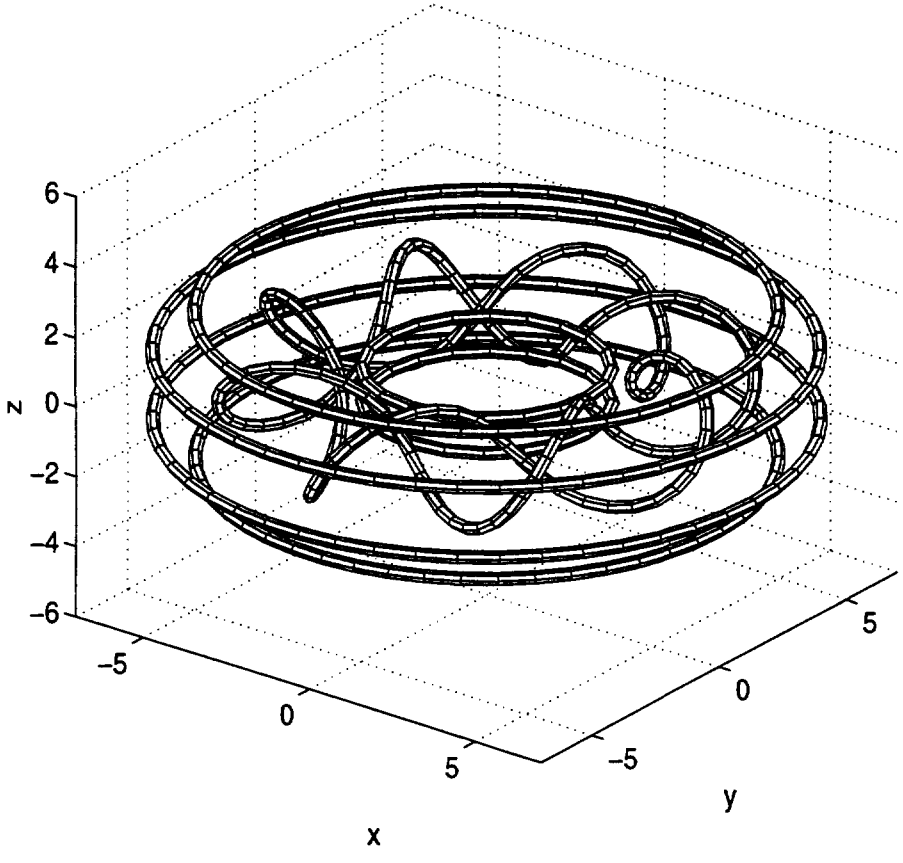

Figure F.4: Torsatron configuration consisting of one pair of HF coils and 3 pairs of VF coils. Fig.6.3, Fig.6.4 and Fig.F.3 show the flux surfaces in vacuum obtained with this configuration (c.f. Section 6.2).